UCLA
UCLA Electronic Theses and Dissertations

Title

Thermodynamic Controls on Deep Convection in the Tropics: Observations and Applications to Modeling

Permalink

https://escholarship.org/uc/item/9cv400pc

Author

Schiro, Kathleen Anne

Publication Date

2017

Peer reviewed|Thesis/dissertation

UNIVERSITY OF CALIFORNIA

Los Angeles

Thermodynamic Controls on Deep Convection in the Tropics:

Observations and Applications to Modeling

A dissertation submitted in partial satisfaction

of the requirements for the degree of Doctor of Philosophy

in Atmospheric and Oceanic Sciences

by

Kathleen Anne Schiro

2017

ABSTRACT OF THE DISSERTATION

Thermodynamic Controls on Deep Convection in the Tropics:

Observations and Applications to Modeling

by

Kathleen Anne Schiro

Doctor of Philosophy in Atmospheric and Oceanic Sciences

University of California, Los Angeles, 2017

Professor J. David Neelin, Chair

Constraining precipitation processes in climate models with observations is crucial to accurately simulating current climate and reducing uncertainties in future projections. This work presents robust relationships between tropical deep convection, column-integrated water vapor (CWV), and other thermodynamic quantities analyzed with data from the DOE Atmospheric Radiation Measurement (ARM) Mobile Facility in Manacapuru, Brazil as part of the GOAmazon campaign and are directly compared to such relationships at DOE ARM sites in the tropical western Pacific. A robust relationship between CWV and precipitation, as explained by variability in lower tropospheric humidity, exists just as strongly in a tropical continental region as it does in a tropical oceanic region. Given sufficient mixing in the lower troposphere, higher CWV generally results in greater plume buoyancies through a deep convective layer. Although sensitivity of

convection to other controls is suggested, such as microphysical processes and dynamical lifting mechanisms, the increase in buoyancy with CWV is consistent with the sharp increase in precipitation observed.

Entraining plume buoyancy calculations confirm that CWV is a good proxy for the conditional instability of the environment, yet differences in convective onset as a function of CWV exist over land and ocean, as well as seasonally and diurnally over land. This is largely due to variability in the contribution of lower tropospheric humidity to the total column moisture. Over land, the relationship between deep convection and lower free tropospheric moisture is robust across all seasons and times of day, whereas the relation to boundary layer moisture is robust for the daytime only. Using S-Band radar, these transition statistics are examined separately for unorganized and mesoscale-organized convection, which exhibit sharp increases in probability of occurrence with increasing moisture throughout the column, particularly in the lower free troposphere. An observational basis for an integrated buoyancy measure from a single plume buoyancy formulation that provides a strong relation to precipitation can be useful for constraining convective parameterizations. A mixing scheme corresponding to deep inflow of environmental air into a plume that grows with height provides a weighting of boundary layer and free tropospheric air that yields buoyancies consistent with the observed onset of deep convection across seasons and times of day, across land and ocean sites, and for all convection types. This provides a substantial improvement relative to more traditional constant mixing assumptions, and a dramatic improvement relative to no mixing. Furthermore, it provides relationships that are as strong or stronger for mesoscale-organized convection as for unorganized convection.

Downdrafts and their associated parameters are poorly constrained in models, as physical and microphysical processes of leading order importance are difficult to observe with sufficient

frequency for development of robust statistics. Downdrafts and cold pool characteristics for mesoscale convective systems (MCSs) and isolated, unorganized deep precipitating convection in the Amazon are composited and both exhibit similar signatures in wind speed, surface fluxes, surface equivalent potential temperature (θ_e) and precipitation. For both MCSs and unorganized convection, downdrafts associated with the strongest modifications to surface thermodynamics have increasing probability of occurrence with decreasing height through the lowest 4 km and show similar mean downdraft magnitudes with height. If θ_e is approximately conserved following descent, a large fraction of the air reaching the surface likely originates at altitudes in the lowest 2 km. Mixing computations suggest that, on average, air originating at heights greater than 3 km would require substantial mixing, particularly in the case of isolated cells, to match the observed cold pool θ_e. Statistics from two years of surface meteorological data at the GOAmazon site and 15 years of data at the DOE ARM site on Manus Island in the tropical western Pacific show that $\Delta\theta_e$ conditioned on precipitation levels off with increasing precipitation rate, bounded by the maximum difference between surface θ_e and its minimum in the profile aloft. Robustness of these statistics observed across scales and regions suggests their potential use as model diagnostic tools for the improvement of downdraft parameterizations in climate models.

The dissertation of Kathleen Anne Schiro is approved.

Rong Fu

Leila M. V. Carvalho

Robert G. Fovell

Alexander D. Hall

J. David Neelin, Committee Chair

University of California, Los Angeles

2017

DEDICATION

to my parents, Anne and Don,

to my brother, Richard,

and to my fiancé Andrew

TABLE OF CONTENTS

List of Figures

List of Tables

ACKNOWLEDGEMENTS

Kathleen Anne Schiro

Los Angeles, California

June, 2017

KATHLEEN ANNE SCHIRO

EDUCATION

University of California, Los Angeles | Los Angeles, CA

      M. S., Atmospheric and Oceanic Sciences   June 2014

Johns Hopkins University | Baltimore, MD

      B. A., Earth and Planetary Sciences   May 2011

FELLOWSHIPS AND AWARDS

Dissertation Year Fellowship | UCLA Graduate Division   Fall 2016 –Spring 2017

Best Poster Presentation | WCRP Latin America and Caribbean Conference   2014

Second Place Poster | 28th Conference on Hydrology, American Meteorological Society   2014

Neiburger Memorial Award | UCLA AOS – for excellence in teaching   2013

Bosart Award | UCLA AOS – for service to students and the department   2013

Group Achievement Award | NASA Ames Research Center   2012

PUBLICATIONS

B.R. Lintner, D.K. Adams, K.A. Schiro, A. Stansfield, A. da Rocha, and J.D. Neelin, 2017: Relationships among climatological vertical moisture structure, column water vapor, and precipitation over the central Amazon in observations and CMIP5 models. *Geophysical Research Letters,* **44***,*1981-1989.

Schiro, K.A., J.D. Neelin, D.K. Adams, B.R. Lintner, 2016: Deep Convection and Column Water Vapor over Tropical Land vs. Tropical Ocean: A comparison between the Amazon and the Tropical Western Pacific. *Journal of the Atmospheric Sciences,* **73**, 4043–4063.

Xue, Y., F. De Sales, W.K.M Lau, A. Boone, K.M. Kim, G. Wang, F. Kucharski, K.A. Schiro, M. Hosaka, S. Li, C. R. Mechoso, L.M. Druyan, I.S. Sanda, W. Thiaw, N. Zeng, R.E.

Comer, Y-K Lim, S. Mahanama, G. Song, Y. Gu, M. Chin, P. Dirmeyer, S.M. Hagos, E. Kalnay, A. Kitoh, L.R. Leung, C-H. Lu, N.M. Mahowald, S. Schubert, Z. Zhang, 2016: West African monsoon decadal variability and drought and surface-related forcings: Second West African Monsoon Modeling and Evaluation Project Experiment (WAMME II). *Climate Dynamics,* **47**, 3517-3545.

Boone, A., Y. Xue, F. De Sales, R. Comer, S. Hagos, S. Mahanama, K.A. Schiro, G. Song, G. Wang and C. R. Mechoso, 2016: The regional impact of Land-Use Land-cover Change (LULCC) over West Africa from an ensemble of global climate models under the auspices of the WAMME2 project. *Climate Dynamics,* **47**, 3547-3573.

Sperber, K. R., E. Cuisinier, A. Kitoh, C. R. Mechoso, A. Moise, W. Moufouma-Okia, K.A. Schiro, and A. G. Turner, 2017: The Global Monsoon System: Research and Forecast (3rd Edition) - Chapter 7: Modelling Monsoons. World Scientific Series on Asia-Pacific Weather and Climate: Vol. 9.

Yates, E.L., A.M. Detweiler, L.T. Iraci, B.M. Bebout, C.P. McKay, K.A. Schiro, E.J. Sheffner, C.A. Kelley, J.M. Tadić, M. Loewenstein, 2013: Assessing the role of alkaline soils on the carbon cycle at a playa site. *Environmental Earth Science,* **70**, 1047-1056.

Yates, E.L., K.A. Schiro, M. Lowenstein, E.J. Sheffner, L.T. Iraci, J.M. Tadic, and A. Kuze, 2011: Carbon Dioxide and Methane at a Desert Site – A Case Study at Railroad Valley Playa, Nevada, USA. *Atmosphere*, **2**, 702-711.

CHAPTER 1

Introduction

Understanding how precipitation will change in the future is one of most important, scientifically challenging, and societally relevant climate problems. Climate model disagreement on both the sign and magnitude of future precipitation changes in the tropics (IPCC AR5 WG1 Ch. 12) is one of the largest uncertainties in understanding the response of climate to increasing greenhouse gas concentrations (Douville et al. 2006). Currently, the scientific community has a limited understanding of what controls the distribution and variability of rainfall, and a lack of robust observational constraints on precipitation processes in models continues to perpetuate this uncertainty. Thus, there is a dire need to reduce such uncertainties by systematically studying the processes governing deep precipitating convection and by finding simple, robust ways to observationally constrain such processes in climate models.

The uncertainty linked to deep convection lies primarily within a model's representation of complicated interactions across scales and the onset of deep convection. Since most of the present-day global climate models (GCMs) cannot explicitly resolve the small-scale physics of convection, the ensemble effect of convection is represented through parameterization. Observational constraints on these processes would provide much-needed insight into the physical basis of these parameterizations.

Several factors contribute to deep convective onset and associated uncertainty in GCMs, yet one of the most significant is thought to be the entrainment profile. Deep convective plumes interact with the surrounding environment as they ascend, mixing in air that dilutes plume buoyancy. Thus, plumes ascending through moister air are more likely to remain buoyant through

the depth of the troposphere. Several previous studies suggest that deep convection is sensitive to moisture in the free troposphere (e.g. Austin 1948; Malkus 1954; Brown and Zhang 1997; Derbyshire et al. 2004; Guichard et al. 2004; Sobel et al. 2004; Holloway and Neelin 2009), yet these processes are difficult to observe and are thus poorly constrained in GCMs.

GCMs are also sensitive to downdrafts parameters (Maloney and Hartmann 2001; Sahany and Nanjundiah 2008; Pritchard et al. 2011). Convective downdrafts are primarily a result of condensate loading and the evaporation of hydrometeors in unsaturated air below cloud base (e.g. Houze 1993), which form cold pools of air that spread horizontally and can initiate convection at their leading edge (e.g. Weisman and Klemp 1986). Observational limitations have hindered the development of robust statistics of such processes, and thus remain poorly constrained in GCMs. Most previous observational studies of downdrafts have examined case studies using data from field campaigns, which have been largely focused over tropical oceans and the continental US.

Overall, a key factor limiting our understanding of deep convection is that the complex interplay between precipitation, convection, and the large-scale dynamics in the tropics has been difficult to observe in both space and time, and taking a multi-scale approach to investigating these relationships is critical. The research conducted in this dissertation employs in-situ observations from a two-year intensive US Department of Energy (DOE) - Brazil collaborative field campaign in the Amazon ("GOAmazon") and multi-year records from DOE Atmospheric Radiation Measurement (ARM) sites in the tropical western Pacific.

My main research goals for this work are as follows: (1) to examine similarities and differences in thermodynamic controls on deep convection over land and ocean in the tropics; (2) to better understand how variability in moisture vertical structure controls deep convection in the tropics, and how this can be understood in terms of mixing schemes suitable for convective

parameterizations; (3) to probe the physics of downdrafts over the Amazon and bound their behavior using simple thermodynamic arguments; (4) to present robust, statistical relationships describing these processes, for potential use as observational constraints for convective parameterizations and model diagnostic tools; (5) to understand to what extent these observational relationships apply to spatially organized mesoscale systems, and to what extent these are similar or different from unorganized convection.

This dissertation is based on published and to-be-published work that draws conclusions from the exploration of the research goals outlined above. Chapter 2, published as Schiro et al. (2016), concludes that leading order behavior characterizing a strong relation between precipitation and column integrated humidity identified in previous studies over tropical oceans act similarly as thermodynamic controls on deep convection over the Amazon. Chapter 3 explores this behavior in detail, concluding that variability in lower tropospheric moisture is the main thermodynamic factor contributing to variability in the onset of organized and unorganized deep convection (e.g. regional, seasonal, diurnal), and that a measure of buoyancy based on a mixing scheme that includes nearly equal weighting of boundary layer and free tropospheric air can be a useful predictor of precipitation across regions, seasons, and times of day for both organized and unorganized convection. Chapter 4 closes the loop by examining downdraft characteristics for mesoscale convective systems and isolated cells. For both convective types, evidence from radar vertical velocity and thermodynamic arguments imply downdrafts originate in the lowest few kilometers. Relationships between precipitation and surface thermodynamics suggest downdrafts reach a typical limit in their cooling/drying potential at the surface for rain rates higher than 10 mm hr^{-1}. Simple, statistical relationships focused on providing observational constraints for convective parameterizations are presented in all three chapters.

CHAPTER 2

Deep Convection and Column Water Vapor over Tropical Land vs. Tropical

Ocean: A comparison between the Amazon and the Tropical Western Pacific

Abstract

The relationships between the onset of tropical deep convection, column water vapor (CWV), and other measures of conditional instability are analyzed with two years of data from the DOE Atmospheric Radiation Measurement (ARM) Mobile Facility in Manacapuru, Brazil as part of the GOAmazon campaign, and with 3.5 years of CWV derived from Global Positioning System meteorology at a nearby site in Manaus. Important features seen previously in observations over tropical oceans — precipitation conditionally averaged by CWV exhibiting a sharp pickup at high CWV, and the overall shape of the CWV distribution for both precipitating and non-precipitating points — are also found for this tropical continental region. The relationship between rainfall and CWV reflects the impact of lower free tropospheric moisture variability on convection. Specifically, CWV over land, as over ocean, is a proxy for the effect of free tropospheric moisture on conditional instability as indicated by entraining plume calculations from GOAmazon data. Given sufficient mixing in the lower troposphere, higher CWV generally results in greater plume buoyancies through a deep convective layer. Although sensitivity of buoyancy to other controls in the Amazon is suggested, such as boundary layer and microphysical processes, the CWV dependence is consistent with the observed precipitation onset. Overall, leading aspects of the relationship between CWV and the transition to deep convection in the Amazon have close parallels over tropical oceans. The relationship is robust to averaging on time and space scales appropriate for convective physics, but is strongly smoothed for averages greater than three hours or 2.5°.

2.1   Introduction

Despite the complex relationships, interactions, and feedbacks that exist among the atmosphere, land, and ocean, a robust relationship exists between precipitation and column water vapor (CWV). Bretherton et al. (2004) identified a smooth relationship of CWV and precipitation in daily mean satellite observations. On shorter timescales, conditionally averaged precipitation rate increases sharply with increasing CWV (Peters and Neelin 2006, Holloway and Neelin 2009, Neelin et al. 2009). This sharp pickup is associated with the onset of conditional instability leading to deep convection. Furthermore, statistics of the transition to deep convection are analogous to properties of a continuous phase transition at a critical value of CWV (Peters and Neelin 2006; Neelin et al. 2009) and can be understood in terms of stochastic variations across the deep convective onset threshold (Stechmann and Neelin 2011). Evaluating this deep convective transition using radiosondes from the DOE ARM site at Nauru in the tropical western Pacific, Holloway and Neelin (2009) demonstrated that CWV represents a proxy for the impact of free tropospheric humidity on the conditional instability of entraining plumes affecting the transition from shallow to deep convection, and thus that the statistics quantifying this transition provide a substantial constraint on subgrid scale processes that must be represented in climate models. It was previously unclear, however, the extent to which this simplifying CWV-precipitation relationship applies for convective transition statistics over tropical land, as fundamental differences exist in the convective environment over land compared to ocean - including a stronger diurnal cycle and greater variations in the boundary layer (Nesbitt and Zipser 2003).

There is substantial evidence suggesting the importance of free tropospheric humidity to the onset of deep convection (Austin 1948; Malkus 1954; Yoneyama and Fujitani 1995; Brown and Zhang 1997; Wei et al. 1998; Raymond and Torres 1998; Sherwood and Wahrlich 1999;

Parsons et al. 2000; Raymond 2000; Raymond and Zeng 2000; Tompkins 2001a; Redelsperger et al. 2002; Ridout 2002; Grabowski 2003; Bretherton et al. 2004; Chaboureau et al. 2004; Derbyshire et al. 2004; Guichard et al. 2004; Sobel et al. 2004; Sherwood et al. 2004; Kuang and Bretherton 2006; Tian et al. 2006; Wu et al. 2009; Waite and Khouider 2010; Zhang and Klein 2010; Kumar et al. 2013), yet many models are currently too insensitive to free tropospheric humidity (Biasutti et al. 2006; Dai 2006; Oueslati and Bellon 2013). This insensitivity contributes to systematic errors and biases in simulated precipitation on a number of space and time scales: the erroneous appearance of a double inter-tropical convergence zone (Hirota and Takayabu 2013; Hirota et al. 2014); deficiencies in the simulation of the Madden-Julian Oscillation (Grabowski and Moncrieff 2004; Hannah and Maloney 2011; Jiang et al. 2011; Del Genio et al. 2011; Kim et al. 2012; Holloway et al. 2013; Kim et al. 2014; Rowe and Houze 2015); failure to represent the shallow-to-deep convective transition and diurnal cycle of deep convection (Randall et al. 1991; Yang and Slingo 2001; Betts and Jakob 2002; Dai and Trenberth 2004; Bechtold et al. 2004; Chaboureau et al. 2004; Guichard et al. 2004; Dai 2006; Del Genio and Wu 2010; Waite and Khouider 2010). The effect of free tropospheric humidity on the onset of deep convection can be explained through mixing between a convective plume and its surrounding environment, which greatly affects the plume's buoyancy. Mixing assumptions must, therefore, be appropriately constrained in convective parameterizations. This has been a long-standing challenge, yet several studies have demonstrated significant model improvement with realistic representations of entrainment processes (Neale et al. 2008; Bechtold et al. 2008; Zhao et al. 2009; Neelin et al. 2010; Sahany et al. 2012). In this regard, the convective transition statistics developed over tropical oceans have proven useful as model diagnostics (Sahany et al. 2012, 2014) that help to constrain entrainment representations, along with other observational and modeling studies (Raymond and

6

Blyth 1986; Brown and Zhang 1997; Jensen and Del Genio 2006; Kuang and Bretherton 2006; Li et al. 2008; Bacmeister and Stephens 2011; Luo et al. 2010; Romps and Kuang 2010). The transition to deep convection can also be examined in the temporal domain (Holloway and Neelin 2010; Adams et al. 2013) in which timescales, lead-lag relations and the distinction between temporal onset and termination (Stechmann and Neelin 2014) can be important.

There are several additional variables and processes controlling the transition to deep convection that must also be understood and accurately represented in models: free tropospheric moistening processes (Johnson et al., 1999; Benedict and Randall, 2007; Kemball-Cook and Weare, 2001; Mapes et al., 2006; Hohenegger and Stevens 2013; Kumar et al. 2013; Masunaga 2013; Hagos et al. 2014); the influence of the diurnal cycle (Betts and Jakob 2002; Bechtold et al. 2004; Chaboureau et al. 2004; Del Genio and Wu 2010; Zhang and Klein 2010; Bechtold et al. 2014); the larger-scale dynamics forcing vertical ascent (Kumar et al. 2013; Hohenegger and Stevens 2013); convective downdrafts and cold pool formation (Tompkins 2001b; Khairoutdinov and Randall 2006; Schlemmer and Hohenegger 2014); cloud size (Boing et al. 2012); moist static energy gradients (Neelin and Held 1987; Lintner and Neelin, 2007, 2008; Raymond et al. 2009; Lintner and Neelin 2010; Ma et al. 2011); vertical wind shear (Rotunno et al. 1988; LeMone et al. 1998); and microphysical processes, including cloud-aerosol interactions (Andreae et al. 2004; Khain et al. 2005). Important differences likely exist in the way these processes and variables contribute to the conditional instability of the environment over tropical land vs. tropical oceans.

Thus far, an insufficient observational record in the continental tropics has limited development of convective transition statistics, yet the Green Ocean Amazon campaign in Manacapuru, Brazil (2014-2015, Martin et al. 2016) has provided a unique opportunity to evaluate the transition to deep convection over tropical land, to elucidate potential complexities compared

to the ocean, and to develop simple, useful statistics as model diagnostics. Here, we derive the CWV-precipitation relationship and associated statistics with these data and with a complementary 3.5 year data set from the central Amazon using Global Positioning System (GPS) meteorology that provides continuous, all-weather observations of CWV at high temporal resolution over tropical land (Adams et al. 2013, 2015). Parallels are drawn between the land and the ocean to assess whether free tropospheric humidity is also of leading order importance to the conditional instability of an entraining plume over land as it is over ocean. The robustness of the convective transition statistics is tested as a function of spatial and temporal scales to establish a benchmark for comparison between models and observations at various scales. Lastly, the CWV-precipitation relationship is examined physically by linking vertical profiles of key thermodynamic quantities and plume buoyancies computed using turbulent mixing to the observed onset of deep convection.

2.2   Data

A suite of observations is used to establish relationships between CWV and deep convection across various instruments, time periods, and tropical locations. The principal location examined is the DOE ARM Mobile Facility at Manacapuru, BR (3° 12' S, 60° 35' W, 50 meters altitude), established as part of the GOAmazon field campaign (January 2014 - December 2015). The GOAmazon data used in this study cover the period 10 Jan 2014 to 20 Oct 2015. The results for the GOAmazon site are compared to those derived from two retired DOE ARM sites in the Tropical Western Pacific: Nauru Island (0° 31' S, 166° 54' E, 7 meters altitude) and Manus Island (2° 3' S, 147° 25' E, 4 meters altitude). The analysis period used in this study and in Holloway and Neelin (2009) for Nauru spans Apr. 2001 – Aug. 2006, and the analysis period from Manus Island spans Jan. 2008 – Dec. 2010. In terms of radiosonde launches, these periods yield roughly

8

comparable numbers to the western Pacific sites (3320 for Nauru and 3309 for Manus), each somewhat larger than the 2379 for GOAmazon.

Additional observations from a GPS meteorological station in Manaus, Brazil are included in this study; this station functioned from July 2008 to December 2011 as part of the National Oceanic and Atmospheric Administration/Earth System Research Laboratory (NOAA/ESRL) Real-Time Ground-Based GPS Meteorological Network and was located at the National Institute for Amazon Research/Large Scale Biosphere-Atmosphere Experiment (INPA/LBA) in Manaus (2.61°S, 60.21°W) (Adams et al. 2013, 2015).

2.2.1 *Column Water Vapor*

Radiosonde measurements at all ARM sites were obtained from Vaisala Digi-Cora III sounding systems at 2-second resolution; the raw sounding data were interpolated to 5-hPa intervals. Reported instrumental uncertainties are approximately 0.5°C for temperature and 5% for relative humidity below 500 hPa. At the GOAmazon site, radiosonde launches occurred four times daily (6 hourly), at 05:30, 11:30, 17:30, and 23:30 UTC (01:30, 07:30, 13:30, and 19:30 LT), with occasional launches at 14:30 UTC (10:30 LT) during the wet season. At Nauru, launches took place at 00:00 and 12:00 UTC (12:00 and 0:00 LT), with occasional launches at 02:30 and 14:30 UTC (14:30 and 02:30 LT), while at Manus Island, most launches took place at either 11:30 or 23:30 UTC, with occasional launches at 03:30 or 15:30 UTC (13:30 or 01:30 LT).

Water vapor and liquid water data sampled by microwave radiometer (MWR) at the GOAmazon site are derived from measurements of absolute microwave radiances (expressed as brightness temperatures) obtained at 23.8 GHz and 31.4 GHz. The retrieval uncertainty for brightness temperatures is 0.3 K and for CWV is typically ~ 0.5 mm. The data used here are derived from radiance measurements with a statistical retrieval algorithm that uses monthly derived and

location-dependent linear regression coefficients (Liljegren 1999). Data from another CWV product derived from a more physically-based retrieval (Turner et al. 2007) are compared to these data in the Appendix. All data for which the brightness temperature exceeds 100 K are removed from this dataset (Morris 2006), as are data that are affected by direct sunlight near local noon (15Z – 17Z) for roughly a 3-week period surrounding the equinoxes. To address the so-called wet-window problem, in which water collecting on the surface of the lens introduces measurement inaccuracy during rainy periods, we linearly interpolate CWV values across time-periods of 6 hours or less. While the existence of the wet-window problem introduces uncertainty, particularly within the highest CWV bins, we argue that the linear interpolation procedure likely underestimates peak CWV and is justified given that the data gaps are typically short and the temporal persistence of water vapor values for strong convective events is on the order of hours (Holloway and Neelin 2010). Additionally, Figure A1 in the Appendix illustrates that there is no obvious systematic bias at high CWV for the times sampled (15-minute average radiometer CWV surrounding radiosonde launch between 10 Jan 2014 and 31 July 2014), which suggests that this interpolation does not greatly affect the results presented in this study.

One way to overcome measurement inaccuracy during rainy times is through use of GPS technology, as its all-weather capability allows for CWV measurements during rainy times (Adams et al. 2011; Adams et al. 2015). The CWV from GPS is derived from water-vapor-induced delays in the radio signals from the satellite to the ground-based receiver (Bevis et al., 1992), and its accuracy in the Amazon is on the order of 1-2 mm (Adams et al. 2011). The INPA site consisted of a dual frequency, geodetic-grade GNSS receiver/antenna and meteorological station concurrently measuring pressure, temperature, relative humidity, winds, and precipitation at 1 min

sampling frequency. NOAA/ESRL processed the GNSS data in near real time (2 h latency), with 30-minute average CWV values used in this study.

2.2.2 *Precipitation*

The GOAmazon precipitation measurements analyzed in Sections 2.3, 2.4 and 2.6.3 are from the Aerosol Observing System (AOS) meteorological station, measured by the acoustic gauge of a Vaisala WXT520. When related to radiosonde CWV, AOSMET precipitation is averaged at 1-hour intervals surrounding the launch; for analyses with radiometer CWV, AOSMET precipitation is averaged at 15-minute intervals. In Section 2.4, the averaging intervals are varied to evaluate the robustness of the statistics. These data were chosen among many other datasets available because we deemed them the most reliable over the full 2014-2015 period (a detailed comparison of the different precipitation observing systems available at the GOAmazon site is included in Figs. 2.A2 and 2.A3).

The precipitation measurements used in this study vary slightly across sites due to differences in instrumentation availability and reliability. In the tropical western Pacific at the Nauru and Manus Island ARM sites, precipitation was measured with an Optical Scientific optical rain gauge (ORG815), and 1-hour averages surrounding radiosonde launches are analyzed in Section 2.3.2. Section 2.5 uses precipitation from a Vaisala WXT-520 at the INPA site in Manaus, Brazil (30-minute averages) for the analysis with GPS-derived CWV.

Section 2.4.2 assesses the robustness of the statistics presented as the horizontal resolution of the precipitation measurements decreases. We average precipitation from the Tropical Rainfall Measuring Mission's (TRMM) 3B42 version 7 product across various spatial scales. The 3B42 precipitation estimates (mm hr^{-1}) have a 3-hourly temporal resolution on a 0.25^{o} x 0.25^{o} grid, covering 50°S - 50°N from 01 Jan 1998 - present. The TRMM 3B42 precipitation estimates are a

combination of multiple independent precipitation estimates from various microwave retrievals and algorithms, while missing data in individual 3-hourly merged-microwave retrievals are filled with microwave-adjusted merged geo-infrared (IR) estimates. The precipitation radar (PR) and TRMM microwave imager (TMI) are used to calibrate all input microwave data, while the IR estimates are computed using monthly matched microwave-IR histogram matching (Huffman et al. 2007). Estimates of precipitation from the microwave instruments are derived from several versions of the Goddard Profiling Algorithm (GPROF), a multi-channel physical approach used to retrieve rainfall and vertical structure information (Kummerow et al. 2001). Over the oceans, GPROF uses signals from emission at low frequencies and scattering at higher frequencies. Over land, the algorithm reduces to a scattering-type procedure using only the higher-frequency channels. All of these estimates are adjusted to a best estimate using probability matching of precipitation rate histograms assembled from coincident data. Note that both the microwave and IR data are snapshots, except for small regions in which two or more overlapping microwave scenes are averaged. Generally, however, each satellite provides a sparse sampling of precipitation. As a result, there can be significant gaps in the 3-hourly coverage by passive microwave estimates. Because of this, precipitation estimates can be thought of as instantaneous values, representative of the 3-hour period in which they fall.

2.3 The Relationship between Deep Convection and CWV over Tropical Land vs. Tropical Oceans

2.3.1 *The GOAmazon Site - Manacapuru, BR*

To illustrate the relationship between CWV and deep convection at the GOAmazon site, we conditionally average precipitation rate by CWV in Figure 2.1. Figure 2.1a is the 1-hour

average precipitation rate conditioned on radiosonde CWV, with the average centered at the time of radiosonde launch. Measurements for all available times (01:30, 07:30, 13:30 and 19:30 LT,
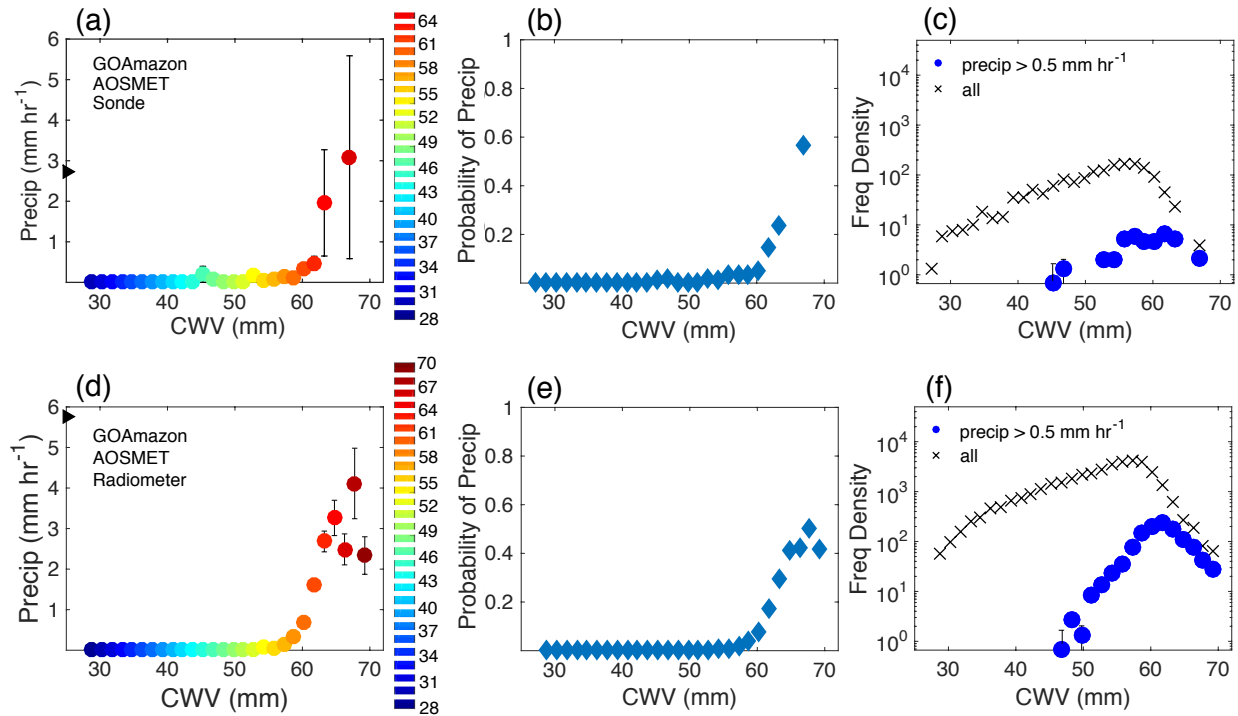
Figure 2.1: The relationship between precipitation and CWV at the GOAmazon site in Manacapuru, BR. (a) The 1-hour average precipitation (mm hr^{-1}) centered at the time of radiosonde launch conditionally averaged on CWV (mm). The mean of precipitating points greater than 0.1 mm hr^{-1} is 2.72 mm, given by the black triangle on the y-axis. (b) The fraction of observations per CWV bin with rain rates greater than 0.5 mm hr^{-1}, for radiosonde CWV. (c) The frequency density of all points and precipitating points with rain rates greater than 0.5 mm hr^{-1}, for radiosonde CWV. (d-f) Same as (a-c), except using 15-min average CWV from the microwave radiometer (MWR). The CWV bins for each set of analysis are given by their respective color bars. The highest bin for the radiosonde analysis has a width of 6 mm and a range from 64 mm to 70 mm, differing slightly from that of the radiometer data.

and occasionally 10:30 LT) were included in the averages. Note that for the statistics presented throughout, CWV bins are typically of equal 1.5 mm width and range from 28 mm to 70 mm; exceptions to this will be noted where appropriate, such as here, where the highest CWV bin spans 6 mm from 64 mm to 70 mm, to include sufficient counts.

Beyond a threshold CWV value, a sharp increase in rain rate is evident. This confirms that the CWV-precipitation relationship and associated behavior exists over tropical land as it does over tropical oceans (Peters and Neelin 2006; Neelin et al. 2009; Holloway and Neelin 2009). The

limited sampling of high CWV in the GOAmazon radiosonde observations, reflected in the large error bars (+/- 1 standard error), limits the precision with which the behavior above the pickup can be estimated; nevertheless, the data are sufficient to establish the occurrence of the pickup, and the radiosonde observations are key to analyzing the vertical structure, which will be discussed in Section 2.6 below.

The larger sample size of radiometer CWV affords better quantification of the behavior at high CWV (Figure 2.1d). For this purpose, Figs. 2.1d-f include four additional 1.5 mm bins at high CWV, in comparison to Figs. 2.1a-c. A sharp pickup is clearly evident in this dataset. Additionally, the conditionally averaged rain rates in the 61-64 mm range in Fig. 2.1a and the magnitudes observed in the 61-64 mm range of Fig. 2.1d mimic each other, demonstrating the robustness of the results across various instruments. A strong correlation (r=0.91) between the 15-minute average radiometer CWV and radiosonde CWV (see Fig. 2.A1) further highlights this consistency. Note that standard error bars in Fig. 2.1a,d reflect only the precipitation variance and number of counts in each bin as an estimate of sampling error, and do not account for potential errors in CWV estimation.

The value of CWV at which the rapid pickup in precipitation begins, referred to as the critical value, is a useful measure in characterizing this onset. For the short, in situ datasets used here, empirical fits involve relatively few points with large error bars, so we simply use the point at the beginning of the rapidly increasing range as a rule of thumb. Estimating the critical value by a linear fit through the range over which precipitation is rapidly increasing, as in Sahany et al. (2014), and choosing a range of above 1 mm hr^{-1} (appropriate for these data) yields a CWV value of ~60mm where the interpolation crosses 1 mm hr^{-1} (Fig. 2.1d). This range is, however, instrument dependent.

Compared to the results from Neelin et al. (2009), the mean tropospheric temperature at the GOAmazon site is 271.4 K, so the location of the pickup for GOAmazon occurs at lower CWV (~ 61 mm) than for comparable temperatures in the tropical eastern Pacific (~ 65 mm, interpolated between 271 and 272 K). This is consistent with the expectation that the mean tropospheric temperature is only one of several controls on conditional instability and thus the location of the pickup, and indicates that other key factors differing between tropical land and ocean are reflected in the onset. Specifically, boundary layer dynamics introduce additional complexity to the transition to deep convection over land, as the diurnal cycle is stronger over land and the partitioning of surface net radiation between latent and sensible heat fluxes depends on the interactions between several surface attributes (e.g., vegetation growth and soil moisture) and the atmosphere.

The curvature above the critical CWV in the radiometer analysis qualitatively resembles the behavior observed over the tropical oceans (Peters and Neelin 2006; Neelin et al. 2009), but we are cautious in drawing conclusions about this given the scatter at high values and limitations of the radiometer. The quantitative values of the conditionally averaged precipitation in the pickup region are slightly smaller than those in microwave retrievals in Neelin et al. (2009) and Sahany et al. (2014), presumably in part a result of inherent uncertainties at high rain rates, particularly in the satellite observations where precipitation is inferred from cloud liquid water. Comparing the 15-minute averages from the GOAmazon site to microwave retrievals over the tropical oceans (effectively snapshots) may also play a role.

Figures 2.1b and 2.1e illustrate an equally sharp increase in probability of precipitation as a function of CWV comparable to that shown for conditionally averaged rain rate in Figs. 2.1a and 2.1d, respectively. The fraction of precipitating points per CWV bin is defined as the number of

CWV observations with rain rates greater than a small threshold (here 0.5 mm hr^{-1}), divided by the total number of CWV samples in each bin. The probability increases dramatically above the critical value, sharply increasing to values greater than 50% in the highest CWV bins.

Figures 2.1c and 2.1f show the frequency of occurrence of different CWV values for all times and for precipitating times (where precipitation rates exceed 0.5 mm hr^{-1}) at the GOAmazon site for radiosonde and radiometer CWV, respectively. Curves are scaled with respect to CWV bin sizes, similar to a probability density function (PDF) but in counts per millimeter – referred to here as frequency density. We chose not to normalize to instead yield PDFs to make the counts for each bin visible, as the lengths of the available datasets vary by instrument and location. The peak in the distribution of CWV, for both the radiometer and radiosonde analysis, occurs between 55-60 mm. The occurrence of the peak in the distribution occurs just below the critical point, consistent with the findings of Peters and Neelin (2006) and Neelin et al. (2009). The highest probability state of the system is near the beginning of the intense precipitation regime, as is shown by the distribution of precipitating points (the peak occurs in the 61-62.5 mm bin in the radiometer analysis, and is slightly more spread out in the radiosonde data). Below 45 mm, no events exceeding the 0.5 mm hr^{-1} threshold are observed.

The longer-than-Gaussian tails of this distribution are also consistent with those seen in previous studies (Neelin et al. 2009; Neelin et al. 2010), seen here with different instrumentation. Because of the lower number of radiosonde observations, we focus on radiometer observations (Fig. 2.1f). Firstly, there is a long tail extending towards lower CWV in the distribution for precipitating points. The peak occurs just below or near the critical point, with a sharp decrease in frequency towards higher CWV in the region of rapid pickup of precipitation, consistent with the dissipative effects of precipitation on CWV (and of convection on buoyancy). Beyond the critical

value, there is evidence of a long tail with roughly exponential decay as CWV increases, suggesting that the system is characterized by a higher frequency of extremes than would be expected from Gaussian statistics. This behavior is particularly evident in the radiometer analysis shown in Fig. 2.1f, but low counts in the high CWV bins and measurement uncertainty limit confidence in this feature.

Many of the onset statistics can be qualitatively and quantitatively captured by a simple stochastic model (Stechmann and Neelin 2011). This model suggests that the long tail for precipitating points in the low CWV regime is associated with a transition probability in which it typically takes some time to transition to a non-raining state when CWV decreases from the raining regime. The same hysteresis affects the position and value of the peak in the distribution for precipitating points, consistent with results here, suggesting it may be interesting in further work to distinguish temporal aspects of the transition, including distinguishing precipitating shallow and congestus convection or the formation of stratiform rain from deep precipitating convection (Ahmed and Schumacher 2015), as this is also a possible explanation of such characteristics of the distribution. The behavior of the distribution for all points at low CWV is expected to be rather dependent on the dynamics of the dry regime and has been noted to have various forms over ocean basins, including a second maximum. This may occur near the balance between evaporation and moisture divergence (Lintner and Neelin 2009).

2.3.2 *The Tropical Western Pacific*

Figure 2.2 illustrates the CWV-precipitation relationship for two sites in the tropical Western Pacific - Nauru (Fig. 2.2a-c) and Manus Island (Fig. 2.2d-f). Compared to the Amazon in Fig. 2.1, the tropical western Pacific sites show very similar behavior. Radiosonde estimates are shown in Fig. 2.2, which can be directly compared to Fig. 2.1a-c. Both pickups of precipitation,

for Nauru (Fig. 2.1a) and Manus Island (Fig. 2.1d), occur at higher values of CWV (~67 mm) than in the Amazon. As was discussed in Section 2.3.1, this is due in part to small differences in the
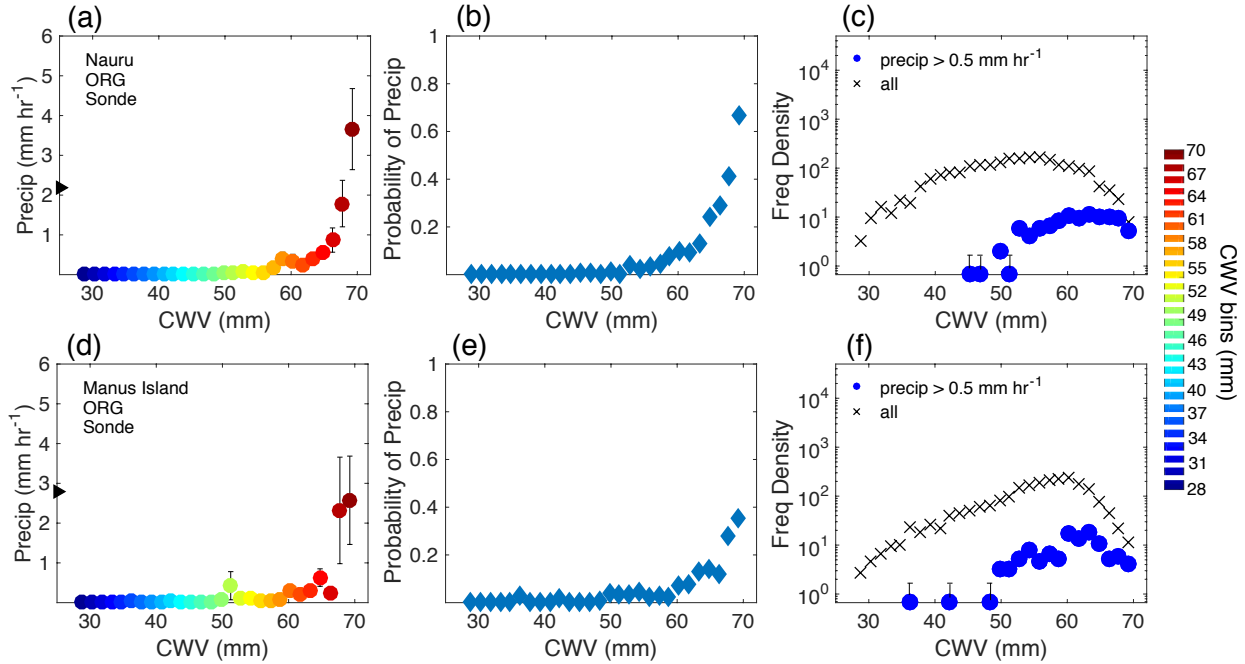
Figure 2.2: Same as Fig. 2.1, but for the relationship between precipitation and radiosonde CWV at Nauru (a-c) and Manus Island (d-f) in the tropical western Pacific. The mean of precipitating points greater than 0.1 mm hr^{-1} is 2.18 mm hr^{-1} for Nauru and 2.78 mm hr^{-1} for Manus Island. CWV bins are the same as in Fig. 2.1d-f (see color bar).

mean tropospheric temperatures (272.0 K at Nauru, 271.9 K at Manus Island) but is also likely due to fundamental differences in the convective environments of a tropical land site vs. a tropical oceanic site. For reference, the values of column integrated saturation specific humidity ($\widehat{q_{sat}}$) for the three sites are 76.0 mm, 75.2, and 73.0 mm at Nauru, Manus Island and the GOAmazon site, respectively, although it is known for tropical ocean basins spanning a wider range of tropospheric temperatures that $\widehat{q_{sat}}$ poorly captures the temperature dependence (Neelin et al. 2009, Sahany et al. 2012) because the relevant physical control is conditional instability rather than large-scale saturation.

As in the GOAmazon case, the fractions of precipitating points (Figs. 2.2b and 2.2f, for Nauru and Manus Island, respectively) sharply increase to 50% or greater beyond a critical CWV. This, again, illustrates that a sharp transition occurs not only in rain rate, but also in the probability of precipitation beyond a threshold CWV. In Fig. 2.2f, Manus Island exhibits distinct peaks in its distributions: the peak of the CWV distribution occurs between 58 and 60 mm, whereas the peak in the distribution of precipitating points occurs between 60-63 mm. This is consistent with the findings from previous studies, where the peak in the precipitating points occurs at slightly lower CWV than the critical value. Also consistent is the sharp decrease in the frequency of CWV between the distribution peak and the CWV values where precipitation picks up rapidly. These characteristics are also observed for Nauru, but the peaks in the distributions of CWV and the precipitating points are broader in this sample from radiosondes, i.e., the CWV distribution peak spans roughly 8 mm (~50-58 mm), whereas the peak in the distribution of precipitating points spans roughly 10 mm (~57-67 mm).

Even though marginal differences can be observed across locations, the main features of these statistics are consistent and robust across all three tropical locations. Though these statistics were not examined near regions of strong topographic forcing, land-sea contrasts or other inhomogeneity, it has been suggested that these complexities can impact the statistics (Bergemann and Jakob, 2016), as additional processes driving deep convection in these regions are not adequately captured with proxies such as CWV or column saturation. Nevertheless, the results presented here suggest that CWV is a good proxy for conditional instability and has a clear relationship to the onset of deep convection throughout much of the tropics.

2.4   The robustness of the observed statistics at various scales

2.4.1   *The effects of temporal averaging*

To explore how averaging over differing temporal scales can affect the statistics describing

the transition to deep convection, we compute the transition statistics at various averaging intervals

with in situ precipitation and radiometer CWV from the GOAmazon site. Four averaging intervals

were chosen for this analysis: 15-min, 1-hour, 3-hour and daily averages. These intervals were

chosen to be most comparable to the current output available from models and observations.
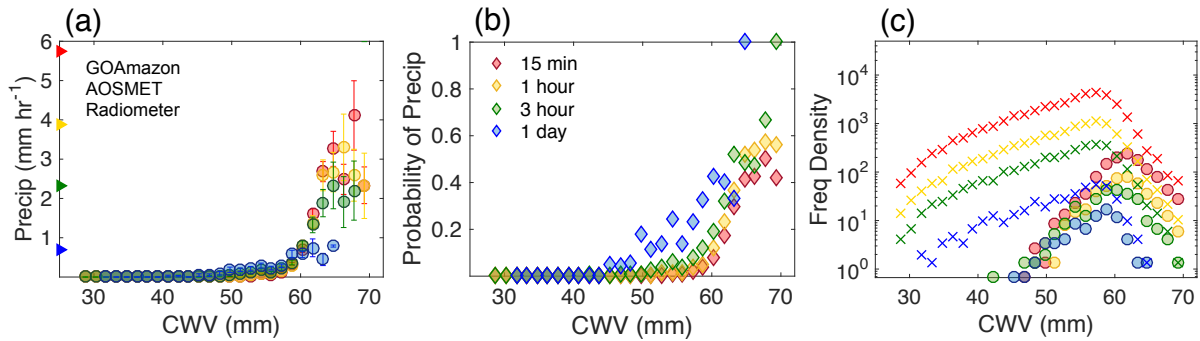
Figure 2.3: Same as Fig. 2.1d-f, using in-situ precipitation and radiometer CWV from the GOAmazon site, but with additional averaging intervals: 15-min averages (red); 1-hr averages (yellow); 3-hr averages (green); daily averages (blue).

In Fig. 2.3a, the magnitude of the conditionally averaged precipitation in the highest four

CWV bins diminishes considerably as the averaging interval increases. Up to and including 3-

hourly averages, the magnitude and sharpness of the pickups are largely preserved. Beyond 3

hours, the pickup is noticeably degraded. However, adapting the scale of the precipitation to the

decrease in resolution (not shown) illustrates that despite the decreased sharpness of the pickup,

the precipitation still increases with increasing CWV. Despite some variability in the shapes of the

curves, the overall locations of the pickups are robust for temporal resolutions of 3 hours or less.

The location of the probability curve pickup in Fig. 2.3b, however, varies substantially as the size

of the averaging interval increases: larger averages pick up sooner and have a higher probability
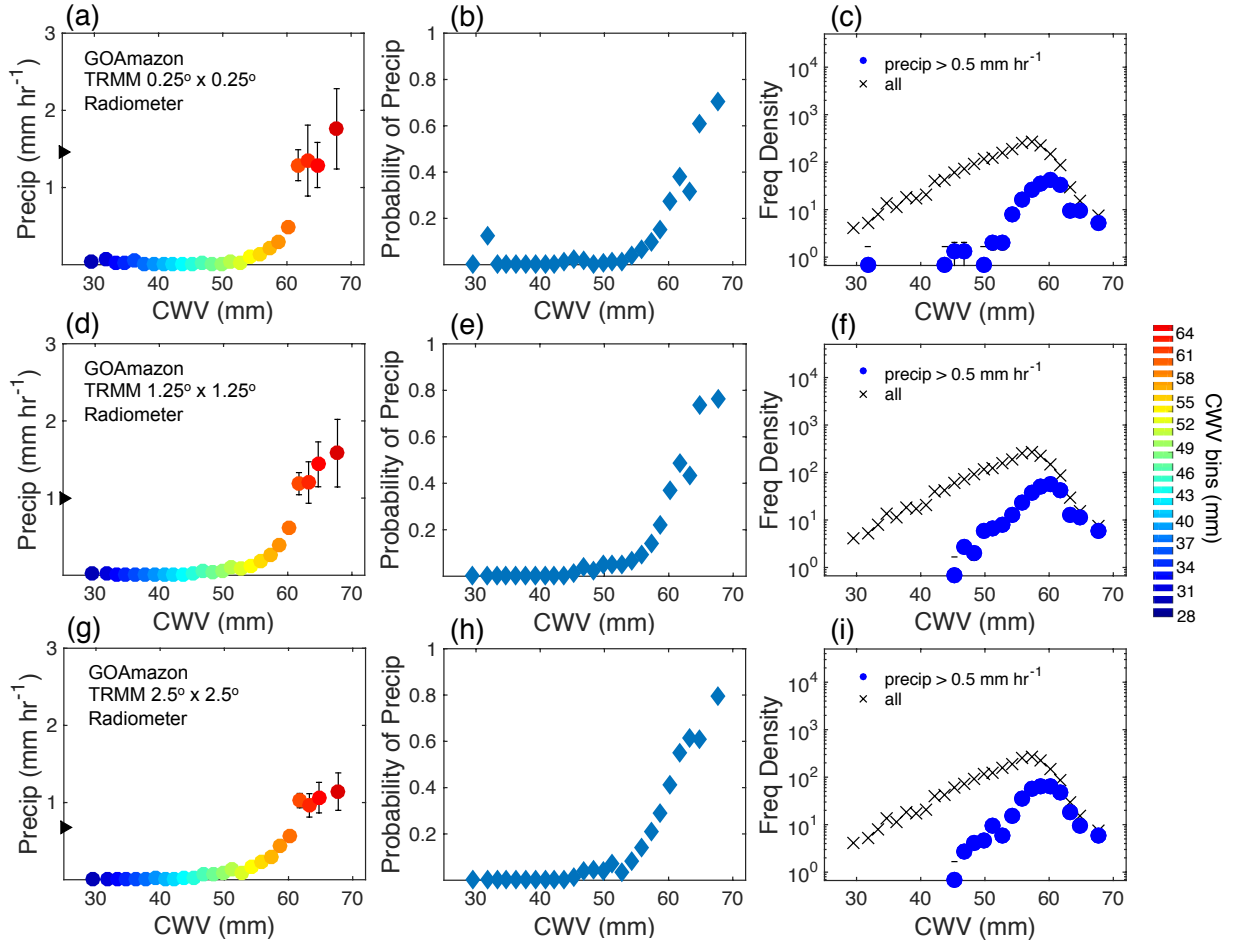
Figure 2.4: Same as Fig. 1d-f, but instead using area-averaged TRMM 3B42 3-hourly instantaneous precipitation at varying resolution from the grid box that includes the GOAmazon site; CWV values are derived from the 15-min averages of MWR data surrounding the TRMM snapshot. (a-c) for precipitation at 0.25° x 0.25° horizontal resolution (grid box over GOAmazon site); (d-f) spatial average of precipitation at 1.25° x 1.25° around GOAmazon site ; (g-i) same as (d-f) but for 2.5° x 2.5°.

of precipitating at high CWV. This can be explained by the fact that the 3-hourly and daily averages are more likely to span times when it is raining than the shorter averages are. The overall shape of the distribution is preserved with averaging (Fig. 2.3c), but the mean shifts to lower CWV and the tails of the distribution are shorter. Overall, these results illustrate how the statistics vary with temporal resolution, which should be considered when applying them as model diagnostics.

2.4.2 *The effects of spatial averaging*

The relationship between spatially averaged TRMM 3B42 3-hourly instantaneous precipitation (see Section 2.2) and radiometer CWV (15-min averages) over the GOAmazon site is shown in Figure 2.4 for 0.25 x 0.25 degrees (a-c), 1.25 x 1.25 degrees (d-f), and 2.5 x 2.5 degrees (g-i). At either 0.25° or 1.25°, the relationship is comparable to the results in Fig. 2.1 and thus robust. However, at 2.5°, it starts to deteriorate, as the pickup of precipitation and the percentage of precipitating points occur too soon in comparison to Fig. 2.1d-e. These results are encouraging, as they suggest that resolutions up to about 1.25 x 1.25° are still of sufficient spatial resolution to reproduce robust statistics that explain the CWV-precipitation relationship, given that the temporal resolution is also adequate. This implies that these statistics are reproducible using the horizontal resolutions available with many current generation GCMs. In such comparisons, it should be borne in mind that a GCM with, e.g., 2° resolution may respond at the finest scale available to it, i.e. the grid scale, in a manner similar to the convective response occurring at finer scales in observations.

2.5   Use of GNSS Meteorological Networks in the Tropics

For two decades, GNSS/GPS meteorology has offered relatively inexpensive, high-frequency (~5 min), all-weather retrievals of CWV, and is thus ideal for analyses requiring long, continuous records of observed CWV over land. This is particularly useful for studies in the tropics, where collecting in situ measurements is a challenge. We thus evaluate the convective transition statistics here for GPS data from a site in Manaus. In Figure 2.5, the statistics are reproduced for GPS CWV and coincident measurements of precipitation (30-minute averages) as in Fig. 2.1. Note that the precipitation measurements from the INPA site are biased low (see Appendix). Therefore, for better comparison to the statistics in Fig. 2.1, the range shown on the precipitation axis (0-1.28 mm hr^{-1}) is reduced relative to the range on the other pickup plots (0-6

mm) by a factor of 4.7 – the ratio of means of precipitating points between the 30-minute average precipitation from both sites. Additionally, the threshold for identifying precipitating points is lowered to 0.1 mm hr^{-1} to more appropriately complement the 0.5 mm hr^{-1} threshold used in Fig. 2.1. When measurement differences are properly accounted for, Figs. 2.1 and 2.5 compare well: the location and shape of the pickup of precipitation is consistent, the probability of precipitation is just below 50% in the highest bin, and the distribution of CWV and precipitating points resides near the transition, with a sharp drop in frequency between the peak and the transition and a long tail extending out to high CWV. This suggests GPS technology will be valuable in observing characteristics of convection at high temporal resolution throughout tropical land regions.
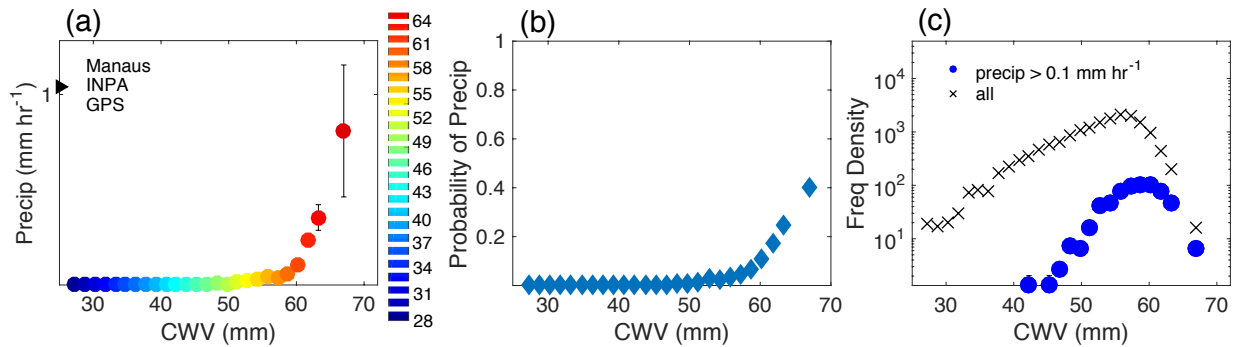
Figure 2.5: Same as Fig. 2.1a-c, but using in-situ precipitation (30-min averages) binned by 30-min GPS-retrieved CWV from a site at the INPA in Manaus, BR. The triangle in (a) denotes the mean of precipitating points > 0.1 mm hr^{-1}, which is 1.04 mm hr^{-1}. Note the change in the precipitation axis in comparison to Fig. 2.1a,d and the change in threshold value used in Fig. 2.5b,c. The rain gauge at the INPA is biased low (see Appendix), and thus to allow for direct comparison to the GOAmazon case, the range on the precipitation axis defined in Fig. 2.1a,d (0 − 6 mm) is decreased here by a factor of 4.68, the ratio of the means between the AOSMET gauge and the INPA gauge.

2.6   Characterizing the variability of column moisture

2.6.1   *Vertical thermodynamic profiles*

Vertical profiles of thermodynamic quantities – specific humidity (q), relative humidity (RH) and equivalent potential temperature (θ_e) – are conditionally averaged on CWV in Figs. 2.6a, 2.6b, and 2.6c, respectively. In Fig. 2.6a, it is evident that profiles of q are most variable in the layers above 800 mb at the GOAmazon site. This differs slightly from the western Pacific case, as

the variability in free tropospheric q (850-500mb) with respect to CWV is slightly less over the Amazon than it is for Nauru (see Figure 3a Holloway and Neelin 2009), presumably due to stronger horizontal moisture gradients near Nauru (see Lintner et al. 2011). Additionally, the contribution from the boundary layer is greater at the GOAmazon site with a ~ 4 g kg^{-1} difference in humidity between the lowest and highest bins at 975 mb (Fig. 2.6a), whereas the difference is lesser at Nauru.
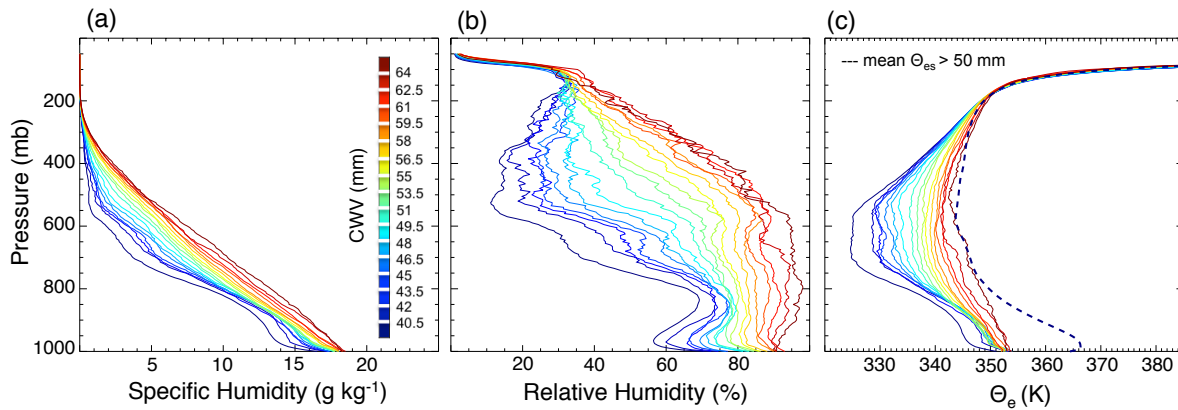
Figure 2.6: Vertical profiles of (a) specific humidity (g kg^{-1}), (b) relative humidity (%), and (c) equivalent potential temperature (K) measured or derived from radiosonde data collected at the GOAmazon site and conditionally averaged by CWV (mm). The mean saturated equivalent potential temperature (θ_{es}, K) for profiles greater than 50 mm is shown in the dashed line in (c).

RH profiles (*RH* with respect to water) belonging to the highest CWV bins at the GOAmazon site (> 61 mm) are at least 90% saturated throughout the lower troposphere. At Nauru, this is the case for CWV greater than 66 mm (see Fig. 4a, Holloway and Neelin 2009), suggesting that the column is saturated for lower CWV in the Amazon than it is over the tropical western Pacific. Additionally, the boundary layer *RH* is roughly twice as variable over the Amazon as it is over Nauru, ranging from a ~ 35% difference at 975 mb between the highest and lowest bins versus a ~15% difference at Nauru. The variability observed in *RH* is highly consistent with variability in column moisture, since free tropospheric temperature variations tend to be modest.

Equivalent potential temperature (θ_e), calculated reversibly following Emanuel (1994) in Fig. 2.6c, is an approximate measure of non-entraining parcel buoyancy, as convective available potential energy (CAPE) can be approximated by drawing a vertical line upward from the initial θ_e. Where this line crosses the θ_{es} curve is roughly the level of free convection (LFC) of the unmixed parcel; the area to the left of the vertical line and to the right of the θ_{es} curve is roughly proportional to CAPE. θ_e at the GOAmazon site shows similar overall variability in the vertical as it does at Nauru. In the absence of entrainment, many of the profiles belonging to the highest CWV bins have sufficient θ_e to support deep convection, providing that the convective inhibition (CIN) residual from the nighttime hours (seen in the θ_e profile) could potentially be overcome. This will be discussed further in Section 2.7.
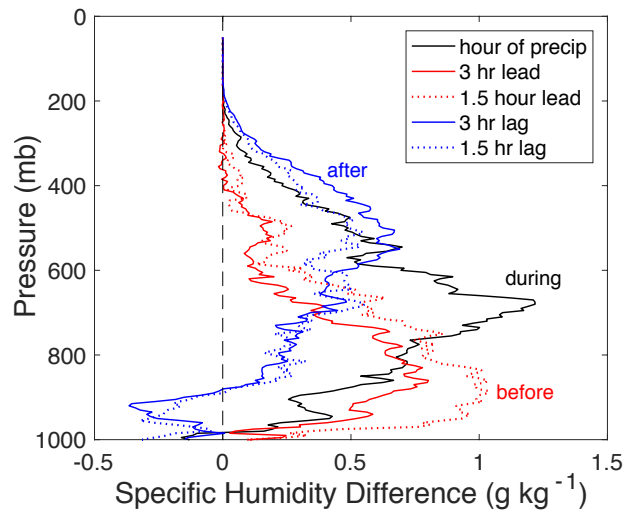
Figure 2.7: Profiles of specific humidity differences (g kg^{-1}) from radiosonde measurements at the GOAmazon site between precipitation events (1-hour average rain rates > 0.5 mm hr^{-1}) and no precipitation events (1-hour average rain rates < 0.01 mm hr^{-1}) for 1.5-3 hours leading precipitation (red), within the hour of precipitation (black), and 1.5-3 hours lagging precipitation (blue). Results are shown for Jan-Apr only (2014-2015).

2.6.2 *Moisture anomalies*

Figure 2.7 illustrates the differences in q at 1.5-3 hours leading (red) and 1.5-3 hours lagging (blue) precipitation, between profiles corresponding to precipitation events (rain rate > 0.5

mm hr^{-1}) and those that do not correspond to a precipitation event (rain rate < 0.01 mm hr^{-1}) for January-April soundings only. Leading an event, moisture anomalies exceeding 0.5 g kg^{-1} and as large as 1 g kg^{-1} are seen clearly throughout the lower troposphere, with a particularly large increase between 750-950 mb. This is consistent with evidence that increased low-tropospheric humidity supports deep convective initiation. These moisture anomalies are also seen in the tropical western Pacific at Nauru (Fig. 5, Holloway and Neelin 2009), where anomalies as large as 3 g kg^{-1} occur in the lower-mid troposphere within 3 hours of a precipitation event. The anomaly in the lower-most layer at the GOAmazon site is, however, more distinct from and almost as large as the anomaly within the hour of rainfall compared to the anomalies at Nauru, which show a consistent vertical structure at all times leading and lagging rainfall. This illustrates the greater moisture variability in the boundary layer over land preceding convection. It can be seen at both sites, however, that a distinct increase in moisture is present in the lower troposphere. There are likely multiple causes of this moistening in the lower troposphere preceding convection at both locations, including mixing and detrainment of water from shallow cumulus convection, in concert with convergence or lifting. Regardless of the cause, it will become evident in the next section as we examine the role of entrainment that sufficient lower free tropospheric moistening is essential to the onset of deep convection.

During a precipitation event, the anomaly in the 750-950 mb layer decreases, suggesting that moist air is lofted by updrafts, with drier air from downdrafts diluting the layer's moisture content. The increased anomaly of mid-upper tropospheric humidity between 200-700 mb is likely due to the effects of convection via some combination of lofting and detrainment of moist air, and large-scale ascent induced by convective heating, potentially including stratiform effects. As precipitation dissipates, this mid-upper tropospheric anomaly persists for hours afterwards, which

may aid in supporting subsequent convective events. These anomalies are present in the tropical western Pacific case as well, but the vertical structure is more consistent throughout the 6-hour period than it is for the GOAmazon case, i.e. the maximum q anomaly at all times is around 800 mb. In the GOAmazon case, on the other hand, the maximum 1.5 hours before precipitation is found around 900 mb, during precipitation it is around 700 mb, and after precipitation it is found at about 500 mb. Additionally, separating the analysis out by time-of-day (not shown) indicates that these moisture anomalies are consistent for events occurring at all times of day.

Overall, in both the Amazon and the tropical western Pacific, humidity is enhanced throughout most of the troposphere for several hours leading and lagging the original precipitation event. Free tropospheric humidity appears to behave similarly in land and ocean cases (although with larger amplitude variation in the Western Pacific), whereas boundary layer moisture is more variable on short time scales in the land case. The Amazon also more clearly exhibits upper tropospheric moisture anomalies in the hours following precipitation, while both the Amazon and western Pacific exhibit reduced boundary layer moisture.

2.6.3 *Dependence on Time-of-Day*

Considering the strength of the diurnal cycle over land, it is natural to wonder whether CWV is a good proxy for conditional instability at all times of day, given how conditions contributing to instability can vary diurnally. Fig. 2.8 suggests that the relationship between CWV and precipitation is robust at all times of day. Figure 2.8a shows the relationship between 15-min average radiometer CWV and precipitation for nighttime hours (7 pm – 8 am). The time intervals were chosen to complement the radiosonde launch times and the analysis presented in Section 2.7. Figure 2.8d shows this relationship for the midday hours, which are the most convective hours of the day (10 am – 4 pm). The pickups of both conditionally averaged precipitation (Figs. 2.8a and

2.8d) and the probability of precipitation (Figs. 2.8b and 2.8e) affirm that the relationship is robust throughout all times of day. The frequencies of occurrence of precipitation (Figs. 2.8c and 2.8f) are also consistent with the results in Fig. 2.1. Despite the fact that more convection occurs in the midday hours over the Amazon, the relationship holds true for all times of day.
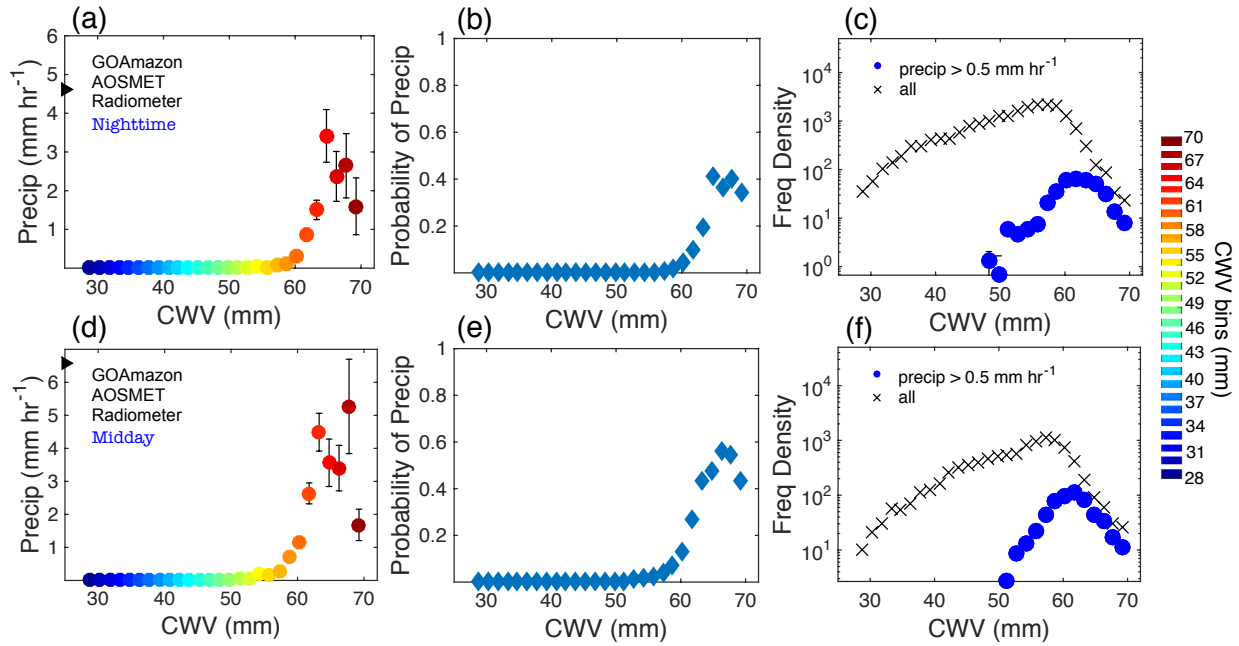
Figure 2.8: Same as Fig. 1d-f, except for (a-c) nighttime hours (8 pm – 7 am), and (d-f) midday hours (10 am – 4 pm) only.

2.7   The sensitivity of plume buoyancy to entrainment under simple freezing assumptions

In this section, we focus on connecting the observed pickup of precipitation to observed increases in buoyancy and the sensitivity to entrainment. We calculate the buoyancy perturbation profiles, the virtual temperature difference between the environment and the plume $\left(\Delta T_v = T_{v,plume} - T_{v,env}\right)$ for plumes rising from the subcloud layer (1000 hPa), with mixing occurring at each pressure level as described by

$$r_k = (1 - X_{k-1})r_{k-1} + X_{k-1}\tilde{r}_{k-1} \qquad (1)$$

where X is the mixing coefficient, r is a conserved variable (with $\tilde{r}$ its environmental value), and k denotes pressure level if X varies. Here we calculate the mixing coefficient proportional to z^{-1}, where z is height, in the layer in which plume mass flux is growing. This mixing assumption was referred to in Holloway and Neelin (2009) as Deep-Inflow-A (DIA) and corresponds to the Siebesma et al. (2007) LES-based dependence. DIA is chosen here because of its realistic representation of buoyancy perturbation profiles and overall consistency with the pickup of precipitation observed in Fig. 2.1, and is described as

$$X_k = c_\in z_k^{-1} \Delta z \tag{2}$$

where X_k is the coefficient in (1), Δz is a positive finite difference layer depth, and $c_\in = 0.4$. Following Holloway and Neelin (2009), a simplified limiting case of freezing microphysics is also used: all condensate is conserved and freezing is assumed to take place very rapidly when the parcel reaches the freezing level.

The individual perturbation profiles are shown in Figure 2.9 and have been conditionally averaged by CWV, with bin spacing as in Fig. 2.1a. Figure 2.9a illustrates the profiles of the radiosondes from all times of day. It is evident that only the highest CWV bins could be convective through a deep layer, as both the CIN (between the surface and ~850 hPa) and reduced buoyancies in the mid-upper troposphere are more likely to inhibit deep convection at lower CWV. Since the afternoon is the most convective time of day in the Amazon (Machado et al. 2004), we also separate the profiles by time-of-day to examine key thermodynamic differences and how stability in the nighttime hours could be contributing to the CIN observed in Fig. 2.9a.

Figure 2.9b, which includes nighttime soundings only (01:30, 07:30 and 19:30 LT), shows the larger layer of CIN seen in Fig. 2.9a, which suggests that this CIN is most characteristic of the nighttime soundings. At these times of day, it is unlikely for convection to fire as a result of
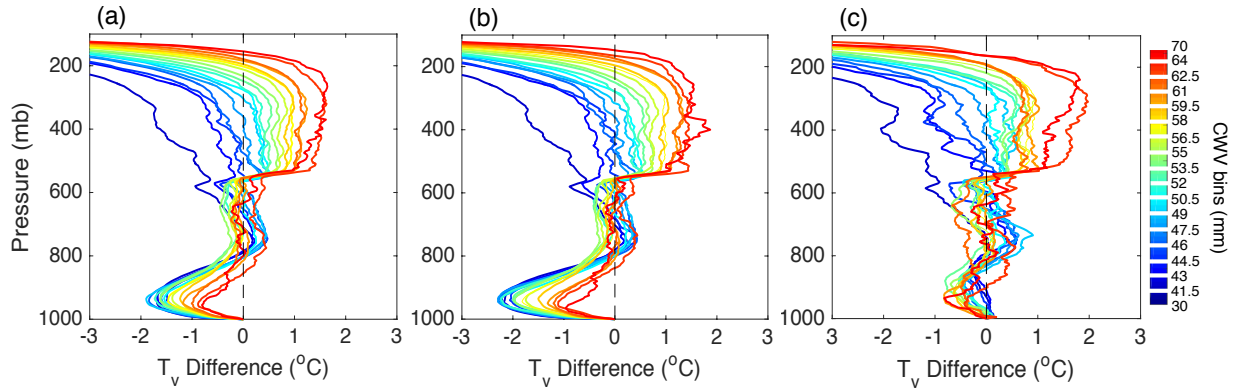
Figure 2.9: Virtual temperature (T_v) difference between the parcel (computed with Deep-Inflow-A mixing) and the environment, binned by CWV. CWV bins are 1.5 mm in width (shown in the color bar), with the highest bin spanning 64-70 mm and the lowest bin spanning 30-41.5 mm. Plume buoyancy differences are shown in (a) for all times of day, (b) for nighttime soundings (19:30, 01:30, 07:30 LST) soundings only, and (c) for midday (10:30, 13:30 LST) soundings only.

local instability, but the profiles at high CWV appear supportive of deep convection if forced (Fig. 2.9b). In Figure 2.9c, only profiles from late morning (10:30 LT) and early afternoon (13:30 LT) soundings were conditionally averaged by CWV. In contrast to the evening/morning soundings, there is very little CIN. The variability observed in the upper CWV bins is due to the low counts of profiles contributing to the average. Overall, it appears that a variety of CWV values would be conducive to convective activity in the afternoon hours, with CWV bins < 60 mm acting to support shallow convection, whereas only the highest CWV bins act to support deep convection.

The entrainment calculations suggest that CWV has a causal effect on deep convection, but they do not indicate the extent to which this effect dominates the observed relationship. Evidence suggests that CWV can also co-vary with convective precipitation (Raymond et al. 2015). A concurrent study evaluating causality with modeling experiments (Y.-H. Kuo et al. 2016, personal communication), shows that without sufficient entrainment the pickup behavior observed in the relationship between precipitation and CWV (Figs. 2.1 and 2.2) does not occur.

Some caveats on this analysis should be noted:

(1) The plume buoyancies sorted by CWV are considerably smaller in the lower troposphere compared to the tropical western Pacific case for the same computation (Holloway and Neelin 2009, Fig 2.8c). The onset of deep convection is thus likely dependent upon other factors unique to tropical land cases, in particular the greater variability of the boundary layer, as both sensible and latent heat fluxes are more variable. Additionally, there are key thermodynamic differences between the convective environments in the wet and dry seasons in the Amazon and thus likely differing thermodynamic controls on deep convection; i.e. during the wet season, there is less CIN, less CAPE and more moisture available throughout the column, whereas in the dry season there is more CIN, more CAPE and less moisture available in the column (Collow et al. 2016).

(2) Entrainment assumptions can affect the details of the buoyancy profiles seen in Fig. 2.9c. In particular, smaller/larger values of the mixing coefficient in the lower troposphere yield larger/smaller buoyancy values. Here it is useful to use a scheme that has already been applied to corresponding soundings at the western Pacific ARM site, but one could evaluate in further work whether there is evidence for differences in entrainment characteristics for deep convection over land in comparison to the ocean. More complex entrainment assumptions would obviously also have an impact, e.g., rescaling the entrainment from the cloud base (de Rooy et al. 2013; Bechtold et al. 2014), the entrainment rate weakening as convection over land deepens (Del Genio and Wu 2010; Stirling and Stratton 2012), having a parameterized dependence on environmental humidity (Zhang and Klein 2010; Stirling and Stratton 2012) or a dependence on cloud size (Simpson 1971; Grabowski 2006; Khairoutdinov and Randall 2006; Stirling and Stratton 2012). However, the computations here indicate a strong dependence on free tropospheric humidity can be found even with fixed entrainment.

(3) Associated with the smaller buoyancy in the lower free troposphere compared to the oceanic case, the role of freezing is more important to occurrences of positive buoyancy in the upper troposphere. If freezing is completely omitted, the jump in buoyancy seen near 550 mb in Fig. 2.9 does not occur, and profiles in the upper troposphere decrease slightly faster with height, yielding little buoyancy even in the high CWV cases. Microphysical differences are known to exist in continental vs. maritime deep convective clouds: robust mixed-phase processes dominate continental convection, whereas maritime deep convection rarely involves vigorous microphysical processes in mixed-phase regions, although ice processes are still important (Rosenfeld and Lensky, 1998; Xu and Zipser, 2012). Proper representation of microphysical processes in models can affect simulation of clouds and precipitation (Khain et al. 2015; Zhang and Song, 2016), and these processes can be significantly altered by different concentrations of aerosols (Andreae et al., 2004; Rosenfeld et al., 2008; Grabowski and Morrison, 2016). Empirically examining the effects of ice microphysics on buoyancy in various convective environments of the tropics is thus of interest for future work.

The discussion of caveats above points to some interesting aspects in which representation of deep convection over tropical land can be expected to be more sensitive than over the ocean. The additional involvement of the boundary layer is no surprise. However, the dependence of the deep convective instability through the upper troposphere on contributions to buoyancy from the freezing process over land, even under highly favorable conditions (sufficient free tropospheric water vapor and at a favorable time of day), points to a potentially greater sensitivity to freezing microphysics than over ocean. These sensitivities will be addressed in future work. Nonetheless, the overall results for the leading order effects of lower free tropospheric water vapor on convection in the Amazon have striking parallels to the oceanic case.

2.8   Conclusions

This study compares and contrasts the relationship between CWV and deep convection in the Amazon to that in the tropical western Pacific using measurements from two neighboring sites at each location: specifically, results from the GOAmazon site in Manacapuru, BR and the GNSS site at INPA in Manaus, BR are compared to results from the DOE ARM sites at Nauru and Manus Island. The relationships evident at all locations are robust, with an increase in conditionally averaged rain rate as a function of CWV. The probability of precipitation often increases beyond 50% in the highest CWV bins. The distribution of CWV is consistent with the distributions observed in microwave retrievals over ocean (Neelin et al. 2009) for both precipitating points and all points, with the distribution for precipitating points peaking just below the critical value at which precipitation increases sharply, and decreasing rapidly over the pickup region. All cases with sufficient data counts are consistent with a longer-than-Gaussian tail extending out to high CWV. Much of the variability in column moisture is due to variability in free tropospheric humidity, suggesting that the onset of deep convection is strongly dependent on free tropospheric humidity at tropical land sites, much like over tropical ocean sites.

The relationship between CWV and precipitation is generally robust across time-of-day. While there is a smaller fraction of precipitating points of a given CWV in nighttime hours compared to those occurring near midday, the conditionally averaged precipitation exhibits a very comparable pickup that increases beyond a threshold value of CWV. Thus, while the probability of nighttime precipitation likely depends on boundary layer factors, CWV remains an important proxy for the effects of lower free tropospheric water vapor on deep convection.

Because convection occurs at small time and space scales, spatial and temporal averaging can degrade the statistics describing the transition to deep convection. In daily averages, a highly

smoothed version of the behavior may still be seen, but much information about the underlying physics - particularly the sharp onset of conditional instability associated with deep convection - is largely lost. Daily averages are thus suboptimal for examining this behavior over both land and ocean, and their use for such an analysis is not recommended. Examining these statistics at various averaging intervals closer to the appropriate time scales for convection indicates that the pickup curves are robust over averages from 15 minutes to 3 hours. One-hour averages yield results very similar to 15-minute averages, while 3-hour averages slightly reduce the sharpness of the pickup. Similarly, using satellite retrievals of precipitation for a region surrounding the GOAmazon site at different spatial resolution yields convective transition statistics that reasonably reflect the in situ observations at 0.25° resolution, but the sharpness of the pickup of precipitation becomes smoothed as the domain of the spatial averaging increases.

Examining the temporal and vertical structure, lower tropospheric moisture increases prior to convection and precipitation at the GOAmazon site. This is consistent with findings for the tropical western Pacific ARM sites (Holloway and Neelin 2009). However, for the land case the lower tropospheric moisture is more variable in time and there are clear indications that moisture has been lofted following the convection, whether by the detrainment of water at various levels during the convective event or by heating and stratiform processes. After convection, the sub-cloud layer becomes cooler and slightly drier over both land and ocean. The before-and-after moisture profiles in this tropical land case thus illustrate the two-way interaction between convection and water vapor, with increases in lower tropospheric water vapor prior to convection consistent with impacts on buoyancy in entraining convection.

The latter impacts are tested by computing buoyancy profiles with a previously used profile of turbulent entrainment, which are then conditionally averaged by CWV to assess whether

buoyancy through a deep convective layer is comparable to the onset of precipitation as a function of CWV. This is examined for soundings from all times of day, and for nighttime and midday ensembles of profiles separately. For nighttime conditions, CIN may be an additional control, although the CIN is considerably smaller for the highest CWV values. The nighttime results may point to the presence of pre-existing disturbances or boundary layer conditions not captured by CWV. The midday soundings show buoyancies sufficient for shallow convection over a middle range of CWV. However, only the highest CWV bins would be convective through a deep layer for each case – nighttime, midday and all times – consistent with the pickup of precipitation. Some differences relative to the ocean are worth noting: there are likely greater contributions from the boundary layer to the conditional instability of the environment that cannot be sufficiently explained by variability in CWV, and there is evidence that freezing microphysics exerts greater influence on the development of buoyancy above the freezing level. Nevertheless, the dependence of deep convective onset on free tropospheric humidity is robust and of leading order over both tropical land and tropical ocean.

2.A   Appendix

To illustrate the consistency between radiometer CWV and radiosonde CWV, Fig. 2.A1 shows 15-min average radiometer CWV scattered against radiosonde CWV. CWV is thus sampled every 6 hours within the period 10 Jan - 30 Sep 2014. It is evident that there are no systematic biases observed at high values of CWV, which could have resulted from interpolation or measurement inaccuracy. Overall, while our ability to confirm consistency between instruments is limited to the sampling of the radiosondes, it is evident from this sample that the CWV values agree well across instruments.
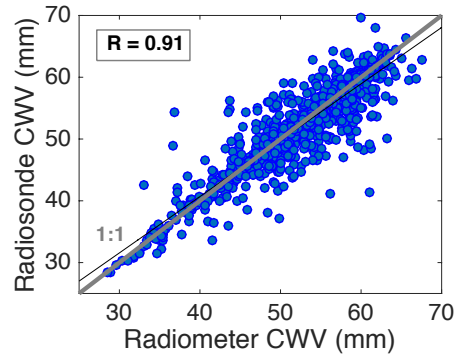
Figure 2.A1: The relationship between radiometer CWV and radiosonde CWV for 10 Jan 2014 – 31 Jul 2014. The correlation coefficient (R) is 0.91.

Figure 2.A2 shows the probability density functions (PDFs) of the precipitating points using five precipitation datasets used throughout this study: AOSMET at the GOAmazon site, ORG at Nauru, ORG at Manus Island, TRMM, and the dataset from INPA in Manaus, Brazil coincident with the GPS CWV measurements. It is evident that the PDFs of the precipitation data from the GOAmazon site, Nauru, and Manus Island are all consistent with one another, whereas the TRMM and INPA datasets are biased low, with much lower probability of high rain rates (Fig. 2.A2a). This contributes to differences in the magnitudes of the pickup curves between those seen in Fig. 2.4 (TRMM) and Fig. 2.5 (INPA), in comparison to Figs. 2.1 and 2.2. The TRMM data in Fig. 2.4 require a unique precipitation axis to those of Figs. 2.1 and 2.2, since these data have a different spatial footprint than all others used in this study. Fig. 2.5, on the other hand, adopts an axis that is scaled according to the ratio of 30-minute mean INPA data and 30-minute mean radiometer data. This value (4.68 mm hr^{-1}) is divided by the range used in Figure 2.1d (6 mm hr^{-1}) to instead yield a range of 1.28 mm hr^{-1} for the axes in Fig. 2.5. It is also apparent that the PDFs of the precipitation datasets at Nauru, Manus Island, and the GOAmazon site all exhibit power law behavior (Fig. 2.A2b) out to high precipitation (~40 mm hr^{-1}), after which point the distribution

drops off exponentially. The exponent of the power law range is approximately -1.25, while the decay scale of the exponential range is roughly 26 mm hour^{-1}.
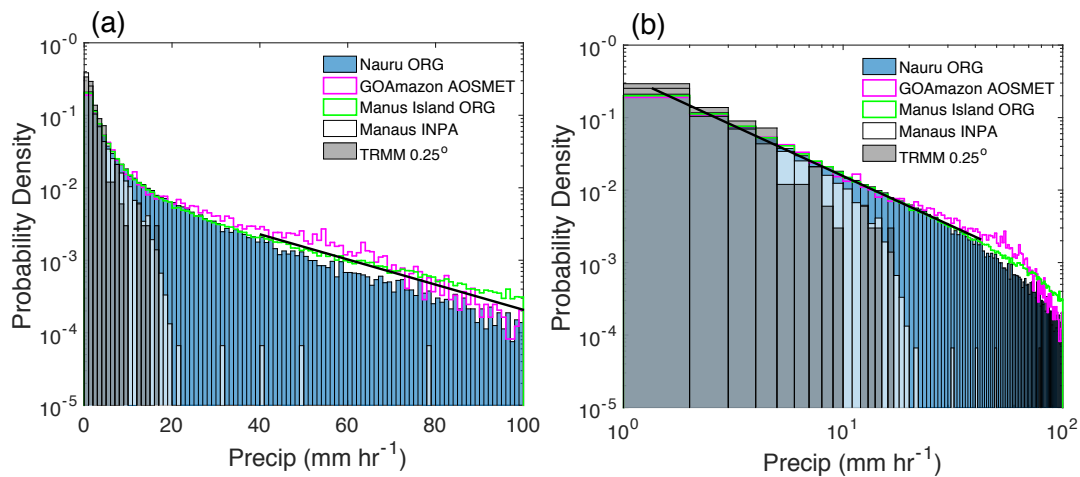
Figure 2.A2: (a) A PDF of precipitating points using 1-min average precipitation for all five instruments used in this study. The means of precipitating points (> 0.1 mm hr^{-1}) are as follows: 7.7 mm hr^{-1} at Nauru, 9.7 at the GOAmazon site, 8.7 mm hr^{-1} at Manus Island, 2.5 mm hr^{-1} at the INPA in Manaus, and 2.2 mm hr^{-1} for the TRMM grid box (0.25^o x 0.25^o) that includes the GOAmazon site. A reference line of slope -0.017 is shown near the exponential part of the curve (from ~40-100 mm hr^{-1}). (b) Same as in (a) but on log-log axes. A reference line corresponding to a power law with slope -1.25 is shown for precipitation rates < 40 mm hr^{-1}.
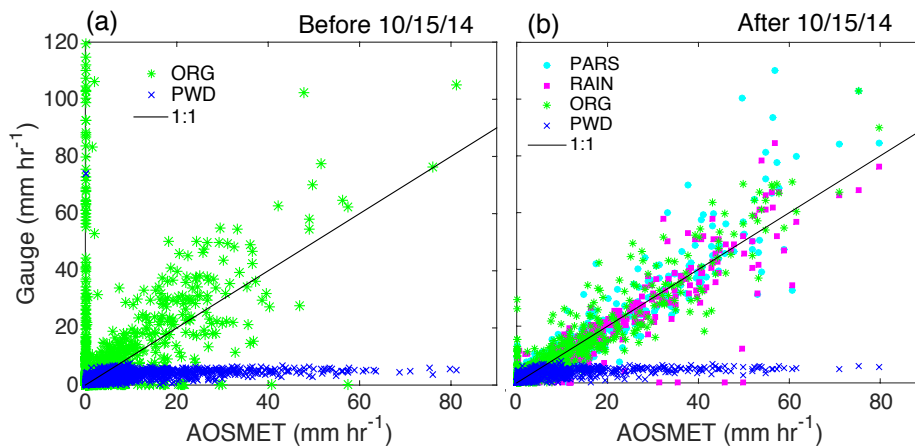
Figure 2.A3: Scatterplots of the precipitation data available from various instruments at the GOAmazon site – optical rain gauge (ORG), present weather detector (PWD), Parisvel laser disdromeder (PARS), tipping bucket rain gauge (RAIN) - in comparison to the AOSMET instrument chosen for this analysis. Results shown are for the time periods (a) prior to 15 Oct 2014 (ORG and PWD only) and (b) after 15 Oct 2014, as a limited selection of reliable observations were available before 15 Oct 2014.

Figure 2.A3 compares the available precipitation observing systems at the GOAmazon site by scattering the 15-minute average precipitation rates of each system against the chosen data set,

AOSMET. Between 01 Jan and 15 Oct 2014, four instruments recorded precipitation: an optical rain gauge (ORG), a present weather detector (PWD), a Vaisala WXT520 from the Aerosol Observing Meteorological Station (AOSMET), and a Vaisala WXT520 from a system including a 3-channel microwave radiometer (MWR3C). Comparison to MWR3C precipitation is not included in this analysis, but the data compare well with the AOSMET precipitation chosen for use in this study (personal communication, ARM Climate Research Facility Data Quality Office).

Figure 2.A3a shows the PWD and ORG datasets scattered against the AOSMET dataset. Two main features are worth noting: (1) the plateau of rain rates in the PWD data (blue), and (2) the erroneous rainfall measured by the ORG (green). The plateau of PWD rain rates indicates that the instrument records a maximum value of ~8-10 mm hr^{-1}; this leads to the systematic recording of erroneously low rain rates above an unknown threshold. These data could be used to confirm the incidence of rain, but analysis of the rain rate magnitudes using these data is not recommended. The ORG had many operational problems throughout the specified time period and thus often recorded precipitation when it was not raining, as is evident from the scatter on the ordinate. Less evident are all of the erroneous values at low rain rates recorded as a result of instrument malfunction. Eliminating all points < 0.5 mm hr^{-1} in the ORG data would likely remedy some issues on the low end, but a threshold would not likely help to eliminate erroneous data on the high end. Therefore, these data must be extensively examined and errors must be corrected for before using these data prior to 15 Oct 2014 when the instrument was repaired (personal communication, ARM Climate Research Facility Data Quality Office).

After 15 Oct 2014, five instruments measured precipitation at the GOAmazon site; all data besides that from the MWR3C system are included in Fig. 2.A3b. It is evident that the ORG data are consistent with the AOSMET precipitation after 15 Oct 2014, as are the data from the Parisvel

laser disdromeder (PARS) and the tipping bucket rain gauge (RAIN). Overall, however, the AOSMET precipitation data set is the most reliable for use throughout the entire GOAmazon campaign, and is thus chosen for use in this analysis. Prior to 15 Oct 2014, use of neither the PWD nor the ORG precipitation data sets is recommended.
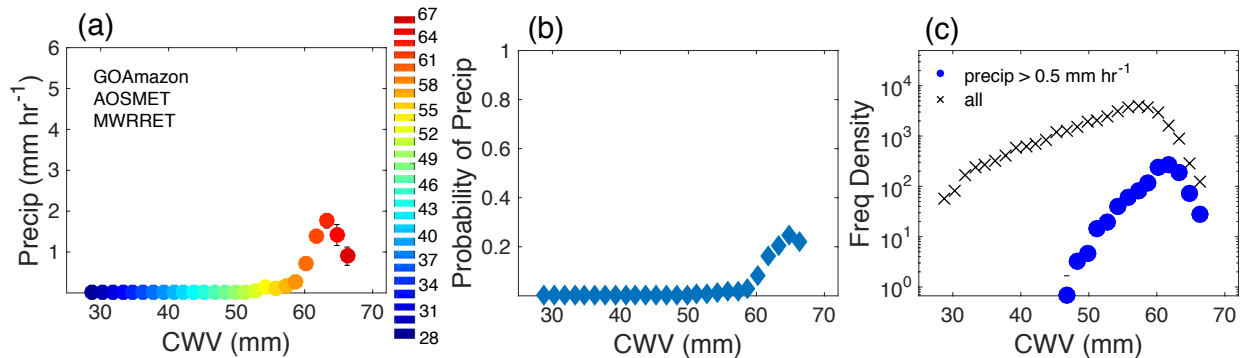
Figure 2.A4: Same as Fig. 1d-f, except with the MWRRET value-added product best-estimate CWV data following the methods of Turner et al. (2007).

As previously noted in Section 2.2, a value-added CWV product from the MWR was archived by the DOE ARM Data Archive in March 2016 and made available in June 2016 (personal communication, ARM Climate Research Facility Data Quality Office). This data set, referred to as MWRRET, is retrieved using a physically-based methodology that includes more information about the atmospheric state in the retrieval process, an optimal estimation in an iterative scheme to retrieve CWV and liquid water path, and a radiative transfer model (Turner et al. 2007).

Even after linearly interpolating over periods of 6 hours or less, the MWRRET contains 60% less data in comparison to the MWR data, and the missing data is likely biased towards periods with substantial precipitation. The length of missing values over which the MWRRET data are linearly interpolated is roughly 10-50% greater than for the MWR data. In the MWRRET CWV dataset, differences in the linear interpolation of CWV values across wet-window periods

(rainy times) tend to shift many of the values previously belonging to high CWV bins to lower CWV bins. The above contributes significantly to the difference in the statistics.

Figure 2.A4 shows a comparison of this data set to the analysis in Fig. 2.1. The results using MWRRET yield identical locations of the precipitation and probability pickups. However, the magnitude of the precipitation and the probability of precipitating points in the last four CWV bins (Figs. 2.A2a, 2.A2b) are reduced compared to Figs. 2.1d and 2.1e. Additionally, the long tails of the CWV distributions for all points and precipitating points at high CWV, seen in Fig. 2.1f, are less pronounced (Fig. 2.A2c) since the occurrence of high CWV is significantly reduced. Overall, this comparison of the less filtered MWR retrieval in the body of the paper to the more conservative MWRRET retrieval in Fig. 2.A4 helps to bound the sensitivity of the statistics to retrieval choices. Regardless of the CWV data retrieval algorithm and method, the key features of the statistics observed in Fig. 2.1 are robust.

In summary, although the qualitative convective transition statistics are robust across a broad set of instrumentation, careful consideration must be given to the observing systems and various data retrieval methods for quantitative aspects, as systematic biases and instrument error could affect comparisons to model output.

CHAPTER 3

Deep Convective Organization, Moisture Vertical Structure, and Convective Transition using Deep-Inflow Plume Buoyancies in the Amazon

Abstract

It is an open question whether an integrated buoyancy measure from a single plume buoyancy formulation can yield a strong relation to precipitation across tropical land and ocean, across seasons and times of day, and for varying degrees of convective organization. An observational basis for such a relation can be beneficial for constraining convective parameterizations, and the consistency of the precipitation-water vapor relation between the DOE Atmospheric Radiation Measurement (ARM) sites in Manacapuru, Brazil and at Nauru in the tropical western Pacific provides one indication that this may be possible. Entraining plume buoyancy calculations confirm that CWV is a good proxy for the conditional instability of the environment, yet differences in convective onset as a function of CWV exist over land and ocean, as well as seasonally and diurnally over land. This is largely due to variability in the contribution of lower tropospheric humidity to the total column moisture. Over land, the relationship between deep convection and lower free tropospheric moisture is robust across all seasons and times of day, whereas the relation to boundary layer moisture is robust for the daytime only. Using S-Band radar, these transition statistics are examined separately for unorganized and organized convection. The latter exhibit sharp pickup curves as a function of lower free tropospheric humidity, consistent with buoyancy-based parameterization. Mixing corresponding to deep inflow of environmental air into a plume that grows with height provides a weighting of boundary layer and free tropospheric air that yields buoyancies consistent with the observed onset of deep convection across seasons

and times of day, across land and ocean sites. Furthermore, it provides relationships that are as strong or stronger for mesoscale-organized convection as for unorganized convection.

3.1   Introduction

Convection is a key process in the hydrologic and energy cycles through the vertical transport of heat, moisture and momentum, and thus largely affects the global energy balance. Representing convection at the right time and place is crucial to the realistic simulation of atmospheric variability. However, the representation of convection remains a large source of uncertainty, bias, and error in current generation numerical weather prediction and climate models (Knight et al. 2007; Sanderson et al. 2008). Errors in simulated precipitation fields often indicate deficiencies in the representation of these physical processes in models. Improving the representation of deep convection thus depends on knowledge of leading-order controls and further requires the development of robust observational constraints from statistical relations that describe these controls.

The uncertainty linked to deep convection lies primarily within a model's representation of complicated interactions across scales and the onset of deep convection. Since most of the present-day global climate models (GCMs) cannot explicitly resolve the small-scale physics of convection, the ensemble effect of convection is represented through parameterization.   The differences among the different convective parameterizations lie primarily in the identification of the source layer of convection and how convective instability is defined and released (Suhas and Zhang 2014). Observational constraints on these processes would provide much-needed insight into the physical basis of these parameterizations. Studies suggest that improvements in the simulation of the Madden-Julian Oscillation (MJO) can be achieved by tweaking the convective closure (Wang and Schlesinger 1999; Zhang and Mu 2005; Lin et al. 2008), and numerical

experiments of the diurnal cycle of precipitation reveal that the parameterization is the main source of error (Betts and Jakob 2002; Bechtold et al. 2004, Knievel et al. 2004; Xie et al. 2004; Lee et al. 2007). Additionally, sensitivity experiments show that certain parameterizations work better for some geographic regions or environments than others, indicating the limitations of parameterizations to consider a range of dynamical and thermodynamic constraints (Liang et al. 2004).

Factors controlling deep convection in the tropics include sensitivity to free tropospheric moisture and entrainment profiles (Brown and Zhang 1997; Holloway and Neelin 2009), the diurnal cycle (Betts and Jakob 2002; Chaboureau et al. 2004; Del Genio and Wu 2010; Zhang and Klein 2010), large-scale dynamics forcing vertical ascent (Kumar et al. 2013; Hohenegger and Stevens 2013), vertical wind shear (Rotunno et al. 1988), microphysical processes and aerosols (Andreae et al. 2004; Rosenfeld et al. 2008), and lifting at the leading edge of cold pools (Tompkins 2001; Khairoutdinov and Randall 2006; Schlemmer and Hohenegger 2014). Examining the transition to deep convection in varying spatial domains and in time (Holloway and Neelin 2010; Adams et al. 2013) is also critical to our understanding. Despite additional complexities, it is of interest to examine whether a bulk measure of buoyancy computed from a simple plume model can yield a consistent relation with observed deep convection over a range of conditions, including larger mesoscale convective systems (MCSs). Ideally, a parameterization would yield realistic statistics for such processes across regions, seasons, times of day, and even for varying levels of convective organization.

Several factors contribute to deep convective onset and associated uncertainty in GCMs, yet one of the most significant is thought to be the entrainment profile. Sensitivity studies with climate models have demonstrated that the mixing processes in cumulus convection are among the

most sensitive of parameters (Murphy et al. 2004; Klocke et al. 2011; Bernstein and Neelin 2017). Sahany et al. 2012 showed that differing the entrainment profiles in CAM3.5 had a substantial impact on the convective onset as defined by the entraining CAPE. Additionally, Kuo et al. 2017 found that without entrainment, the sharp increase in precipitation with CWV observed over both land (Schiro et al. 2016; Ahmed and Schumacher 2016) and ocean (Bretherton et al. 2004; Peters and Neelin 2006; Holloway and Neelin 2009; Neelin et al. 2009; Ahmed and Schumacher 2015) disappears. However, detailed representation of cumulus mixing remains highly uncertain due partly to the lack of observational constraints (e.g. Mapes and Neale 2011).

By modifying the entrainment profile, the relative roles of boundary layer humidity and free-tropospheric humidity can significantly change, which motivates our discussion here about the appropriate weighting of free tropospheric and boundary layer air and the interaction between convection and the moisture field. It is of interest to find a mixing scheme that is most appropriate to span a range of conditions in varying convective environments. Holloway and Neelin (2009) explored the consistency of various mixing assumptions to the observed onset of precipitation as a function of CWV and introduced a mixing scheme associated with deep inflow into the plume through a deep lower tropospheric layer. The concept of deep inflow into a plume is agnostic regarding the extent to which the environmental air enters via small-scale turbulence versus organized inflow. It is thus plausible that it may span a range of convection types and is reasonable to test for consistency with the way organized convective system interact with their environments. This is explored here using radar data to distinguish local, isolated convection from organized convection.

Here, we extend beyond the CWV-precipitation relation to examine the moisture vertical structure, its associated variability (e.g. regionally, diurnally, seasonally), its effects on the

conditional instability of the environment and thus the onset of deep convection, and its relation to convective organization. The convective environments in and around Manaus, Brazil, as intensively observed during the two-year (2014-2015) Green Ocean Amazon, or GOAmazon, campaign will be of primary focus, but we will draw parallels where appropriate to the convective environment in the tropical western Pacific using data from the DOE Atmospheric Radiation Measurement (ARM) site at Nauru. The relationship between boundary layer and free tropospheric moisture to convective onset will be quantified, and plume buoyancies, computed with various mixing assumptions, will be related to the observed onset of deep convection across regions, seasons, and times of day, and for varying degrees of convective organization.

3.2 Data

3.2.1 *Precipitation*

The in situ precipitation measurements analyzed from the GOAmazon site are from the Aerosol Observing System and measured by the acoustic gauge of a Vaisala WXT520 meteorological station; these data are thus referred to as AOSMET precipitation. When related to radiosonde CWV, AOSMET precipitation is averaged at 2-hr intervals centered 1 hour after radiosonde launch; for analyses with radiometer CWV, AOSMET precipitation is averaged at 12-min intervals. Precipitation probability is computed with respect to a threshold of 0.5 mm hr^{-1}.

Radar derived precipitation rates are also incorporated. These data were obtained from the Sistema de Proteção da Amazonia (SIPAM) ground-based S-Band (10 cm wavelength), Doppler, single-polarized radar, with a horizontal beam width of 0.96^o and a vertical beam width of 0.93^o. The radar scans up to 17 elevation angles from 0.9^o to 19° every 12 min. The reflectivity data are interpolated to the Constant Altitude Plan Position Indicator (CAPPI) data with horizontal resolution of 2 km and vertical resolution of 0.5 km (altitude ranges from 0.5 to 20 km). A single

reflectivity-precipitation (Z-R) relation (Z=174.8R$^{1.56}$), created using 2014 wet-season impact disdrometer data, was applied by ARM to the 2.5 km SIPAM Manaus S-Band CAPPI data to generate rain rates for each radar volume. These data are then spatially averaged in 25 km and 100 km grid boxes surrounding the GOAmazon site (T3), to provide statistics comparable to that of typical GCM grid scales. The 100 km grid box was shifted slightly right of center from the T3 site, as data is not recommended for use for rain rate retrievals beyond a 110 km radius of the radar (see Giangrande et al. 2016, Fig. 1).

3.2.2 *Moisture*

The data used in this study are taken from two DOE ARM sites in the tropics. The first is the DOE ARM Mobile Facility deployed as part of the GOAmazon field campaign (January 2014–December 2015). All observations in this study were measured at the T3 site (3.21^{o}S, 60.60^{o}W, 50-m altitude) near Manacapuru, except for data from an S-Band radar at site T1 (3.15^{o}S, 59.99^{o}W) to the east of T3. The results from the GOAmazon site are compared to 5 years of data (2001-2006) from a retired DOE ARM site in the tropical western Pacific at Nauru (0° 31'S, 166° 54'E; 7-m altitude).

Thermodynamic profiles and CWV data from the radiosondes were obtained from 4-5 times daily launches (01:30, 07:30, 10:30 – wet season only, 13:30 and 19:30 LT) at the GOAmazon site from Vaisala Digi-Cora III sounding systems at 2-s resolution. The raw sounding data were interpolated to 5-mb intervals (1 mb = 1 hPa) for mixing computations in Section 2.5. The reported uncertainties are ~5% for relative humidity and ~0.5^{o}C for temperature below 500 mb. It is worth noting that, because of sampling, averages including all available data in this analysis will be more representative of the nighttime soundings than the daytime soundings. At Nauru, launches occurred twice daily (00:00 and 12:00 LT). We remove any radiosondes from the

analysis if rain occurred 4 hours prior to launch to avoid, as best as possible, sampling within a cold pool and an environment modified by precipitation processes.

Microwave radiometer CWV from the GOAmazon site using the MWRRET value-added product (Turner et al. 2007) is employed in Section 2.4.1. A linear interpolation procedure is performed to gap-fill CWV values across time periods of 6 hours or less. Interpolation is reasonable given that the data gaps are typically short and the temporal persistence of water vapor values for strong convective events is on the order of hours (Holloway and Neelin 2010), although quantitative differences can be noted between different methods of filtering and interpolation. Figure 3.S1 quantifies these differences by comparing different interpolation methods and datasets, including those used in Schiro et al. (2016). The linear interpolation procedure likely underestimates peak CWV, but is chosen as the more conservative method. The data used in this study are averaged at 12-min intervals to match the 12-min resolution of the Doppler radar.

3.2.3 *Cloud top height*

Cloud top height provides an additional measure of deep convection to the convective onset statistics presented in Section 3.4. These data are obtained from a product provided through the DOE ARM program that uses the 95 GHz W-Band ARM Cloud Radar (WACR), micropulse lidar, and ceilometer data to produce cloud boundaries using the WACR Active Remote Sensing of Clouds (WACR-ARSCL) Value-Added Product (Kollias and Miller, 2007). Cloud top heights are averaged at 1-hour intervals, and cloud tops with bases greater than 3 km are excluded from the analysis.

3.2.4 *Convection Classification*

Information about convection type is obtained from composite S-Band radar reflectivity in a 100 km grid box surrounding the GOAmazon site. Classifying deep convection and organized

convection using radar data typically involves employing a maximum reflectivity threshold in base reflectivity (e.g. Churchill and Houze 1984; Steiner et al. 1995). If this threshold exceeds 40 dBz, it is typically convective, as stratiform precipitation usually does not have such high base reflectivity. Here, we employ a threshold of 45 dBz to distinguish convective from stratiform processes since we use composite reflectivity instead of base reflectivity. Events are grouped into four categories. Deep organized convection ("DEEP-org") is classified as having maximum reflectivity greater than or equal to 45 dBz and a spatial extent greater than 50 km in one direction. Spatial extent is defined by contiguous pixels with reflectivity greater than 30 dBz. A 50 km threshold is employed here, rather than a more traditional 100 km threshold to identify mesoscale convective systems (MCSs; Houze 2004), as a reasonable separation in order to include as many convective events as possible. Deep cellular convection ("DEEP-cell") are locally-occurring, isolated cells with reflectivity greater than 45 dBz and a spatial extent less than 50 km in one direction. Examples of DEEP-org and DEEP-cell events are shown in Fig. 3S.1. Other precipitation ("other") is defined by maximum reflectivity less than 45 dBz for any spatial extent. Lastly, no precipitation ("no precip") is defined by maximum reflectivity less than 20 dBz throughout the 100 km domain.

3.3   Moisture Vertical Structure

A robust relationship exists between CWV and precipitation over tropical oceans (Bretherton et al. 2004; Peters and Neelin 2006; Neelin et al. 2009; Holloway and Neelin 2009; Ahmed and Schumacher 2015), which also holds over tropical land (Schiro et al. 2016; Ahmed and Schumacher 2016). In this study, we go beyond this relation by characterizing the effects of variability in moisture vertical structure regionally, seasonally, and diurnally on convective onset,

with the aim of better understanding the mechanisms through which the moisture field interacts with the convection through effects on conditional instability.
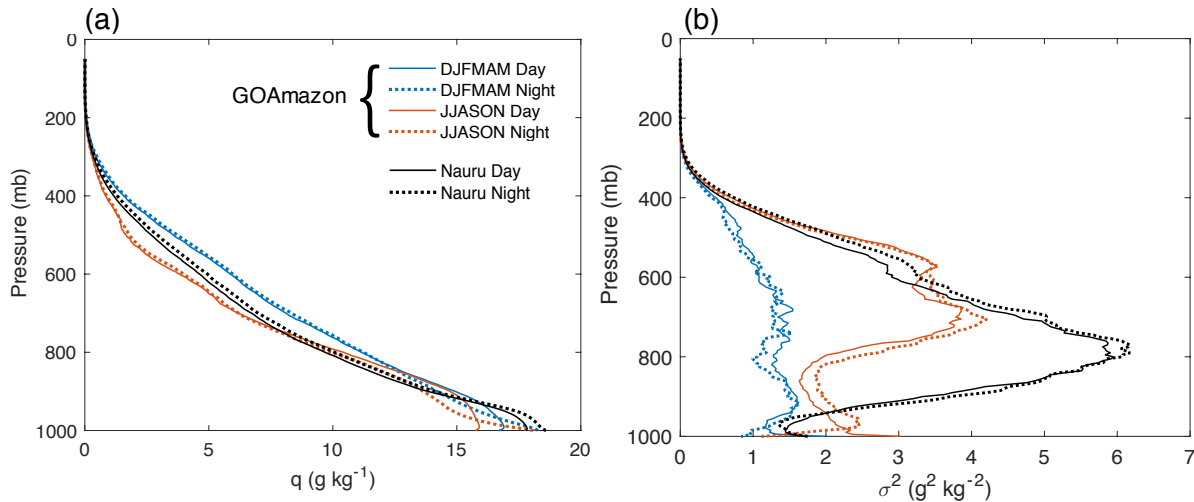
Figure 3.1: (a) Mean specific humidity profiles at the GOAmazon site by time of day (nighttime – 01:30, 07:30 and 19:30 LT; daytime – 10:30, 13:30 LT) and season (wetter months, DJFMAM, in blue; drier months, JJASON, in orange). (b) As in (a), but for specific humidity variance.

Fig. 3.1 shows the mean moisture structure (Fig. 3.1a) and moisture variance profiles (Fig. 3.1b) throughout the troposphere for Nauru in the tropical western Pacific (black curve; see also Holloway and Neelin 2009) and the GOAmazon site (color). The results shown at Nauru span the entire seasonal cycle, as there is little variability seasonally. There is also little variability in moisture diurnally, but we show this for reference. At the GOAmazon site, we define seasons based on the two main patterns observed in moisture variance, seen in Fig. 3.1b. This definition varies from those traditionally used in the literature defining wet, dry, and transition seasons in the Amazon (e.g. Machado et al. 2004). Since we are specifically examining variability in moisture vertical structure and its effects on conditional instability of the environment and the onset of deep convection, we feel justified in our definitions based on moisture variance only. This also aids in developing robust statistics, given the limited sampling of the radiosondes. Thus, we are left with

49

two seasons consisting of 6 months each – the wetter half of the year (Dec-May, DJFMAM) and the drier half (Jun-Nov, JJASON) – that will be compared throughout the study.
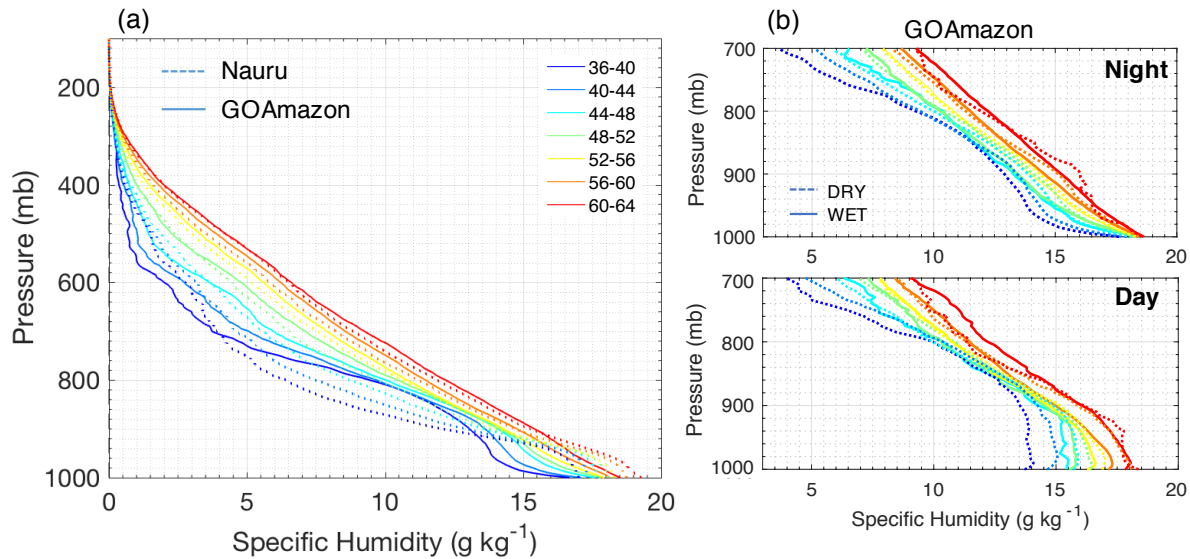
Figure 3.2: (a) Specific humidity profiles conditionally averaged by CWV (colors) for Nauru (dashed) and GOAmazon (solid). Averages are for profiles during all times of day and all seasons. (b) For GOAmazon profiles only, zoomed in on the lower troposphere (700-1000 mb) and split out by season (wetter months, solid; drier months, dashed) and time of day (night, top panel; day, bottom panel).

During the wetter months (JFMAM), the atmosphere is moist throughout the entire troposphere and is less variable than the dry season, wherein the humidity in the boundary layer and middle troposphere is more variable. Diurnal variability also exists in the vertical moisture structure, most notably in the near-surface layer but also in the lower free troposphere. Compared to Nauru, along the eastern margin of the warm pool in the tropical western Pacific, the boundary layer at the GOAmazon site is less moist, but the lower free troposphere is moister. Moisture variance is notably greater at Nauru, particularly in the lower free troposphere, than it is at the GOAmazon site.

Fig. 3.2a shows the profiles of specific humidity conditionally averaged by CWV for Nauru (dashed), as shown in Fig. 3a of Holloway and Neelin (2009), over top of the results for

GOAmazon (solid). The results in Fig. 3.2a are averaged for all times of day and all seasons. For the same CWV values, the boundary layer humidity is higher at Nauru than at GOAmazon, and the lower free troposphere (~750-900 mb) is moister at GOAmazon than at Nauru, especially at lower CWV. Above 700 mb, the GOAmazon site still has higher humidity on average, but the profiles are more consistent across CWV. To summarize, the contribution to total CWV from the boundary layer at Nauru is larger, and thus the moisture content aloft is, on average, lesser at Nauru than it is at the GOAmazon site for the same CWV. Thus, there are different moisture profiles with the same total column humidity over land and ocean, which likely contribute to differences observed in the onset of deep convection as a function of CWV over land and ocean. For instance, the onset of deep convection occurs at lower CWV over land and ocean (Schiro et al. 2016; Ahmed and Schumacher 2017). This will be explored further in Section 3.5 where we examine the effects of moisture on conditional instability with simple plume models.

To examine the diurnal cycle and its relation to the moisture vertical structure in greater detail with respect to CWV at the GOAmazon site, we conditionally average the specific humidity profiles on CWV for daytime and nighttime soundings for DJFMAM (solid) and JJASON (dashed) and zoom in on the structure in the lower troposphere (700-1000 mb) in Fig. 3.2b. Overall, the boundary layer in the daytime is deeper (on the order of 1 km), more variable, and spans a broader range of specific humidity values with CWV than in the nighttime boundary layer, which is much shallower (on the order of a few hundred meters), less variable, and spans a narrower range of humidity values with CWV. In the drier months, the boundary layer contributes more to the total column moisture than in the wetter months. In the drier months during the day, total column moisture is characterized by a narrower range of humidity values in the lower free troposphere than in the wetter months. Alternatively, above 700 mb, total column moisture is characterized by

51

a broader range of humidity values in the drier months than the wetter months for both daytime and nighttime soundings (not shown). For reference, Fig. 3.S2 in the supplement shows the correlation of CWV with specific humidity as a function of height broken out by time-of-day and season.

Overall, the moisture profiles that characterize the total column moisture can vary seasonally, diurnally, and regionally. The implications of this will be explored in greater detail in Section 3.5, as we examine the relation between the moisture vertical structure and the conditional instability of the environment with entraining plume buoyancies.

3.4   Convective Onset Statistics

3.4.1   *Relationship to Seasonal and Diurnal Cycles*

The onset of deep convection, as shown by precipitation and cloud top height as a function of CWV, is shown in Fig. 3.3 for DJFMAM Day, DJFMAM Night, JJASON Day, and JJASON Night. The statistics are shown for both in situ precipitation and precipitation from the S-Band radar, as well as for CWV from both the microwave radiometer and radiosondes. Cloud top heights are derived from the W-Band cloud radar (x's). All cloud tops with bases greater than 3 km are excluded from the statistics. It is evident that the conditional mean rain rate and cloud top height, as well as the probability of precipitation exceeding 0.5 mm hr^{-1} and cloud top height exceeding 8 km, sharply increase with CWV across the diurnal and seasonal cycles.

During the daytime, precipitation is frequent, which is evident in the PDFs of precipitating points (colors) in comparison to the total points (black/gray squares). On average, the onset is observed at slightly lower CWV in the daytime than at night, and at higher CWV in the wetter months than in the drier months. Additionally, in the drier months, the range of CWV observed is
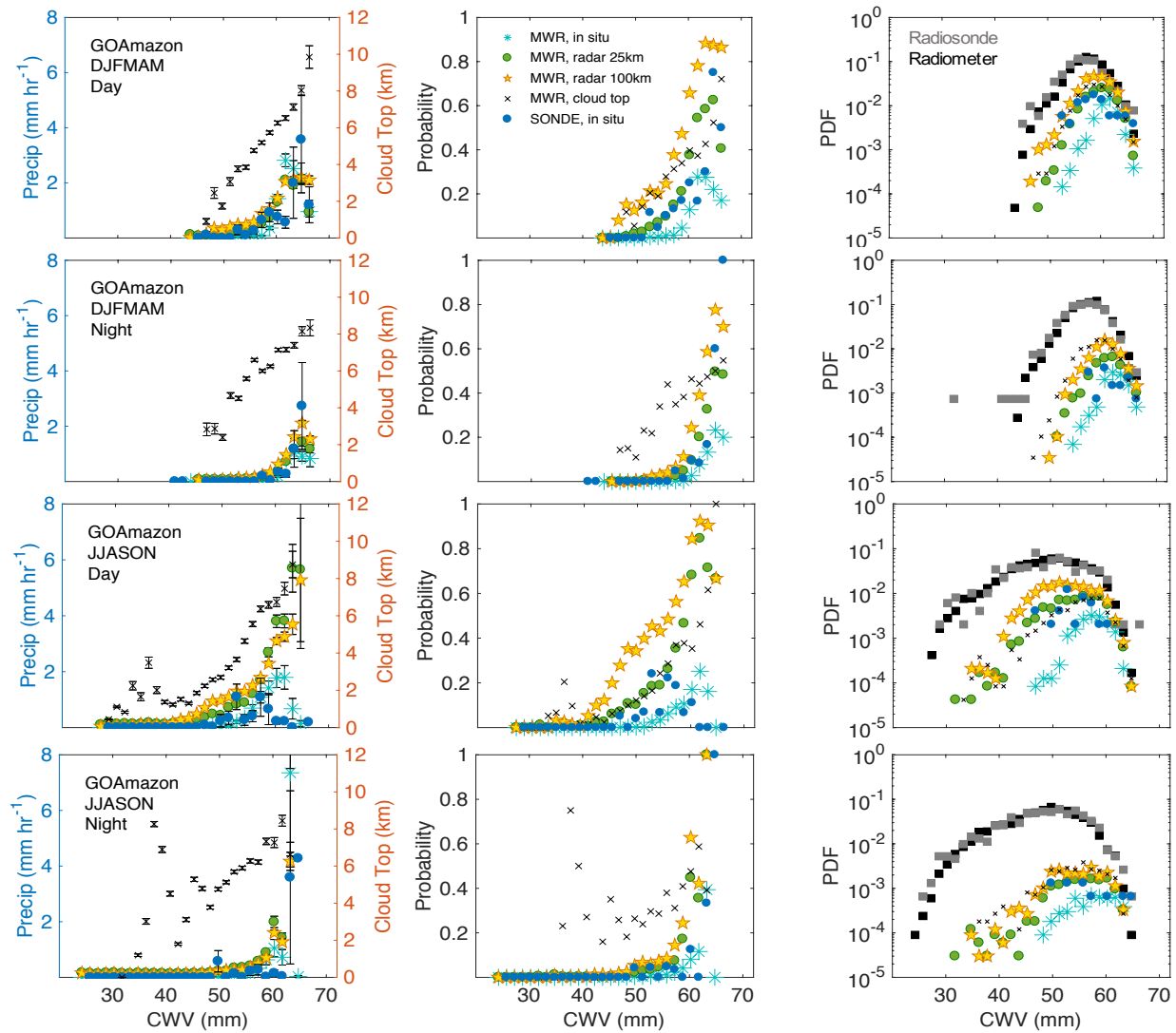
Figure 3.3: Convective onset statistics at the GOAmazon site for DJFMAM Day (top row), DJFMAM Night (second row), JJASON Day (third row), and JJASON Night (bottom row) for 12-min average microwave radiometer CWV and in situ precipitation (blue stars), radar precipitation at 25 km (green circles), radar precipitation at 100 km (yellow stars), and W-Band Cloud Radar derived cloud top height (x's), as well as radiosonde-derived CWV with 1-hr average in situ precipitation (blue circles). Left column: precipitation conditionally averaged on CWV. Middle column: probability of precipitation greater than 0.5 mm hr^{-1} in each CWV bin. Right column: probability density of radiometer (black squares) and radiosonde (gray squares) CWV, and of precipitating points (colors).

wider than that observed during the wetter months. In the daytime, the lower tropospheric moisture is higher than in the nighttime for the same CWV value and for the dry season in comparison to the wet season (Fig. 3.2). This result suggests that differences in lower tropospheric moisture content, rather than total column moisture, are most important to the onset of deep convection,

thus contributing to the differences observed in the onset with respect to CWV regionally, seasonally, and diurnally. In Section 3.4.3, we divide the lower troposphere into contributions from the boundary layer and free troposphere to examine their respective influences.

It is worth noting that these characteristics defining the onset are consistent across all observational platforms, yet the sampling limitation of the radiosonde and in situ-derived statistics in comparison to the radiometer and radar derived statistics is apparent. Throughout the remainder of the study, we use radiosonde-derived thermodynamic quantities in relation to in situ and radar precipitation, since we wish to examine the vertical moisture structure within the context of the conditional instability of the environment. This, however, provides some context for the robustness of the statistics when the sample size is increased.

3.4.2 *Convective Organization*

To examine the onset as it relates to convective organization, radar data are employed to characterize the level of organization of the convection within a 100 km grid box surrounding the GOAmazon site within an hour of radiosonde launches. As described in Section 3.2.4, convection is classified as deep if the composite radar reflectivity exceeds 45 dBz. The convection is considered organized when it exceeds 50 km in one linear dimension (contiguous reflectivity > 30 dBz), and is considered cellular for anything less than 50 km. This information is displayed in a histogram in the left column of Fig. 3.4, with the probability of precipitation (precipitation rates greater than 0.5 mm hr^{-1}) as a function of radiosonde-derived CWV overlain. Moving forward, all radiosondes launched after precipitation events up to 4 hours prior are eliminated from this analysis to reduce the likelihood of sampling air directly modified by precipitation processes. For the probability, only bins including 5 or more samples are plotted.
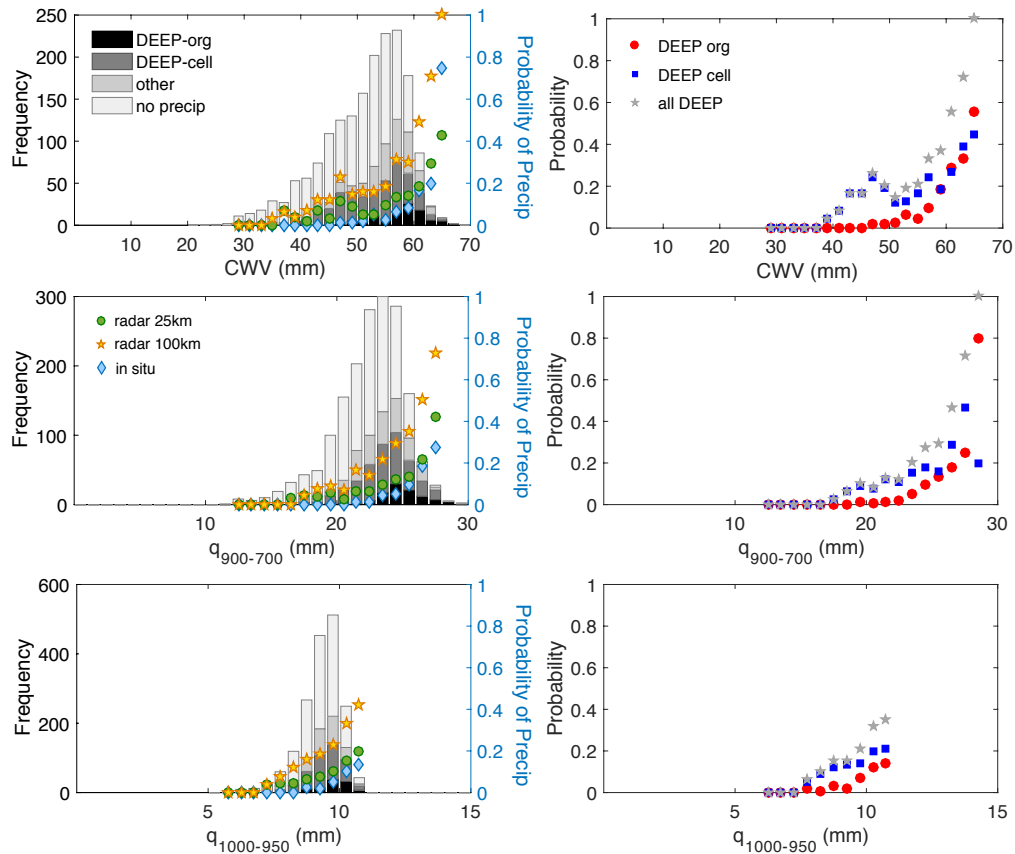
Figure 3.4: (left column) Histograms of convection type as classified using radar reflectivity and precipitation area within a 100 km grid box surrounding the GOAmazon site (black – organized deep convection ≥ 45 dbz and at least 50 km wide in one direction; dark grey – cellular deep convection ≥ 45 dbz and < 50 km wide in one direction; light gray – other precipitation with reflectivity < 45 dbz; white - no reflectivity signature > 20 dbz detected in the domain) and probability of precipitation greater than 0.5 mm hr^{-1} from in situ rain gauge measurements (blue diamonds), radar precipitation from a 25 km spatial average around the GOAmazon site (green circles), and radar precipitation from a 100 km spatial average around the GOAmazon site (yellow star) conditionally averaged by integrated humidity in (a) the total column from 200-1000 mb, (b) the lower free troposphere (700-900 mb), and (c) the boundary layer (950-1000 mb). (right column) The fraction of the total observations that were deep convection (grey stars), cellular deep convection only (blue squares) and organized deep convection (red circles) with rain rates greater than 0.5 mm hr^{-1}.

The information in Fig. 3.4 (top row) is complementary to that presented in Fig. 3.3: the

probability of precipitation is the same except for being matched to radiosonde CWV and using 1-

hr averages instead of 12-min averages, and the histogram presented is a more detailed look at the

convective type contributing to the distribution of precipitating points. The right column examines

the fraction of the total observations that were classified as deep convection (all deep convection

– grey stars; organized deep convection – red circles; cellular deep convection – blue squares).

The grey stars share a symbol with the yellow stars in the left panel to signify their similarity, as the black stars are derived from the classification at 100 km and the yellow stars are derived from the mean reflectivity in the 100 km domain.

The onset of deep convection occurs with increasing total moisture in the column. The average probability of precipitation is greater at 100 km than at 25 km and in situ because the likelihood of observing precipitation increases as the size of the grid cell increases. Isolated cells are the most common deep convection type, with organized deep convection a larger fraction of the total at high CWV. A key finding is that organized convection and local, isolated cells are both sensitive to the humidity in the atmosphere, and the occurrence of both convective types sharply increases with increasing CWV. Isolated cellular convection is, however, observed at CWV in the 40-50 mm range, whereas organized convection is rarely observed in this range. This will be explored further in Section 3.4.3.

3.4.3 *Boundary Layer vs. Free Troposphere*

We now examine the respective relationships of boundary layer and free tropospheric humidity to deep convection and convective organization. Much of the relation between deep convection and CWV can be explained by its relation to free tropospheric moisture (middle row, Fig. 3.4). Some of the relation can also be explained by boundary layer humidity (bottom row, Fig. 3.4), although this relationship is less pronounced on average. (For information about the sensitivity of these results to layer averaging, see Fig. 3.S4 and corresponding discussion in the supplement.) It should be noted, however, that the averages over all times of day are more representative of nocturnal convection, as radiosondes are more frequently launched at these times.

Fig. 3.5 is the same as Fig. 3.4 for the free troposphere, but separates out the analysis by time-of-day and season. The probabilities of precipitation for in situ, 25 km radar, and 100 km
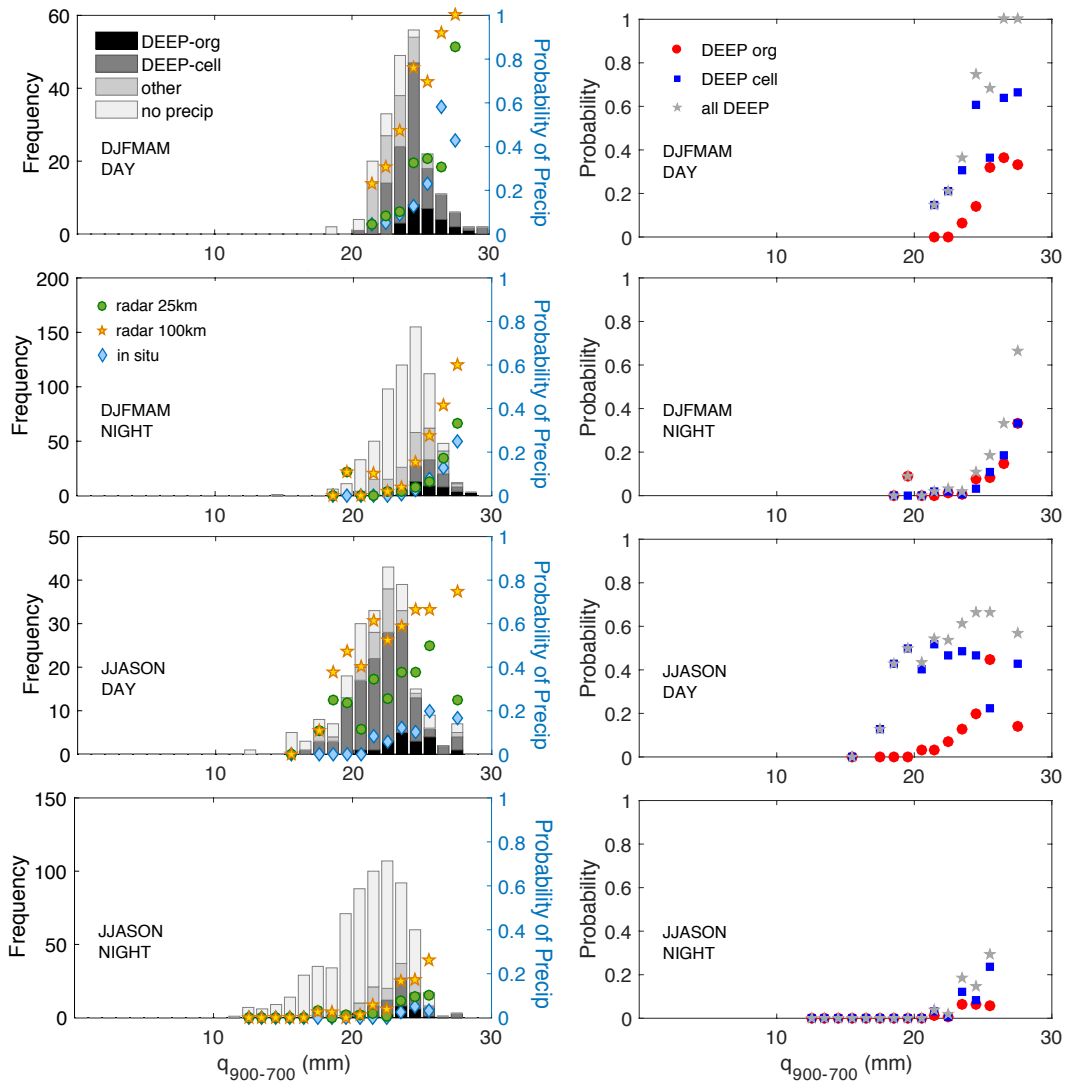
Figure 3.5: Same as Fig. 3.4, except for integrated humidity in the free troposphere (700-900 mb) only during (a) DJFMAM Day, (b) DJFMAM Night, (c) JJASON Day, and (d) JJASON Night.

radar precipitation all increase sharply with increasing lower free tropospheric humidity for all seasons and times of day; the one exception is the dry season nighttime, whose probabilities are lower. It appears for this case that high humidity in the lower free troposphere does not guarantee convection, but when convection is observed it occurs in humid environments only. Additionally, the probability of both cellular and organized deep convection increases sharply with increasing humidity in the wet season, but the dry season daytime shows moderately high probability of
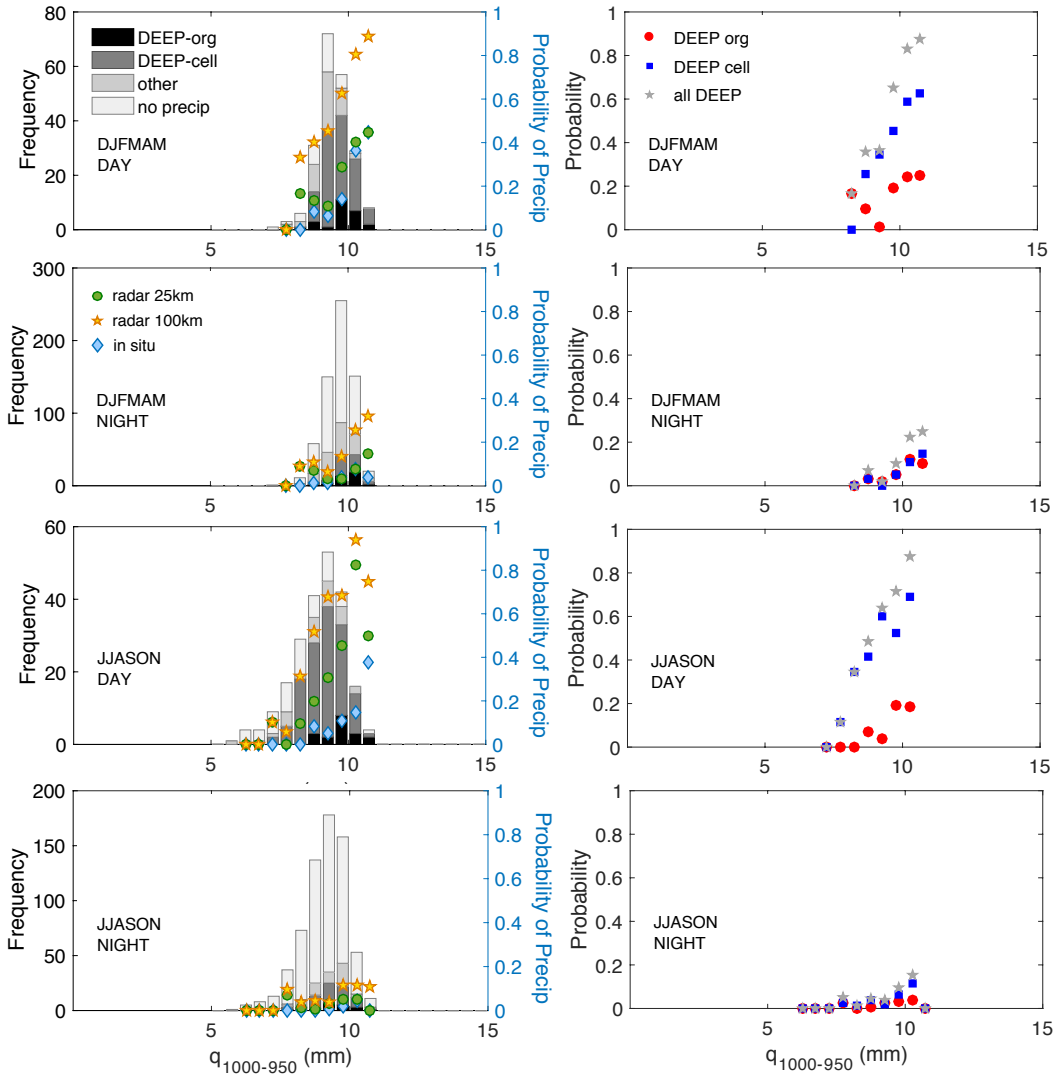
Figure 3.6: Same as Fig. 3.5, except for integrated humidity in the boundary layer (950-1000 mb) during (a) DJFMAM Day, (b) DJFMAM Night, (c) JJASON Day, and (d) JJASON Night.

isolated cellular convection even for lower humidity. Cellular deep convection is ubiquitous throughout the domain during the daytime hours in all seasons and is the most frequent type of deep convection observed. At night, however, the probabilities of both convection types are equally likely and increase sharply with increasing lower free tropospheric humidity. Overall, the occurrence of both cellular and organized convection is strongly tied to the lower free tropospheric humidity, with occurrence of cellular convection at lower humidity in the daytime hours (particularly the dry season).

The role of the boundary layer is depicted in Fig. 3.6, where the probability of precipitation and frequency of deep convective events show strong relation to the boundary layer humidity (1000-950 mb) during the daytime. At night, this relationship is less discernable. The nocturnal boundary layer, often shallower than 950 mb, is much less variable than the daytime boundary layer and maintains high humidity at nearly constant values. A layer of convective inhibition develops, and in some instances, is possibly a hindrance to the development of convection without the presence of mechanical lifting or erosion by solar heating in the morning hours. Cellular convection increase sharply with increasing humidity during the daytime, while organized convection does not appear to be as tied to the boundary layer humidity. Both the probabilities of precipitation in the left column and the probability of deep convection (right column) show that the relation to the boundary layer is much weaker during the nighttime than daytime.

Overall, deep convection of all types, in all seasons, and at all times of day occurs more frequently with increasing lower free tropospheric humidity. The lower free tropospheric humidity is strongly tied to the occurrence of organized deep convection. The boundary layer is also strongly related to convective onset, but this is mainly true for the daytime and cellular convection only. For reference, variants of these statistics for the boundary layer and lower free troposphere are reproduced in the supplemental material (Figs. 3.S5 and 3.S6) as a function of their respective layer saturation.

3.5   Relating observed deep convection to plume buoyancy under different mixing parameterizations

In Section 3.4, we examine the relation between deep convection and moisture and how variability in moisture vertical structure (e.g. seasonally, diurnally) contributes to variability in deep convective onset as a function of total column moisture. It was also shown that both organized

and unorganized convection show strong relation to lower tropospheric moisture, particularly in the free troposphere. CWV has proven useful in previous studies since it is commonly available from GCM output and satellite retrievals (over ocean), and since it is a good proxy for conditional instability over land and ocean (Holloway and Neelin 2009; Schiro et al. 2016). Here, since we have additional data available – vertical moisture structure, information about diurnal variability and convection type – we have the opportunity to test various assumptions of plume buoyancy against observed deep convection across a range of conditions. Thus, in Section 3.5, we refine our analysis by replacing CWV by measures explicitly based on the conditional instability of the environment, using different postulates for mixing as it affects plume buoyancy.

GCMs all make assumptions about buoyancy that, in combination with other parts of the deep convective closure scheme, yield precipitation. We thus ask how strong a relation to observed deep convection can be achieved with a single, physically-consistent plume buoyancy formulation. Ideally, a bulk measure of plume buoyancy given a realistic, physically-based assumption would show strong relation to observed precipitation and deep convection over a wide range of environmental conditions. Our exploration of thermodynamic controls in the previous section suggested that the consistent relation to lower tropospheric moisture, particularly in the lower free troposphere, provides some indication that buoyancy is largely dependent on the moisture available in this layer, and that a model of plume buoyancy that adequately accounts for variability in this quantity could yield consistent results under a range of environmental conditions (e.g. across seasons, diurnal cycle, regions, and even for different convection types).

3.5.1 *Formulation*

All mixing assumptions discussed here follow the general form $r_k = (1 - \chi_{k-1}\Delta p)_{r-k} + \chi_{k-1}\Delta p\tilde{r}_{k-1}$, where r is the conserved variable, $\tilde{r}$ is the corresponding environmental variable, k

is the pressure level, Δp is the pressure interval, and χ is the mixing coefficient. For all mixing assumptions that include freezing, liquid water is converted to ice conserving the ice-liquid water potential temperature when the plume reaches 0°C. All computations are performed in pressure coordinates. For reference, a case with no mixing is also shown, in which a parcel is raised undiluted from 1000 mb.

The constant-mixing case assumes that the plume mixes with the environmental air at a constant rate of 0.001 hPa^{-1} between 50 and 950 mb with a larger rate of χ (0.18 hPa^{-1}) in the boundary layer (1000-950 mb). This is the same assumption used in Holloway and Neelin (2009), and is similar to the assumption from Brown and Zhang (1997). It has been noted previously in the literature the limitations of such an assumption, either in the magnitude of the coefficient used (Kuang and Bretherton 2006) or in the range of values needed to yield consistency to observed deep convection (Jensen and Del Genio 2006). Here, we expand upon these arguments by examining its consistency to observed deep convection over a tropical land site.

Deep-Inflow mixing, first introduced by Holloway and Neelin (2009) but reviewed here, follows the assumption that the updraft mass flux increases nearly linearly through a deep lower tropospheric layer, consistent with observations of vertical velocity and derived mass flux profiles over tropical ocean (e.g. Robe and Emanuel 1996; LeMone and Zipser 1980) and tropical land (May and Rajopadhyaya 1999; Kumar et al. 2015; Giangrande et al. 2016). Deep inflow refers to a plume's interaction with its environment by way of lateral inflow of environmental air through a deep lower tropospheric layer and is relatively agnostic to the mechanism through which the air becomes incorporated into the plume (e.g. it could occur partly through organized inflow at the plume-scale or mesoscale in addition to small-scale turbulence). It is thus reasonable to conjecture

that this scheme might apply to the mesoscale-organized convection identified in the analysis above, in addition to unorganized plumes.

If detrainment is neglected, an entrainment profile can be calculated for any corresponding mass flux profile from mass continuity. We can derive mixing coefficients using $\chi_k = -m^{-1}(\partial m/\partial p)\Delta p$, where m is the mass flux and p is pressure, with Δp defined to be positive. If mass flux increases with height throughout the lower troposphere, this would suggest large lower tropospheric entrainment rates. The weighting of the environmental variable is given by the vertical rate of increase of mass as follows:

$$r(p) = \frac{1}{m(p)} \int_{p_0}^{p} \tilde{r} \, \frac{\partial m}{dp} \, dp$$

If the plume's mass is increasing linearly with height, this reduces to a vertical average of all levels:

$$r(p) = (p - p_0)^{-1} \int_{p_0}^{p} \tilde{r} \, dp$$

Deep-Inflow-A (Holloway and Neelin 2009; Sahany et al. 2012) is given from an LES-based estimate of the vertical dependence of the mixing coefficient reported in Siebesma et al. (2007), where the mixing coefficient has an inverse dependence on height following $\chi_k \Delta p = c_\in z_k^{-1} \Delta z_k$, where $c_\in = 0.4$, z is the height, and Δz_k is the depth of the layer. Deep-Inflow-B uses an idealized updraft vertical velocity which increases nearly linearly with height with 0 at 1000 hPa and its maximum at 430 hPa. The mixing coefficients are then computed from the vertical gradient of the specified updraft vertical velocity profile, with the mixing coefficient set to zero above 430 hPa (under the postulate that there is negligible mixing above the level where mass flux no longer increases).

Figure 3.7: Mean virtual temperature differences between plumes originating at 1000 mb and their surrounding environments conditionally averaged by CWV for (a) no mixing, (b) constant mixing (0.001 hPa^{-1}), (c) Deep-Inflow-A mixing, and (d) Deep-Inflow-B mixing for Nauru (dashed) and GOAmazon (solid).

3.5.2 *Profiles*

Fig. 3.7 compares buoyancy profiles between the GOAmazon site and Nauru for the range of mixing assumptions described above and examines their consistency to the onset of deep convection observed with increasing humidity. All profiles are virtual temperature profiles derived from the radiosondes. Environmental profiles are subtracted from the plume computations, which originate at 1000 mb (near-surface). Profiles in Fig. 3.7 are averaged for all times of day and all seasons. It is worth noting again that, unless separated by time-of-day, the analysis at the

GOAmazon site will be more representative of the nighttime soundings than the daytime soundings due to a higher frequency of nighttime soundings.

Fig. 3.7a is the simplest case, which assumes no mixing with the surrounding environment, and thus the buoyancies are largely dependent on the characteristics of the plume at its level of origin. This yields results inconsistent with the onset of precipitation at a critical value of CWV (e.g., Fig. 4; see also Fig. 3a, Holloway and Neelin 2009; Fig. 2a, Schiro et al. 2016) over both land and ocean, since buoyancies are positive through the free troposphere for all CWV at Nauru and GOAmazon (above a layer of convective inhibition in the nighttime hours at GOAmazon). This would imply conditional instability available to deep convection, even under CWV conditions for which little occurs. Additionally, at the GOAmazon site, the lower CWV cases are more buoyant than the higher CWV cases. This is largely because, on average, 1000 mb moisture is similar across CWV values at GOAmazon, yet the free troposphere is cooler on average for lower CWV (not shown). This means that the parcel originating at 1000 mb starts off just as buoyant as the high CWV parcels, but then travels through cooler, denser air aloft, enhancing parcel buoyancy. The excessive buoyancy for this case occurs even without the inclusion of freezing, which tends to enhance buoyancy in the upper troposphere.

In comparison to the no mixing case, the constant-mixing case shows some improvement in matching buoyancy with the onset of precipitation in that the buoyancy is small or negative for the lowest CWV values at both Nauru and GOAmazon (Fig. 3.7b). For the GOAmazon site, the inverse relationship between buoyancy and CWV seen in the 600-800 mb layer is still apparent, yet there exists a consistent relation to CWV in the layers above. In these figures, the rapid-freezing assumption allows the contribution of freezing to buoyancy at upper levels to be easily seen; more gradual freezing would spread this increase across the layers above. If freezing is not included,

this scheme would appear more consistent with the pickup in precipitation at Nauru (Holloway and Neelin 2009). With freezing, it suggests conditional instability through a deep layer even for fairly low values of CWV.
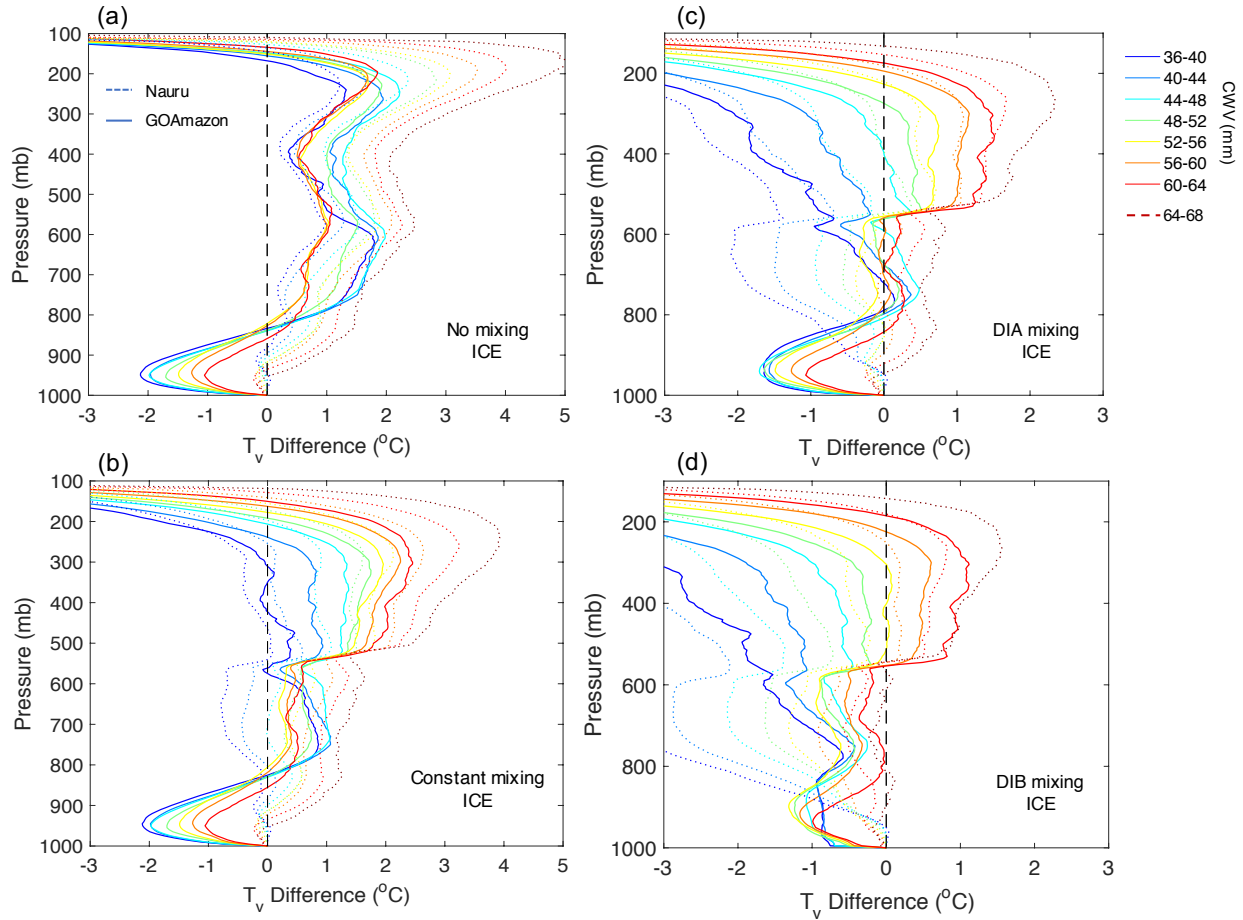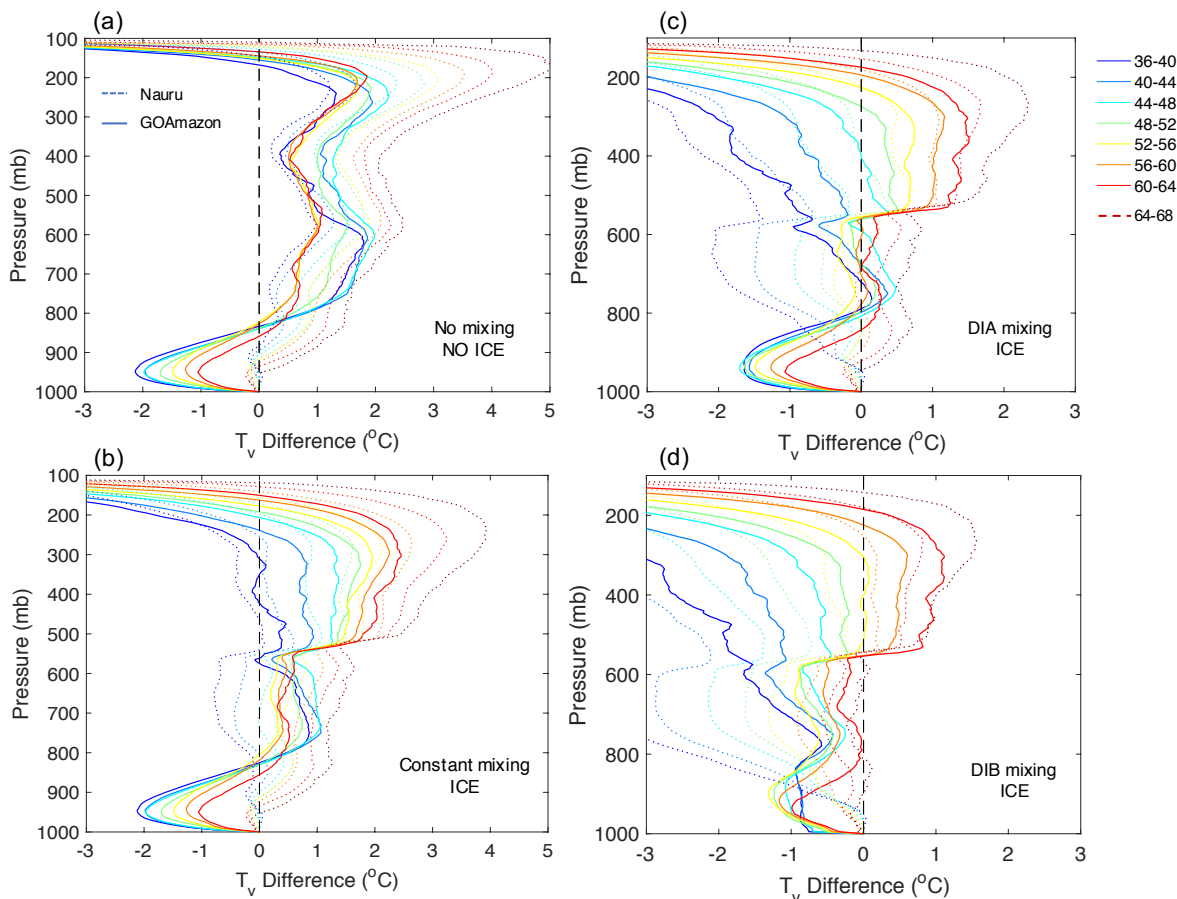

Figure 3.8: Mean virtual temperature differences between plumes originating at 1000 mb and their surrounding environments conditionally averaged by CWV for Deep-Inflow-B (solid) and constant 0.001 hPa^{-1} (dashed) mixing with ice at the GOAmazon site for (a) DJFMAM day, (b) DJFMAM night, (c) JJASON day, and (d) JJASON night.

Figure 3.7c and 3.7d show that including inflow from a substantial lower tropospheric layer using Deep-Inflow mixing yields a more robust relationship between plume buoyancies observed and the sharp increase in precipitation observed with increasing CWV (Holloway and Neelin 2009; Schiro et al. 2016) than the other relations in Figs. 3.7a and 3.7b for both land and ocean cases. It should be noted that these calculations can be sensitive to microphysical assumptions (not shown),

such as the removal of condensate within the calculation, which can increase buoyancies in the lower-mid troposphere. Overall, for a plume originating from the boundary layer, mean plume buoyancies with respect to CWV are most consistent with the sharp increase in precipitation observed throughout the depth of the troposphere for assumptions that include substantial mixing through a deep lower tropospheric layer over both land and ocean.

Figure 3.8 examines the GOAmazon case in greater detail. Since there is more variability in the moisture vertical structure as a function of time of day and season at this site, we can gain insight from how moisture variability affects buoyancy and thus the onset of deep convection. We examine this by checking for consistency between the observed moisture-precipitation relations and the onset as given by the buoyancy profiles. Results are shown for buoyancies computed using constant mixing with freezing (0.001 hPa^{-1}, dashed lines, as in Fig. 3.7b) and Deep-Inflow-B with freezing (as in Fig. 3.7d, solid lines) for plumes originating at 1000 mb. The onset occurs at lower total CWV in the dry season than the wet season, and in the daytime compared to nighttime, as is shown in Fig. 3.3. This is most likely a result of the greater moisture in the boundary layer and lower free troposphere for the same CWV values (see Fig. 3.2), yielding more buoyancy.

For the case of constant mixing, the boundary layer and lower free troposphere are treated unequally, placing greater weight on the boundary layer. The constant mixing case appears to be too buoyant (in the sense that it predicts deep conditional instability at CWV values for which little precipitation is observed) at all times. Increasing the entrainment coefficient helps to a certain extent (see Fig. 3.S7), but since it decreases buoyancy relatively uniformly throughout the whole column, rather than enhancing mixing in the lower troposphere only, there is an upper limit to the coefficient before significantly reducing buoyancy above the freezing level to values no longer consistent with deep convection. Raising the parcel from above the boundary layer also reduces

the spurious prediction of deep conditional instability at intermediate CWV values to some degree (see Fig. 3.S8), although it is unphysical to assume a parcel originates from 925 mb all the time. Overall, the constant-mixing is limited in its representation of diurnal and seasonal variability in convective onset as a function of CWV. This suggests that its weighting of lower tropospheric air, placing greater emphasis on boundary layer air, is not optimal.

For the Deep-Inflow mixing case, which accounts for nearly equal weights of boundary layer and free tropospheric humidity, the range of CWV values at which the plumes become positively buoyant ($\Delta T_v > 0$) is generally consistent with the approximate CWV values at which the onset can be observed in Fig. 3.3 for all times of day and seasons. While we are careful not to suggest this as the optimal weighting, we note that mixing of such proportions can capture diurnal and seasonal variability in buoyancy consistent to the observed onset. The ratio of free tropospheric moisture to boundary layer moisture varies seasonally and diurnally (Fig. 3.2), but the consistency between the observed onset and Deep-Inflow mixing suggests that this variability appears less important than the total moisture content. In other words, the Deep-Inflow scheme appears to be giving sufficient weight to lower tropospheric moisture, consistent with its importance as a key thermodynamic variable controlling convective onset.

3.5.3 *Onset of deep convection as a function of buoyancy*

We now examine how strong a relation to observed deep convection an integral measure of buoyancy can yield. For simplicity, we use the mean buoyancy from 200-1000 mb as the integral measure, since we want to consider a quantity that transitions smoothly from negative to positive and includes both the lower and upper troposphere. Fig. 3.9 shows the histograms of convection type and probabilities of precipitation for three mixing cases: no mixing without freezing (top panel), constant mixing (0.001 hPa^{-1} with ice (middle panel) and Deep-Inflow-B mixing with ice

67
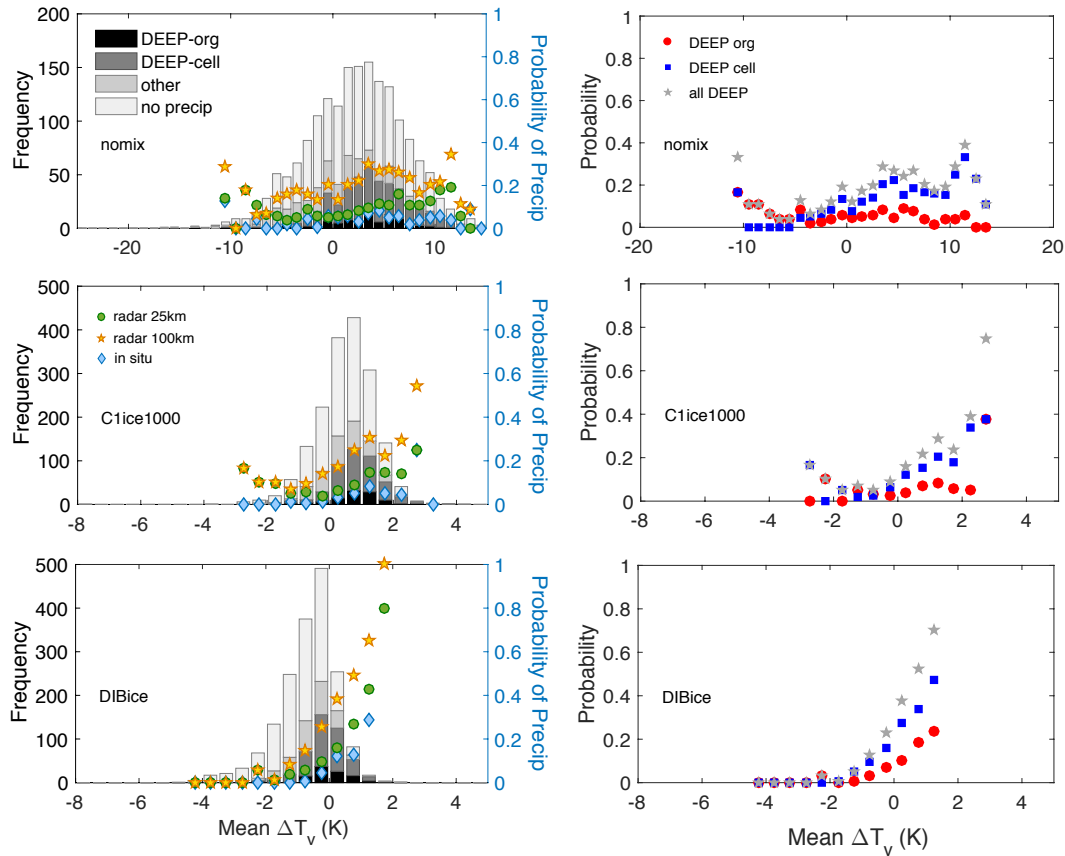
Figure 3.9: Same as Fig. 5, but probabilities and frequencies are conditionally averaged by mean tropospheric virtual temperature difference (buoyancy) between a plume originating at 1000 mb and the surrounding environment for constant mixing with ice (0.001 hPa^{-1}; top row) and DIB with ice (bottom row).

(bottom panel). Deep-Inflow-A behaves similarly to Deep-Inflow-B, so we choose the latter as the case with deepest inflow to provide a sense of the bounding behavior. Given that layer integrated water vapor quantities exhibit strong relations to a pickup in precipitation probability, we seek a buoyancy-based calculation showing at least as strong a relationship.

Precipitation probability conditioned on buoyancy computed using a Deep-Inflow mixing assumption indeed yields a strong pickup above a threshold value. In this sense, Deep-Inflow-B buoyancy can be termed a good predictor for precipitation probability. Precipitation probabilities conditioned on buoyancies computed using no mixing or constant mixing yield less strong relationships. As mentioned previously, increasing the entrainment coefficient in the constant-

entrainment case helps somewhat, but increasing it too much tends to shift the entire plot toward

negative buoyancies. Buoyancies start becoming strongly negative before a relation that closely

resembles that between precipitation and buoyancy from Deep-Inflow mixing emerges.
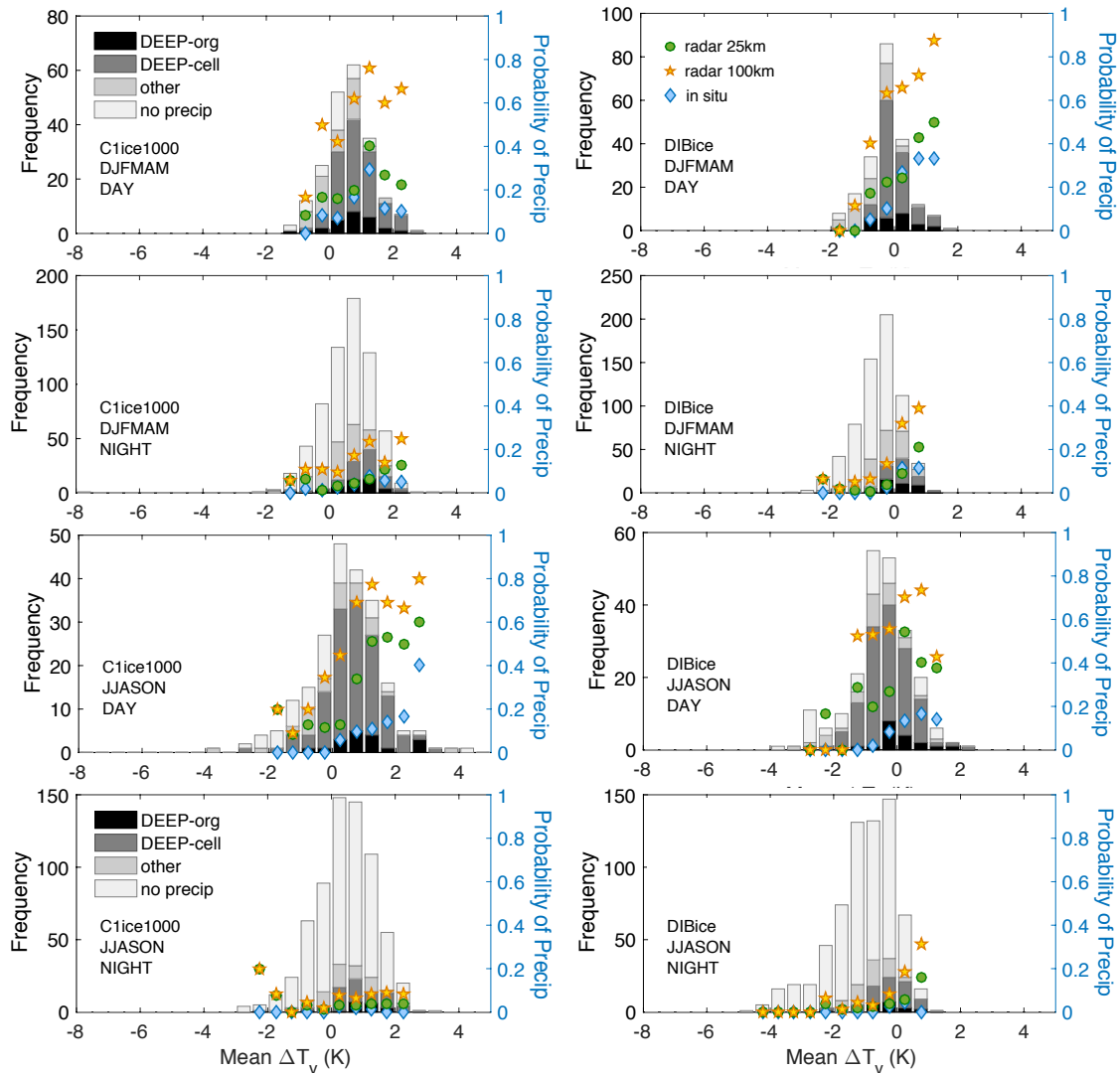
Figure 3.10: Probability and frequency of precipitation and deep convection conditionally averaged by mean tropospheric virtual temperature difference (buoyancy) between a plume originating at 1000 mb and the surrounding environment for various times of day and seasons. (left column) Buoyancies computed using constant mixing with ice (0.001 hPa^{-1}). (right column) Buoyancies computed with DIB mixing with ice.

We then explore the potential utility of the two buoyancy computations as predictors of

precipitation probability across seasons and times of day in Fig. 3.10. The no-mixing case is not

considered because it tends to behave poorly (shown in Fig. 3.S9 of the supplemental material for

reference). Both mixing assumptions show an increase in the probability of precipitation with increasing buoyancy during the daytime when the boundary layer has a more robust relation to the precipitation (Fig. 3.6), but differences can be seen at nighttime by comparing the constant mixing case in the left column to the Deep-Inflow-B case. There is a strong relationship to 700-900 mb humidity across the diurnal and seasonal cycles (Fig. 3.5), and thus assumptions that more heavily weight the contribution of the lower free troposphere to parcel buoyancies will show a more consistent relation to the probability of precipitation. At nighttime, when the boundary layer exerts less influence, the Deep-Inflow-B case performs better than the constant mixing case originating at 1000 mb. This suggests that a scheme that uses an appropriate weighting of plume inflow between the free troposphere and boundary layer is important for adequate representation of nocturnal convection.

Fig. 3.11 examines the utility of these assumptions as predictors of deep convection occurring in organized systems versus unorganized convection. One can ask whether buoyancy based on a single mixing parameterization can yield strong relationships to probability of precipitation for both organized and local convection. The constant mixing case (left column), is more limited than the Deep-Inflow case as a predictor of both organized and unorganized convection. In particular, the relation between plume buoyancy and organized convection is stronger for the Deep-Inflow case. This is consistent with the relation between organized convection and humidity apparent in Figs. 3.5 and 3.6, particularly in relation to lower free tropospheric humidity in the nighttime cases. This is suggestive of a single scheme's applicability to both organized and unorganized convection for convective closure. Moreover, using a mixing assumption that includes sufficient mixing from the lower free troposphere, a similarly strong relation to that of deep convection and humidity is captured by an integral buoyancy measure.
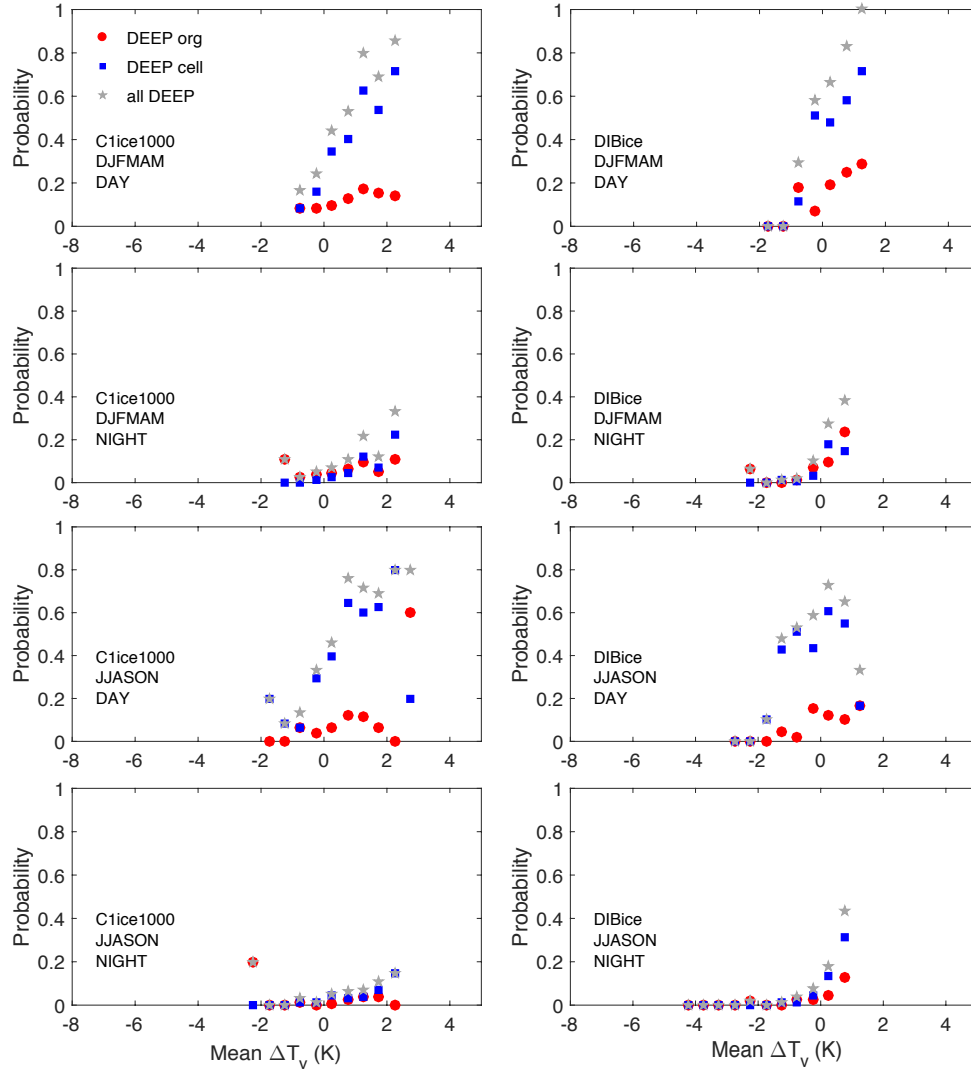
Figure 3.11: Probability of deep convection as determined by the fraction of total events that are deep convective (DEEP-cell and DEEP-org, red circles) and the fraction of all events that are organized deep convective events (blue squares). Probabilities are conditionally averaged by mean tropospheric virtual temperature difference (buoyancy) between a plume originating at 1000 mb and the surrounding environment for various times of day and seasons. (left column) Buoyancies computed using constant mixing with ice (0.001 hPa^{-1}). (right column) Buoyancies computed with DIB mixing with ice.

Overall, these results suggest that plume models without sufficient influence of the lower free troposphere are less successful predictors of deep convection. A single plume formulation with a similar weighting of air mixing in through a deep lower tropospheric layer to that of Deep-Inflow-B used here is likely to, however, exhibit skill as a predictor of deep convection.

71

3.6   Conclusions

A robust relation between CWV and precipitation over land and ocean provides a useful model constraint for the onset of deep convection. The GOAmazon campaign (2014-2015) near Manacapuru, BR provides a unique opportunity to examine this relation in greater detail by studying the interaction between variability in moisture vertical structure and the conditional instability of the environment. Results shown previously for a tropical oceanic environment at the DOE ARM site at Nauru in the tropical western Pacific are examined as a basis for comparison.

There is little variability in moisture vertical structure across the seasonal and diurnal cycle at Nauru. The Amazon, however, has both a distinct seasonal and diurnal cycle in moisture vertical structure and associated variability. This makes the Amazon a good test case for examining variability in the moisture field and its effects on deep convection in the tropics. Mean moisture profiles show that the boundary layer at Nauru is moister than in the Amazon, while the lower free troposphere is drier. Moisture variance is large in the free troposphere at Nauru and the GOAmazon site. The maximum (near 800 mb) is larger at Nauru than GOAmazon, and over land this maximum (~700 mb) is most evident in the drier months. During the wet season, moisture is less variable and more uniform throughout the column.

Over land, where larger diurnal and seasonal cycles exist, the onset to deep convection is strongly tied to free tropospheric moisture across all seasons and times of day, whereas the onset shows a strong relation to boundary layer moisture during the daytime only. The onset is characterized by the occurrence of locally-occurring cellular convection, as well as larger, organized convective systems. During the daytime, local cellular convection is the most common convection type whereas larger-scale, organized convective systems are a larger fraction of the total convection occurring during nighttime. The probability of organized convection increases

sharply with increasing lower free tropospheric humidity, whereas the relation to boundary layer moisture is less discernible. The probability of isolated cellular convection, however, is strongly tied to both lower free tropospheric moisture and boundary layer moisture. Isolated cellular convection occurs at lower values of lower free tropospheric humidity than organized convection, most probably due to the strong influence of the boundary layer on isolated cells. The influence of the boundary layer is primarily confined to the daytime, whereas the lower free tropospheric moisture is strongly tied to both daytime and nocturnal convection.

Variability in lower tropospheric humidity accounts for variability in the conditional instability of the environment, as estimated from buoyancy computations, and thus the onset of deep convection over both land and ocean, and across the seasonal and diurnal cycles to leading order. CWV is reaffirmed as a good proxy for conditional instability, yet since differences exist in the total moisture content of the lower troposphere for a given CWV regionally, seasonally, and diurnally, differences are thus observed in the observed onset of precipitation with CWV. For instance, more moisture in the daytime boundary layer and lower free troposphere for a given CWV allow for the onset of deep convection to occur at lower CWV in the dry season daytime than wet season daytime at the GOAmazon site. Furthermore, the large range of environmental conditions across day and night and for the wet season and dry season at the GOAmazon site permits inferences to be made about the relative success of different mixing assumptions as predictors of deep convective conditions. The criterion here is whether buoyancy computations based on a giving mixing scheme (as summarized by an integrated buoyancy measure) can yield a strong relationship to the pickup in probability of precipitation. Given that the pickup can be seen as a function of layer integrated water vapor, a buoyancy computation should yield at least as

distinct a relationship to be considered successful. This comparison can be carried out separately for organized and unorganized convection.

A plume buoyancy formulation with deep inflow through a deep lower tropospheric layer shows that a single plume formulation can capture this leading order behavior across tropical land and ocean, across seasons and times of day, and for both organized and unorganized convection. Rather than suggesting an exact formulation for an optimal profile, we provide evidence that a single, physically-based plume computation with an appropriate weighting of lower free tropospheric humidity can be a useful predictor of deep convection across a range of scales. This does not exclude the need for explicit treatments of organized convection (e.g. Mapes and Neale 2011; Khouider and Moncrieff 2015), but it does suggest that a Deep-Inflow framework for mixing in the buoyancy calculations can be useful even in presence of organization. We interpret this as the organized convection being sustained by the same basic mechanisms driving buoyancy, with the inflow of environmental air into updrafts coming from a roughly similar deep layer in both cases. Even when the mesoscale systems are pre-existing and propagating into the region where the sounding is observed, lack of conditional instability (given suitable inflow assumptions) yields low probability of that system continuing to produce precipitation. The results here suggest implementing Deep-Inflow mixing in a convective parameterization would be warranted, although it is an open question whether this change alone would be sufficient to reduce long-standing precipitation biases in regions like the Amazon.

3.S   Supplemental Material

3.S.1 *Data*

Figure 3.S1 is similar to Figure 3.3, but for all seasons, and shows a comparison of results from the MWR raw data using three methods of gap-filling and filtering points for which the
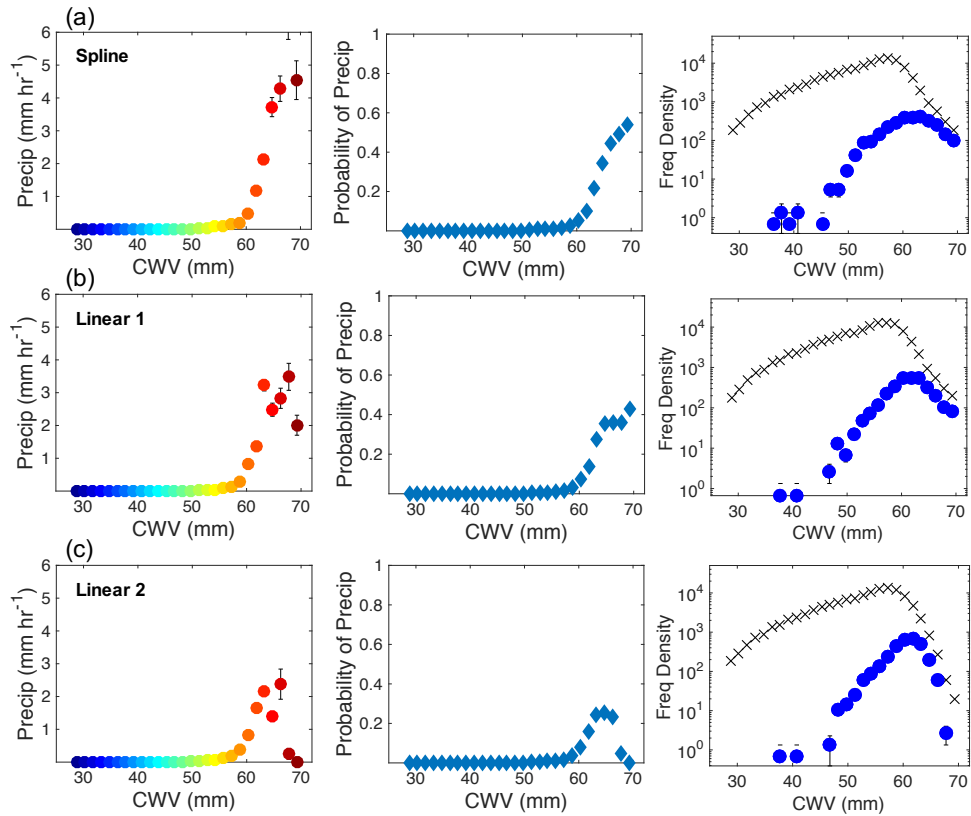
Figure 3.S1: A comparison of various interpolation methods used to gap-fill microwave radiometer data at times when the instrument is not recording (mostly raining times) over periods of 6 hours or less: (a) Cubic spline interpolation, (b) linear interpolation similar to Schiro et al. (2016), and (c) linear interpolation like that used in Fig. 3.3.

radiometer CWV may be affected by rain (wet-window problem). Figure 3.S1a,c compare cubic spline interpolation with linear interpolation. A threshold of 100 K in the 23.8 GHz channel is used to filter out points affected by rain, unless otherwise noted. Additionally, data in a 1-month period surrounding the equinoxes is removed from 11:00 − 13:00 LT due to instrument malfunction. Figure 3.S1b,c compare results using the above filtering procedure to those presented in Schiro et al. (2016) using the 31.4 GHz channel. The spline interpolation is possibly more often correct than the linear interpolation, given that CWV is often increasing at the beginning of the gap and decreasing afterward, but we cannot exclude that it could create artificial high values. The method of Fig. 3.S1c is the most conservative, and is thus chosen for use in Fig. 3.3 using the most

conservative dataset (MWRRET). Although it likely underestimates results at high CWV values, it guards against any possible overestimates in this range.

3.S.2 *Classification of Organized vs. Unorganized Convection*

Fig. 3.S2 shows three radar images as examples of deep convective events occurring within 100 km of the GOAmazon site. Fig 3.S2a typifies unorganized cellular convection, meeting the criteria outlined in Section 3.2, and is classified as DEEP-cell throughout the study. Fig. 3.S2b is a convective cell that exhibits some degree of organization, but is less than the typical 100 km threshold characteristic of MCSs (Houze 2004). Convection of this nature are grouped into the DEEP-org category, following the criteria outlined in Section 3.2. Lastly, Fig. 3.S2c is a well-defined MCS with a leading line of convective cells and trailing stratiform region, a common MCS type occurring in the Amazon basin. This is also classified as organized within our definition.

3.S.3 *Moisture Vertical Structure*

In Fig. 3S.3a, the CWV value for each sounding in the wetter months is correlated to the moisture at each 5 mb vertical level for daytime (solid, light blue) and nighttime (dashed, dark blue) soundings. The daytime soundings show strong positive correlation to CWV in the boundary layer and free troposphere, with a local minimum in the layers right near cloud base. In the drier months (Fig. 3.S3b), the correlations at every level are higher.

3.S.4 *Convective Onset Statistics*

Fig. 3S.4 presents a sensitivity study to examine whether any layer in the free troposphere exerts greater control over the onset to deep convection. It is evident from this plot (left panel) that the layer < 500 mb exhibits less of a relation to the onset than in other layers. The 700-900 mb has a very robust relation to the precipitation observed. The 500-700 mb layer shows a reasonably strong relation as well, but there is more precipitation observed over a much wider range of
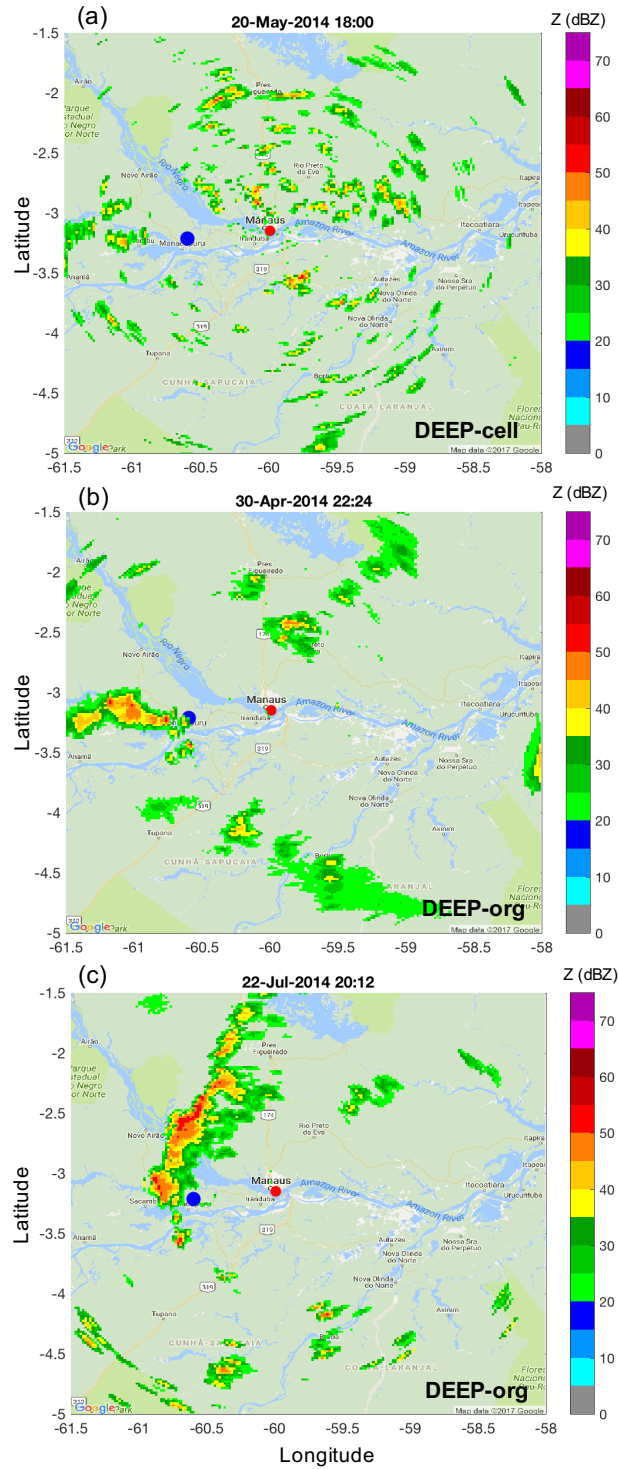
Figure 3.S2: Examples from S-Band Radar on 20 May 2014 at 18:00 UTC (14:00 LT) for a case of isolated, cellular convection (DEEP-cell), at 30 Apr 2014 at 22:24 UTC (18:24 LT) for a case of organized convection between 50-100 km in horizontal extent (DEEP-org), and on 22 Jul 2014 at 20:12 UTC (16:12 LT) for a case of organized convection exceeding 100 km in one direction (MCS). The red dot indicates the location of the S-Band radar, and the blue dot indicates the location of the main GOAmazon site (T3).
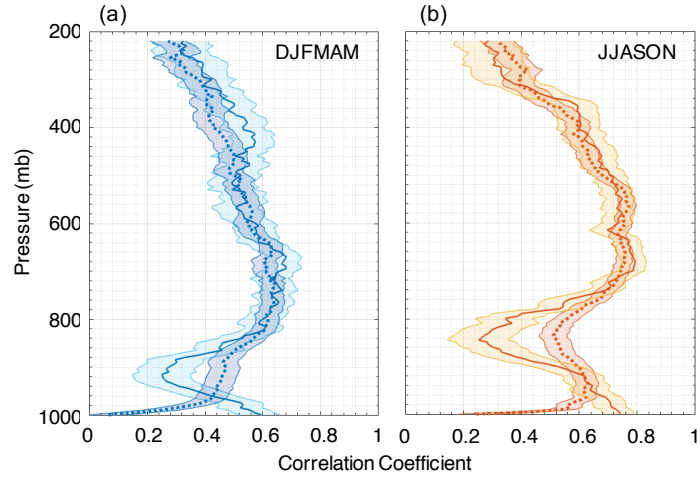
Figure 3.S3: Correlation coefficient between CWV and specific humidity in each 5 hPa layer for (a) DJFMAM and (b) JJASON for daytime (light shading, solid lines) and nighttime radiosondes (dark shading, dashed lines).
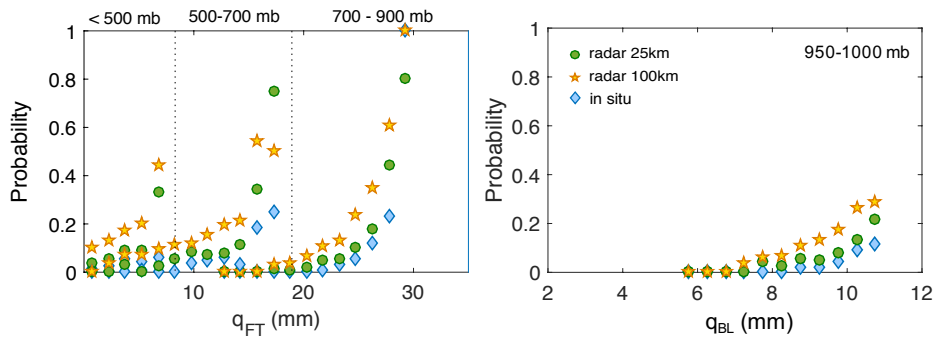
Figure 3.S4: Sensitivity test for the humidity-precipitation relation for various definitions of free tropospheric (left) and boundary layer (right) humidity.
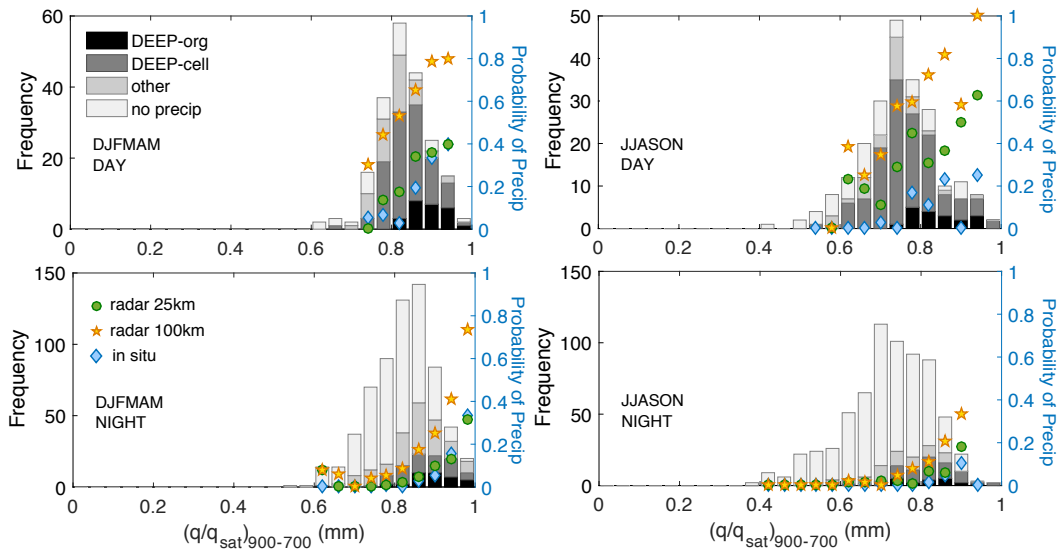
Figure 3.S5: Same as Fig. 3.5 (left column), but for values of 700-900 mb saturation.
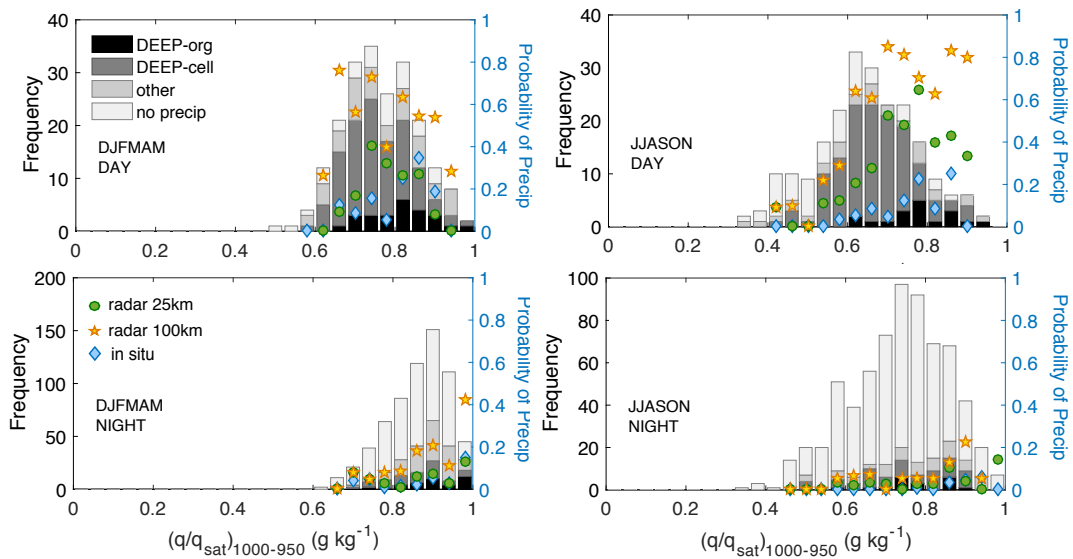
Figure 3.S6: Same as Fig. 3.6 (left column), but for values of boundary layer (1000-950 mb) saturation.
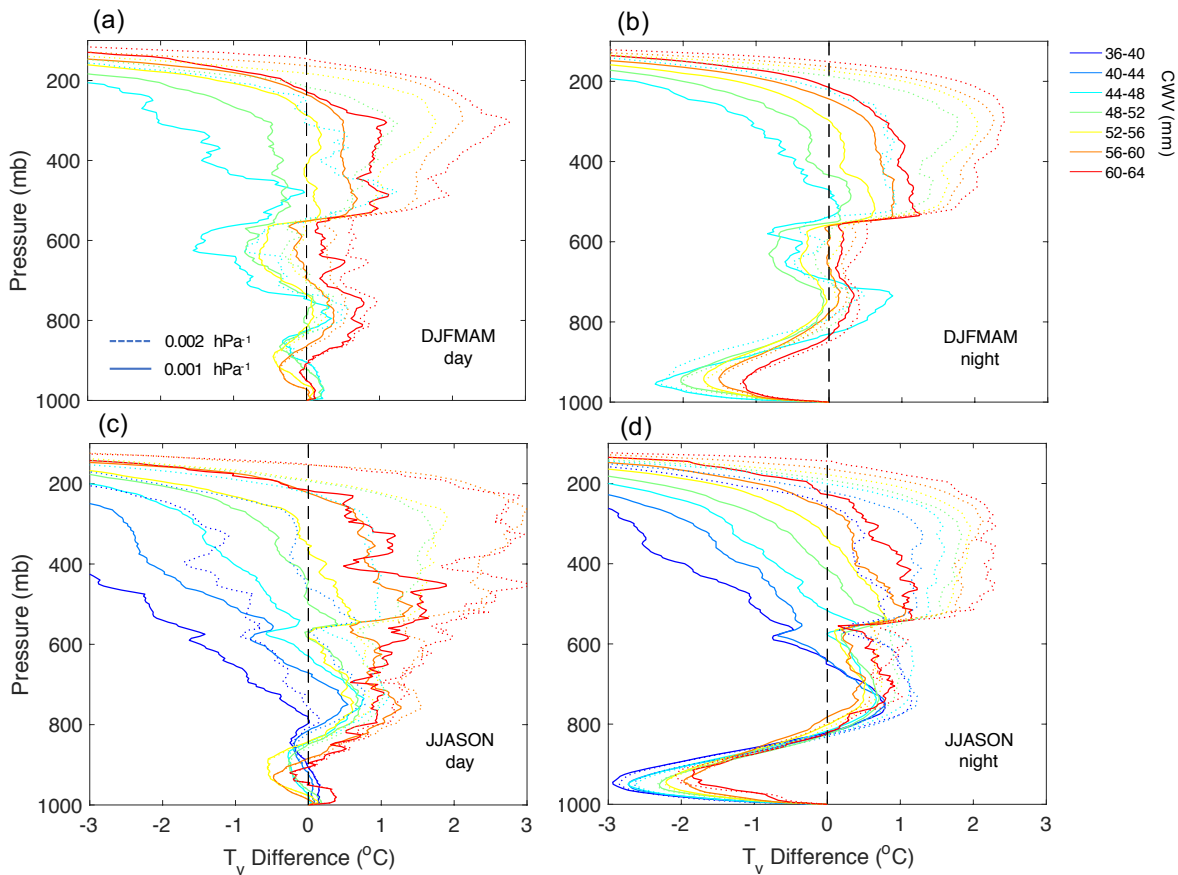
Figure 3.S7: Mean virtual temperature differences between plumes and their surrounding environments conditionally averaged by CWV for constant mixing at a rate of 0.001 hPa^{-1} (solid) and 0.002 hPa^{-1} at the GOAmazon site for (a) DJFMAM day, (b) DJFMAM night, (c) JJASON day, and (d) JJASON night.

humidity within this layer. Overall, this supports our choice to define the lower free troposphere between 700-900 mb throughout the study.

To consider the effects of temperature in the analysis presented in Figures 3.5 and 3.6, Figure 3.S5 plots integrated moisture in the 700-900 mb layer divided by the saturation specific humidity. The relation to column saturation is just as strong as that shown in Fig. 3.5 for the 700-900 mb specific humidity. In the daytime in the drier months, the onset occurs at lower column saturation than during the daytime in the wetter months; the onset at nighttime occurs at 80% humidity or greater. This is also true in Fig. 3.S6 for the boundary layer (approximated as 950-1000 mb), although more scatter is seen in the observations.

3.S.5 *Buoyancy Computations*

Fig 3.S7 shows plume buoyancies given two constant rates of mixing: 0.001 hPa^{-1}, the same as is used throughout the study, and a doubling of this rate (0.002 hPa^{-1}), which was referred to as C2 in Sahany et al. (2012). As discussed in the main text, increasing the mixing coefficient helps to show more consistent relation between the buoyancy curves and the corresponding increases in precipitation (Fig. 3.3), increasing the entrainment coefficient helps to a certain extent, but does not better consistency compared to the Deep-Inflow assumptions (Fig. 3.8). Increasing the coefficient any more reduces buoyancies in the upper troposphere significantly.

Fig. 3.S8 shows the results divided by time-of-day and season for the constant mixing case lifted from 925 mb. This is roughly at the top of the boundary layer in the daytime, and is above the nocturnal boundary layer. Overall, raising the plume from 925 mb does not show considerable improvement over the 1000 mb case: daytime buoyancies are lesser, yet still consistent with the onset observed, whereas buoyancies in the dry season are too high with freezing included. Plumes should originate from the most unstable layer, however, which is usually the boundary layer.
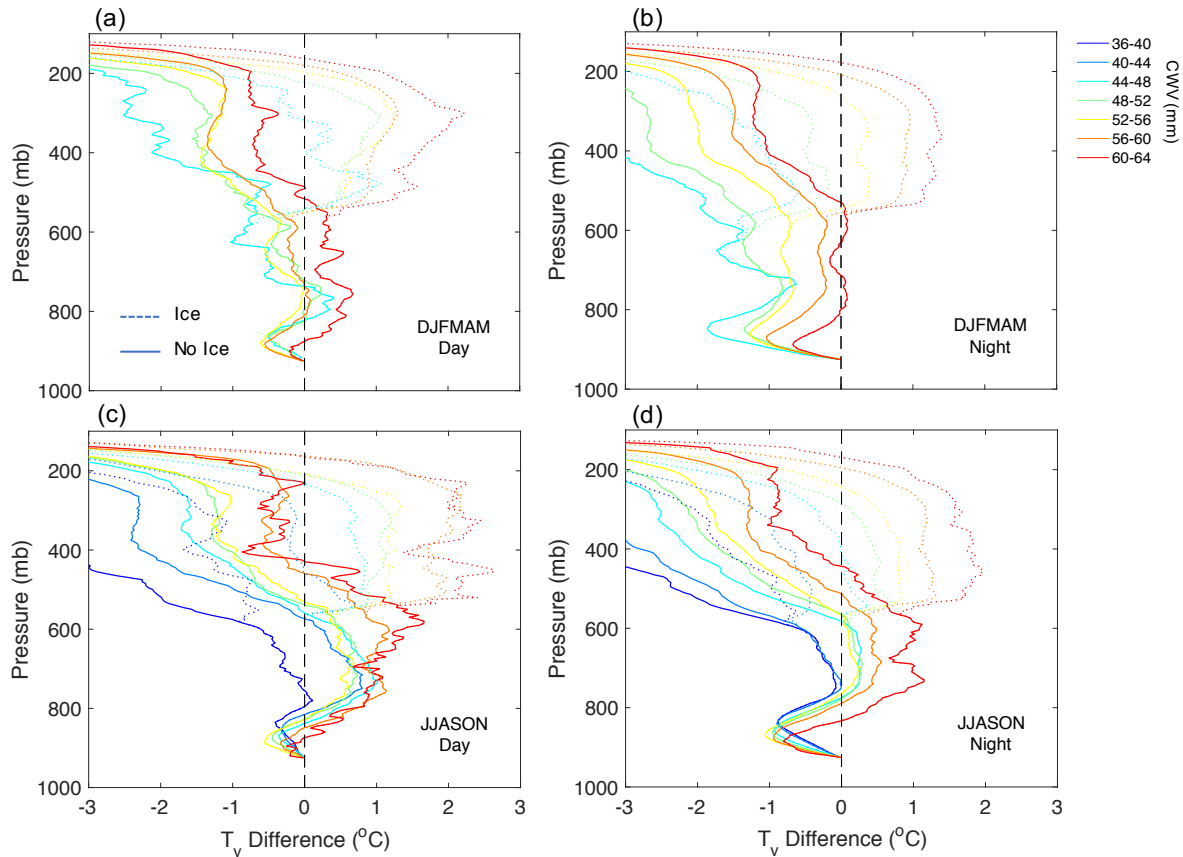
Figure 3.S8: Mean virtual temperature differences between plumes originating at 925mb and their surrounding environments conditionally averaged by CWV for constant mixing at a rate of 0.001 hPa^{-1} at the GOAmazon site for (a) DJFMAM day, (b) DJFMAM night, (c) JJASON day, and (d) JJASON night. Dashed lines show buoyancies for plumes in which all condensate (retained) is frozen at 0°C; solid lines do not include the effect of freezing.

Lastly, Fig. 3.S9 reiterates the fact that plume buoyancies computed without mixing are unrealistic as predictors of precipitation.
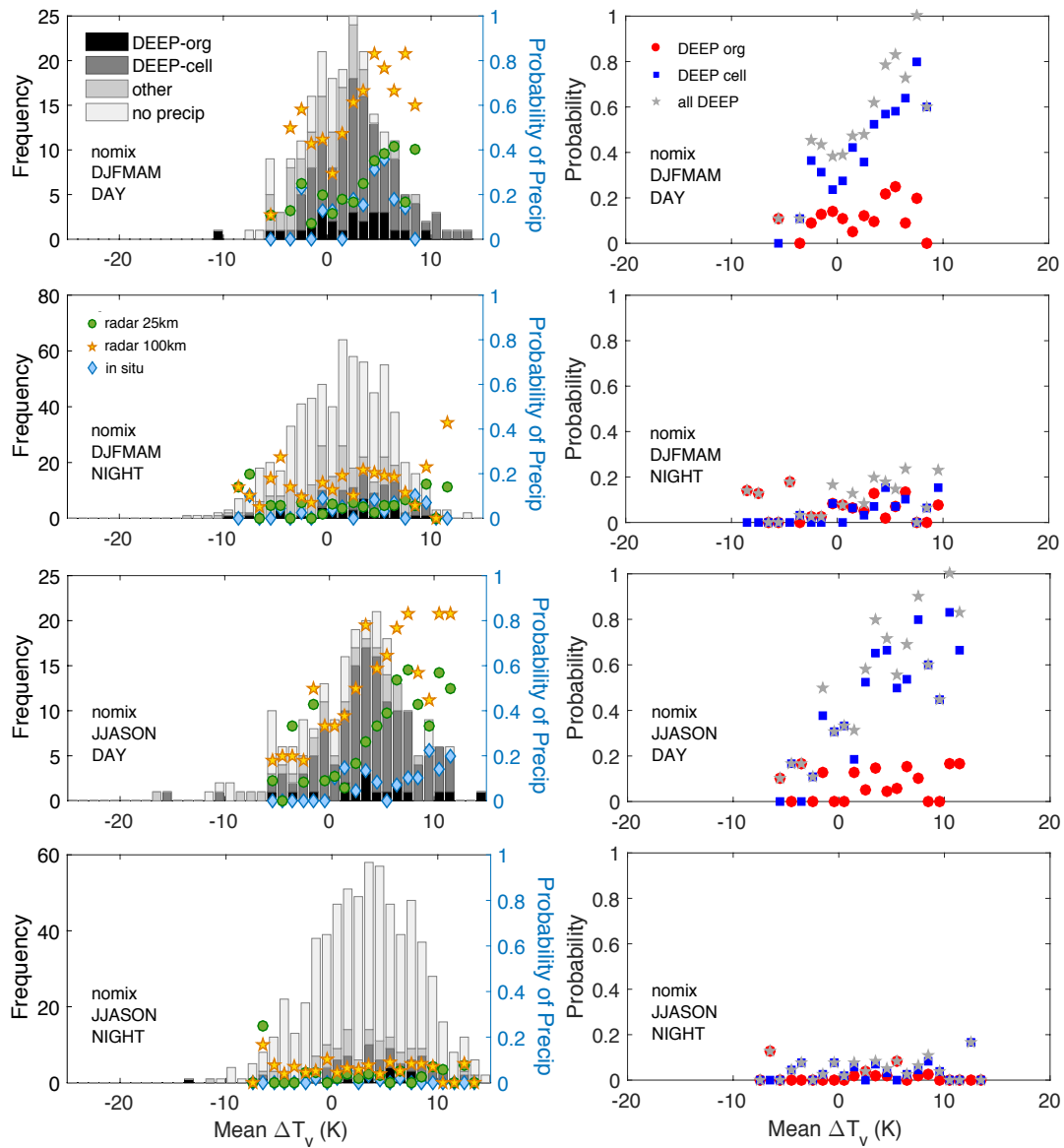
Figure 3.S9: Same as Fig. 3.5, but probabilities and frequencies are conditionally averaged by mean tropospheric virtual temperature difference (buoyancy) between an undilute plume originating at 1000 mb and the surrounding environment.

CHAPTER 4

Tropical Continental Downdraft Characteristics: Mesoscale System versus

Unorganized Convection

Abstract

Downdrafts and cold pool characteristics for mesoscale convective systems (MCSs) and isolated, unorganized deep precipitating convection in the Amazon are composited and compared using two years of data from the GOAmazon campaign. For both MCSs and isolated cells, there are increases in column water vapor (CWV) and surface fluxes observed in the two hours leading the convection and an increase in wind speed, decrease in surface moisture and temperature, and increase in relative humidity coincident with system passage. Composites of vertical velocity data and radar reflectivity from a radar wind profiler show that the downdrafts associated with the sharpest decreases in surface θ_e have a probability that increases towards lower levels throughout the lowest 4 km. Both MCSs and unorganized convection show similar mean downdraft magnitudes and probabilities with height. This is consistent with thermodynamic arguments: if θ_e is approximately conserved following descent, a large fraction of the air reaching the surface likely originates at altitudes in the lowest 2 km. Mixing computations suggest that, on average, air originating at heights greater than 3 km would require substantial mixing, particularly in the case of isolated cells, to match the observed cold pool θ_e. Precipitation conditionally averaged on decreases in surface equivalent potential temperature ($\Delta\theta_e$) exhibits a strong relationship simply because the largest $\Delta\theta_e$ values are associated with high probability of precipitation. The more physically motivated conditional average of $\Delta\theta_e$ on precipitation levels off with increasing precipitation rate, bounded by the maximum difference between surface θ_e and its minimum in the profile aloft.

Precipitation values greater than about 10 mm/hr are associated with high probability of $\Delta\theta_e$ decreases. Robustness of these statistics observed across scales and regions suggests their potential use as model diagnostic tools for the improvement of downdraft parameterizations in climate models.

4.1   Introduction

Convective downdrafts involve complex interactions between dynamics, thermodynamics, and microphysics across scales. They form cold pools, which are evaporatively cooled areas of downdraft air that spread horizontally and can initiate convection at their leading edge (Byers and Braham 1949; Purdom 1976; Wilson and Schreiber 1986; Rotunno et al. 1988; Fovell and Tan 1998; Tompkins 2001; Khairoutdinov and Randall 2006; Lima and Wilson 2008; Khairoutdinov et al. 2009; Boing et al. 2012; Rowe and Houze 2015). The boundary between the cold pool and the surrounding environmental air, known as the outflow boundary or gust front, is the primary mechanism for sustaining multi-cellular deep convection (e.g. Weisman and Klemp 1986). It has also been shown to trigger new convective cells in marine stratocumulus clouds (Wang and Feingold, 2009; Terai and Wood, 2013) and in trade-wind cumulus (Zuidema et al. 2011; Li et al., 2014). Downdrafts also have implications for new particle formation in the outflow regions, which contribute to maintaining boundary layer CCN concentrations in unpolluted environments (Wang et al. 2016).

Precipitation-driven downdrafts are primarily a result of condensate loading and the evaporation of hydrometeors in unsaturated air below cloud base (e.g. Houze 1993). Some studies claim that the effects of condensate loading are greater than those of evaporative cooling (Torri and Kuang, 2016); others say that evaporation is the main driver (Knupp and Cotton 1985; Srivastava 1987). It was originally suggested by Zipser (1977) that the downdrafts in the

convective part of a system are saturated, referred to in the literature as convective-scale downdrafts, and the downdrafts in the trailing stratiform region (referred to as mesoscale downdrafts) are unsaturated. Studies with large-eddy simulations (LES; Hohenegger and Bretherton 2011; Torri and Kuang 2016) indicate, however, that most convective downdrafts are unsaturated, consistent with evidence that the evaporation of raindrops within the downdraft likely does not occur at a sufficient rate to maintain saturation (Kamburova and Ludlam 1966).

More recently, studies have shown the importance of downdraft parameters in maintaining an accurate simulation of tropical climate in global climate models (GCMs; Maloney and Hartmann 2001; Sahany and Nanjundiah 2008). Accurate simulation of MCSs in continental regions (Pritchard et al. 2011) was also shown to be sensitive to downdraft-boundary layer interactions, with significantly improved representation of MCS propagation in the central US once such interactions were resolved. Additionally, representing the effects of downdrafts and cold pools in models has been shown to have positive effects on the representation of the diurnal cycle of precipitation (Rio et al. 2009; Schlemmer and Hohenegger 2014).

This study aims to characterize the physics of downdrafts in a comprehensive way in the Amazon for both isolated and mesoscale convective systems, and to provide useful guidance for downdraft parameterization in GCMs. The DOE-Brazil Green Ocean Amazon (GOAmazon) campaign (2014-2015) provides an unprecedented opportunity to evaluate downdraft characteristics for the first time in the Amazon with sufficiently large datasets for quantifying robust statistical relationships describing leading order processes. Relationships explored previously, primarily in tropical oceanic or mid-latitude regions, are revisited and compared to our findings over the Amazon. Downdrafts in MCSs and isolated cells will be compared, to inform decisions concerning their unified or separate treatment in next generation models. The effect of

downdrafts on surface thermodynamics and boundary layer recovery will be examined, and the origin height of the downdrafts will be explored, combining inferences from radar wind profiler data for vertical velocity and thermodynamic arguments from simple plume models. Lastly, statistics describing cold pool characteristics at the surface will be presented and discussed for possible usage as model diagnostics.

4.2   Data and Methods

Surface meteorological values (humidity, temperature, wind speed, precipitation) were obtained from the Aerosol Observing meteorological station (AOSMET) at the DOE ARM site in Manacapuru, Brazil, established as part of the GOAmazon campaign (site T3). The record used in this study spans 10 Jan 2014 – 20 Oct 2015. Values in this study are averaged at 30-min intervals. Equivalent potential temperature is computed following Bolton (1980). Sensible and latent heat fluxes (30-min) are derived from eddy correlation flux measurements obtained with the eddy covariance technique involving correlation of the vertical wind component with the horizontal winds, temperature, water vapor density, and carbon dioxide concentration. A fast-response, three-dimensional sonic anemometer is used to obtain the wind components and speed of sound, while an open-path infrared gas analyzer is used to obtain the water vapor density and carbon dioxide concentrations. Surface flux data from 01 Apr 2014 – 20 Oct 2015 are used here, with periods of missing and unreliable data excluded, as flagged by ARM.

Thermodynamic profiles are obtained from radiosonde measurements within 6 hours of a convective event. Radiosondes are launched at approximately 01:30, 7:30, 13:30, and 19:30 LT each day, with occasional radiosondes at 10:30 LT in the wet season. Profiles of vertical velocity and radar reflectivity are obtained from a 1290 MHz radar wind profiler (RWP) reconfigured for

precipitation modes. It has a beam width of $6°$ (~ 1 km at 10 km AGL), a vertical resolution of 200

m, and a temporal resolution of 5 seconds (Giangrande et al. 2016).
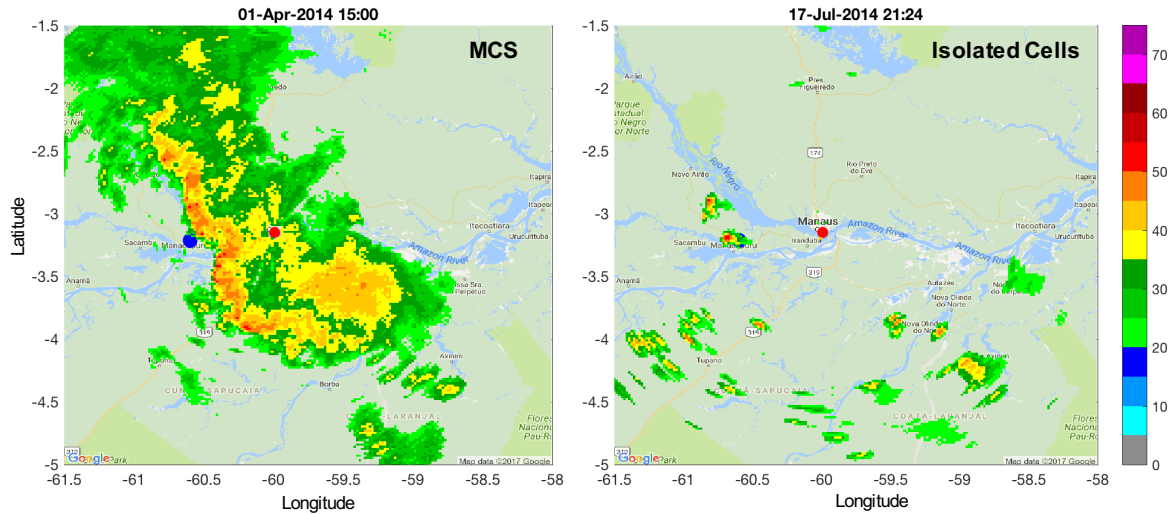
Figure 4.1: Examples from S-Band Radar on 01 Apr 2014 at 15:00 UTC (11:00 LT) before the passage of an MCS, and at 17 Jul 2017 at 21:24 UTC (17:24 LT) after the passage of an isolated cell. The red dot indicates the location of the S-Band radar, and the blue dot indicates the location of the main GOAmazon site (T3).

Precipitation data at 25 km and 100 km, as well as convection classifications, are derived

from an S-Band radar located approximately 67 km to the northeast of T3 at the Manaus Airport.

Composite constant altitude low-level gridded reflectivity maps (e.g., constant altitude plan

position indicators, CAPPIs) were generated, and the radar data were gridded to a Cartesian

coordinate grid with horizontal and vertical resolution of 2 km and 0.5 km, respectively. These

data were processed by GOAmazon instrument scientists and are available on the intensive

operational period ARM server. Rain rates were obtained from the 2.5 km reflectivity using the

reflectivity-rain rate (Z-R) relation $Z=174.8R^{1.56}$ derived from disdrometer data. The spatially

averaged rainfall rate over a 25 km and 100 km grid box were used in this study. The center of the

100 km grid box is shifted slightly to the right of center with respect to the T3 site due to reduced

data quality beyond a 110 km radius.

All convective events used in this study meet the following criteria: producing downdrafts that create a subsequent drop in θ_e at the surface of less than -5°C in a 30-min period and having precipitation rates exceeding 10 mm hr^{-1} in that same period. These criteria were chosen to examine the most intense downdraft events with the most well-defined vertical velocity signatures in the RWP data. Only data for events with complete vertical velocity data coverage over the 1-hr period spanning the passage of the convective cell(s) and centered around the maximum precipitation were composited and evaluated.

Isolated convective cells were identified by S-Band composite reflectivity, as in Fig. 1, and are defined as being less than 50 km in any horizontal dimension (contiguous pixels with reflectivity > 30 dBz) with a maximum composite reflectivity of greater than or equal to 45 dBz. Following the criteria defined above, this resulted in the selection of 11 events, all of which were in the late morning or afternoon hours between 11:00 and 18:00 LT. Mesoscale convective systems follow the traditional definition of regions of contiguous precipitation at scales of 100 km or greater (contiguous pixels with reflectivity > 30 dBz) in any horizontal dimension (e.g. Houze 1993; Houze 2004). All of the events sampled are characterized by a leading edge of convective cells with a trailing stratiform region (Fig. 4.1), which is the most common MCS type (Houze et al. 1990). The above criteria yielded 17 events: 11 in the late morning and early afternoon hours (11:00-18:00 LT) and 6 in the late evening/early morning hours (22:00-11:00 LT).

In Section 4.6, statistics are presented using the entire two year timeseries of meteorological variables at the GOAmazon site, as well as 15 years of data (1996-2010) from the DOE ARM site at Manus Island in the tropical western Pacific. One-hour averages are computed in $\Delta\theta_e$ and precipitation.

4.3. Surface Thermodynamics

Composites of surface meteorological variables are displayed in Fig. 2.2 for the 11 isolated cellular deep convective events coinciding with drops in equivalent potential temperature of -5°C or less and precipitation rates greater than 10 mm hr^{-1} (see Section 4.2). The composites are centered 3 hours before and after the time marking the beginning of the sharpest decrease in surface θ_e. All differences quoted are the differences in values between the maximum and minimum values within the 1-hr timeframe of convective cell passage, unless noted otherwise. All timeseries averaged in the composites are shifted to the mean value at 0.5 hour, the timestep immediately following the minimum $\Delta\theta_e$, and error bars on the composites are thus shown with respect to time 0.5.

In the two hours leading the convection, the CWV increases by 4.3 mm. Values of θ_e are 353.6 K on average before passage of the cell. An hour after the passage, the θ_e value drops by an average 8.9^{o}C to an average value of 344.7 K. Since the isolated convective cells observed occur in the daytime hours, the relative humidity is seen to drop steadily throughout the 3-hr period leading the convection following the rise in temperatures with the diurnal cycle. Once the cell passes, RH values rise to 81.6%, which indicates that the downdrafts are sub-saturated when they reach the surface. Temperatures drop by 4.4^{o}C to 24.9^{o}C, which is less of a drop in temperature than observed over mid-latitude sites (see Table 2 in Engerer et al. 2008 for a review of mid-latitude case studies) and specific humidity drops by 1.1 g kg^{-1} to 16.0 g kg^{-1}. Wind speeds reach 5.5 m s^{-1} on average, consistent with previous studies that document strong horizontal winds associated with the leading edges of cold pools (e.g. Fujita 1963; Wakimoto 1982), but are lower
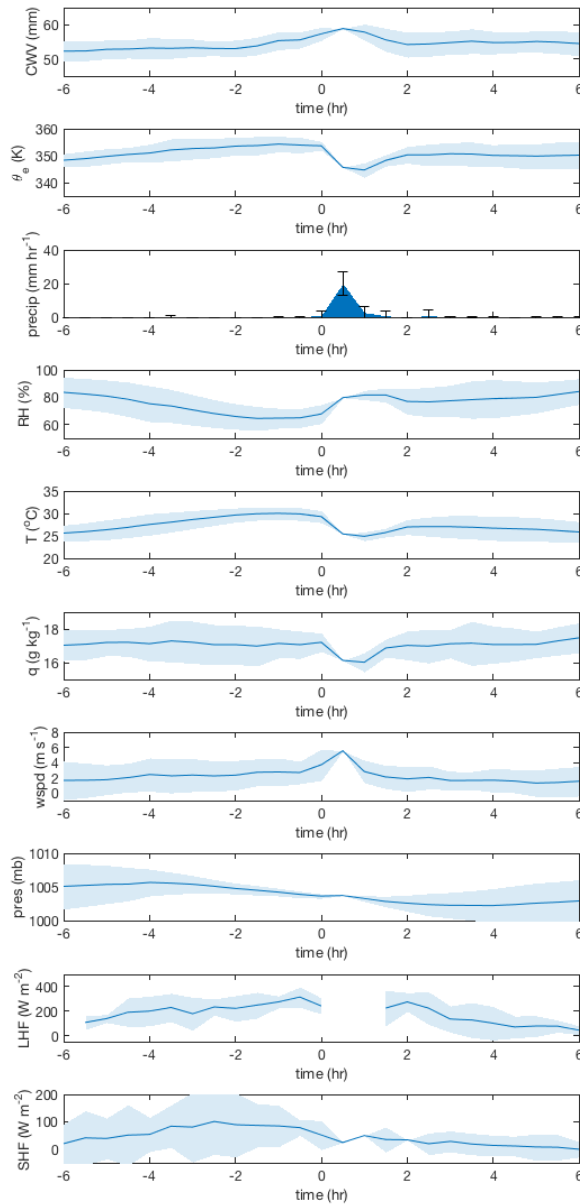
Figure 4.2: Composites of meteorological variables from the AOSMET station at site T3 6 hours leading and 6 hours lagging the 30 minute interval right before the drop in equivalent potential temperature (2nd panel) and precipitation maximum (3rd panel) coincident with the passage of isolated cells. Error bars are +/- 1 standard deviation with respect to time 0.5.

than the observed values for mid-latitude storms (Engerer et al. 2008). Additionally, surface pressure often increases with the existence of a cold pool and is referred to as the meso-high (Wakimoto 1982). Here, it increases marginally by 0.8 hPa, but this value is much less than the typical values observed in mid-latitudes (e.g. Goff 1976; Engerer et al. 2008). Lastly, 63% of the

temperature and moisture depleted by the downdraft recovers within two hours of cell passage, with moisture recovering more quickly and by a greater percentage than temperature.
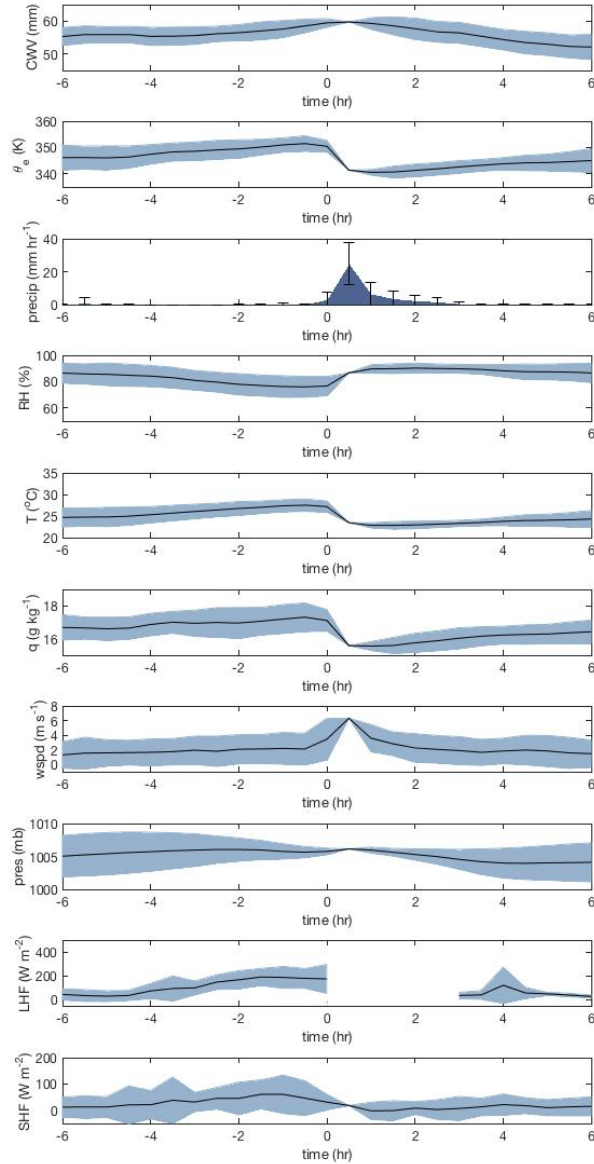
Figure 4.3: Same as Fig. 4.2, except for MCSs.

Complementary to those in Fig. 4.2, composites of surface meteorological variables are shown in Fig. 4.3 for the 17 MCSs with surface θ_e depressions of -5°C or less and coincident precipitation rates of 10 mm hr^{-1} or greater. On average, the environment is more humid, as is seen

in the CWV composite. Values of θ_e leading the passage of MCSs are a few degrees lower than the θ_e values leading the isolated cells. This is mostly due to lower surface temperatures. The precipitation occurs over a longer period than in the cases of isolated cells, as there is stratiform rain trailing the leading convective cells. The stratiform rain and associated downdrafts also sustain the cooling and drying of the near surface layers for many hours lagging the precipitation maximum. Column water vapor values leading the MCSs are slightly higher on average than observed leading the isolated cells, with an average maximum value of 59.8 mm. The relative humidity maximum in the cold pool is 90.2% (ΔRH = 14.2%), the specific humidity minimum is 15.5 g kg^{-1} (Δq = 1.7 g kg^{-1}), and the temperature minimum is 22.9^{o}C (ΔT = 4.7^{o}C), with winds gusting to an average of 6.3 m s^{-1} with the passage of the leading convective cells. The cold pools are thus cooler, drier, and nearer to saturation for the MCSs than for the isolated cells. It is worth noting that these statistics for MCSs are not greatly affected by the inclusion of nighttime events; composites for afternoon only MCSs yield similar results.

Overall, the environments in which MCSs live are moister, they have colder, drier cold pools that are nearer to saturation, the winds at their leading edges are gustier, and their boundary layers recover more slowly than for isolated cells.

4.4. Downdraft Origin and the Effects of Mixing

Many previous studies of moist convective processes use θ_e as a tracer since it is conserved in the condensation and evaporation of water and for dry and moist adiabatic processes (e.g., Emanuel, 1994). Tracing surface θ_e to its equivalent value aloft has been done before in many studies of tropical convection to examine potential downdraft origin heights (e.g. Zipser, 1969; Betts, 1973, 1976; Betts and Silva Dias, 1979; Betts et al. 2002). This follows the assumption that downdraft air conserves θ_e to a good approximation. It also assumes that downdraft air originates

at one height above ground level (AGL). Neither of these assumptions is likely to be true, as mixing is likely occurring between the descending air and the environmental air and thus originating from various levels.
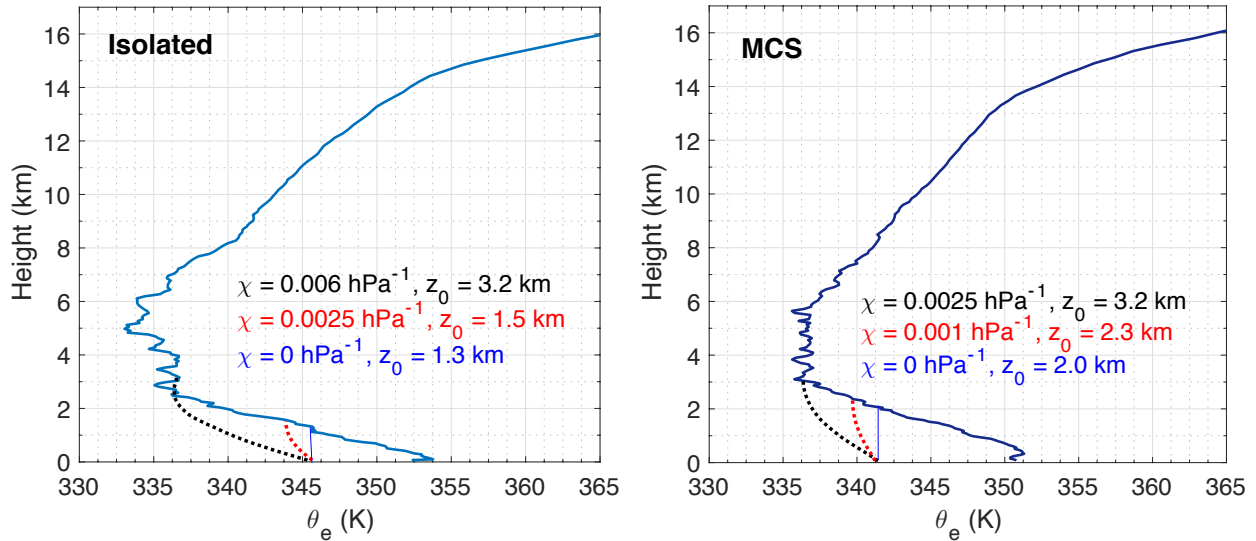
Figure 4.4: Mean profiles of θ_e for isolated cells (left) and MCSs (right) within 6 hours leading the passage of a deep convective event. Dashed lines indicate the mean descent path for plumes originating at various altitudes and mixing with its environment at various rates; solid blue line shows mean descent without mixing.

We examine the mean θ_e profiles for MCSs and isolated cells, conditioned on the existence of a substantial drop in θ_e and precipitation rates above a threshold value, to place bounds on mixing and downdraft origin with simple plume computations. Matching the minimum θ_e value observed at the surface following the passage of convection to the minimum altitude at which those values are observed yields 1.3 km for isolated cells (left panel, Fig. 4.4) and 2.0 km for MCSs (right panel, Fig. 4.4). Again, this assumes that θ_e is conserved and that all of the air originates at one altitude. If instead we assume that substantial mixing occurs with the surrounding environment and that air originates at multiple levels in the lower troposphere, it would be plausible for more of the air reaching the surface to originate at altitudes greater than 1.3 and 2 km for isolated cells

and MCSs, respectively. This has been alluded to in previous studies (e.g. Zipser, 1969; Gerken et al. 2016), providing evidence that air originates in the middle troposphere.

To examine this, we mix air from above the altitude where the θ_e matched the surface value is shown in the composites in Figs. 4.2 and 4.3 downward towards the surface, varying the entrainment rate (constant with pressure). To start, we use a mixing of 0.001 hPa^{-1}, as this is the constant entrainment value used in Holloway and Neelin (2009) and Sahany et al. (2012), which produced realistic updraft buoyancy profiles over tropical oceans. For the MCS case, it is plausible that a downdraft could originate at a height of 2.3 km given this rate of mixing to reach the surface with characteristics given by Fig. 4.3. (Note that there is a spread in surface values and profile characteristics, but for simplicity we use mean values.) If instead the air were coming from the level of minimum θ_e, an assumption similar to that made by many downdraft parameterizations (e.g. Zhang and McFarlane 1995; Tiedke 1989; Kain and Fritsch 1990), mixing would need be 2.5 times greater. For the isolated cells, mixing rates appear to need to be much greater in order to produce results consistent with those seen at the surface. If we start out at 0.0025 hPa^{-1}, the rate sufficient for a minimum θ_e origin for the MCSs, this only yields an origin height of 1.5 km. If instead we assume the air originates near the level of minimum θ_e, mixing would need to be about 2.5 times greater. For reference, in the Tiedke and Zhang-McFarlane schemes, downdrafts mix with environmental air at a rate nearly double the rate of mixing in updrafts, which in the Tiedke scheme is 2 x 10^{-4} m^{-1}. This is similar to 0.0025 hPa^{-1} in pressure coordinates in the lower troposphere.

To summarize, this analysis is suggestive of bounds on mixing coefficients for downdraft parameterizations. Downdrafts would need to mix less substantially through the lower troposphere for MCSs than isolated cells to draw down air that matched the observed characteristics at the

surface, and the rate of mixing needed to bring air down from the level of minimum θ_e would be 2.5 times greater for isolated cells than for the MCSs.

4.5. Vertical Velocity and Downdraft Probability

Figure 4.5 composites reflectivity (Z), vertical velocity (w) and the probability of observing downdrafts (w < 0 m s^{-1}) for the 11 cases of isolated cellular convection meeting the minimum $\Delta\theta_e$ criteria of -5°C and minimum precipitation criteria of 10 mm hr^{-1}. Time 0 is the time right before the sharpest decrease in θ_e, repeated from Fig. 4.2 in the top panel, and maximum precipitation. A 3-hr window is composited for reference, but the interval of primary interest is the 1-hr window within which the minimum $\Delta\theta_e$ and maximum precipitation are observed. To highlight the interval of interest, the 1-hr intervals leading and lagging this period are masked out.

The drop in θ_e is coincident with the passage of the isolated cell and its main updraft and precipitation-driven downdraft. Mean reflectivity exceeding 40 dbz is observed during this period, as are strong updrafts in the middle-upper troposphere. The cell then dissipates and/or moves past the site within an hour. A downdraft is observed directly below and slightly trailing the updraft core. This is the downdraft that is associated with the largest drop in surface θ_e. As is suggested in the literature, these are mainly driven by condensate loading and evaporation of precipitation and are negatively buoyant. The probability of observing negative vertical velocity (threshold < 0 m s^{-1}) within the 30 minutes of observed maxima in the absolute value of $\Delta\theta_e$ and precipitation is highest in the lower troposphere (0-2 km), consistent with precipitation-driven downdrafts observed in other studies (Sun et al., 1993; Cifelli and Rutledge, 1994).
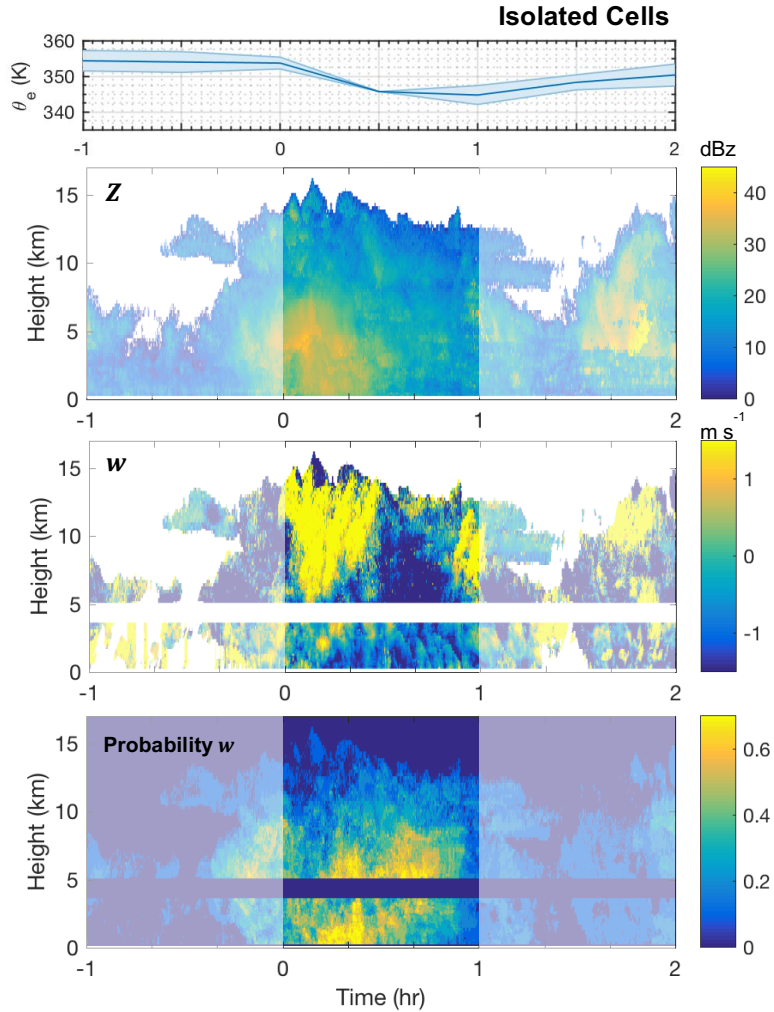
Figure 4.5: The mean reflectivity (top, dBz), mean vertical velocity (w; middle, m s^{-1}), and probability of w < 0 m s^{-1} (bottom) measured by the radar wind profiler at T3 leading and lagging the passage of isolated cells.

There is also a high probability of downdrafts in air near the freezing level (masked out in the vertical velocity retrievals, as there is large error associated with retrievals near the freezing level; Giangrande et al. 2016). It appears likely, however, that these downdrafts are discontinuous in height more often than not, as high probabilities are not observed coincidentally in the lowest levels beneath these downdrafts. These mid-upper level downdrafts are documented in previous studies of MCSs, suggesting that they form in response to the pressure field (e.g. Biggerstaff and Houze, 1991), can occur quite close to the updraft (Lily, 1960; Fritsch, 1975), and are positively

buoyant (Fovell and Ogura, 1988; Jorgensen and LeMone, 1989; Sun et al., 1993). These motions produce gravity waves in upper levels, as is discussed in Fovell et al. 1992.

Figure 6 shows the same composites for the 17 MCSs observed. They, too, have high reflectivity (mean > 40 dbz) in the 30 minutes coincident with the minimum θ_e and a defined updraft extending up to the upper troposphere. Downdrafts occurring coincident with the minimum
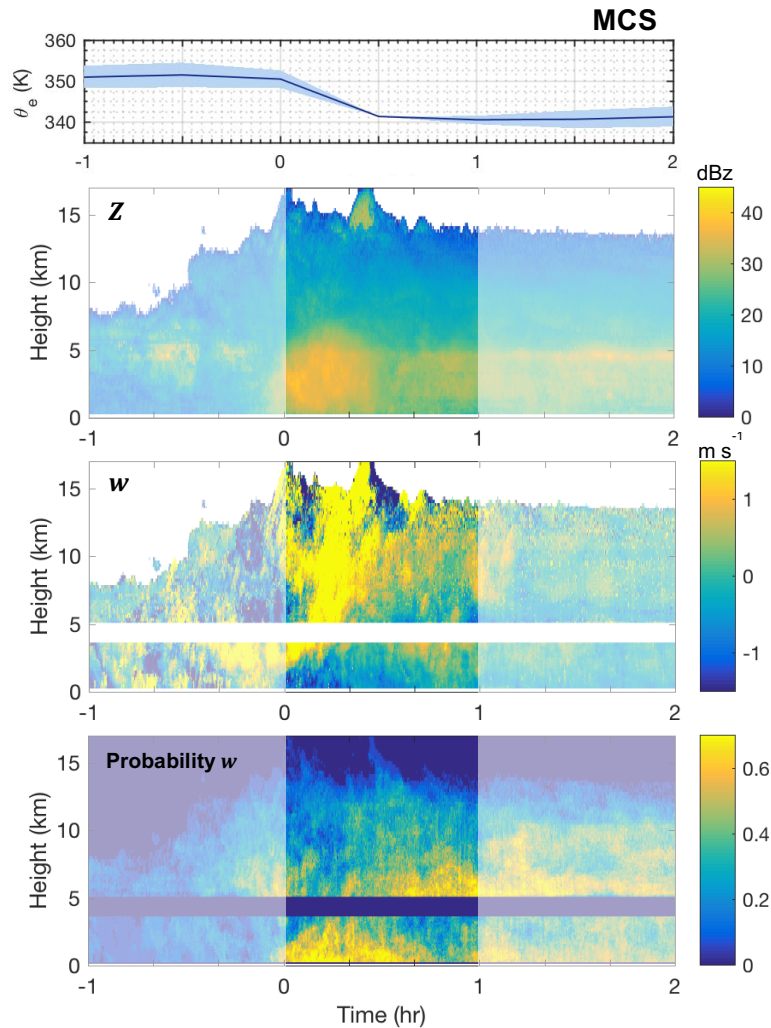
Figure 4.6: Same as Fig. 4.5, but leading and lagging the passage of MCS's.

θ_e are observed directly below the updraft signature in the mean vertical velocity panel, and the probabilities are greatest below the freezing level. There is also evidence of mesoscale downdrafts in the trailing stratiform region of the MCSs, which Miller and Betts (1976) suggest are more

97

dynamically driven than the precipitation-driven downdrafts associated with the leading-edge convection. These sustain the low θ_e air in the boundary layer for hours after the initial drop, observed in Fig. 4.3. Vertical motions in the stratiform region are weaker than in the convective region, and on average, as in Cifelli and Rutledge (1994), rarely exceed 1 m s^{-1}.

Figure 4.7 is a concise summary of the results presented in Figs. 4.5 and 4.6, showing the mean vertical velocity within the 30-min period leading maximum precipitation and during minimum $\Delta\theta_e$ for MCSs and isolated cells weighted by the frequency of data at each altitude. Previous studies using radar wind profilers have shown mean updraft and downdraft strength increases with height (May and Rajopadhyaya, 1999; Kumar et al. 2015; Giangrande et al. 2016), consistent with our results here for both isolated and organized deep convection. The corresponding mean probability is shown in the right panel. The probability of downdrafts for both isolated cells and MCSs increases nearly linearly towards the surface below the freezing level. Thus the behavior in the lowest 4 km summarizes our results from the previous two figures and suggests that downdrafts accumulate air along their descent, analogous to mixing. Probabilities, which can be interpreted loosely as convective area fractions following methods outlined in Kumar et al. (2015) and Giangrande et al. (2016), are also largest below the freezing level for downdrafts and in the 3-7 km region for updrafts. The probability and vertical velocity for both MCSs and isolated cells correspond to mass flux profiles that increase nearly linearly throughout the lower troposphere for updrafts and that decrease nearly linearly throughout the lower troposphere for downdrafts, as seen in Giangrande et al. 2016 over a broader range of convective conditions.

These results suggest that in most downdrafts, a substantial fraction of the air reaching the surface originates in the lowest 3 kilometers within both organized and unorganized convective systems. Several observational studies corroborate the evidence presented here that a majority of
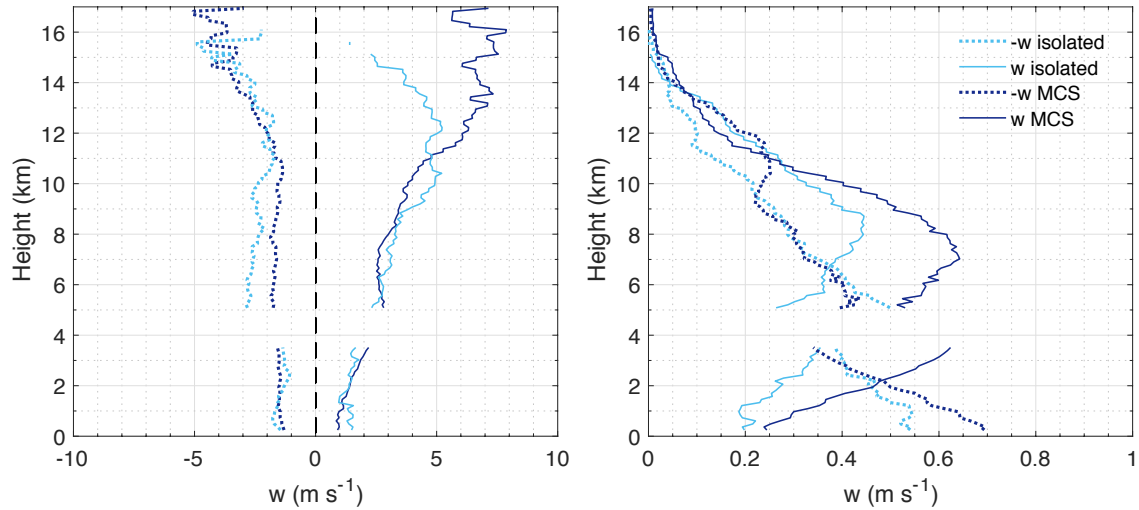
Figure 4.7: (left) Mean vertical velocity profiles for MCS's (navy) and isolated cells (light blue) weighted by the frequency of data at each altitude for downdrafts (w < 0 m s^{-1}; dashed) and updrafts (w > 0 m s^{-1}; solid). (right) Mean probability of observing updrafts or downdrafts as a function of altitude. Means are composited from data within the 30 minutes of the observed $\Delta\theta_e$ minimum and precipitation maximum.

the air reaching the surface in deep convective downdrafts originates at low-levels (Betts 1976; Barnes and Garstang 1982; Betts et al. 2002). Betts 1976 concluded that the downdraft air descends approximately only the depth of the subcloud layer (~150 mb). Betts et al. (2002) cited a range of 765-864 hPa for the first levels at which the surface θ_e values matched those of the air aloft. Additionally, there are many modeling studies that provide evidence of these low-level origins (Moncrieff and Miller, 1976; Torri and Kuang, 2016). Recently, Torri and Kuang (2016) used a Lagrangian particle dispersion model to show that precipitation-driven downdrafts originate at very low levels, citing an altitude of 1.5 km from the surface. All of these conclusions are consistent with our results here, suggesting that downdraft parameterizations substantially weight the contribution of air from the lower troposphere (e.g. with substantial mixing, modifying height of downdraft origin).

4.6.   Relating Cold Pool Thermodynamics to Precipitation

As seen previous sections, the passage of both organized and unorganized convective cells can lead to substantial decreases in θ_e resulting mainly from precipitation-driven downdrafts formed from the leading convective cells. In this section, we search for robust statistical relationships between key thermodynamic variables for potential use in improving downdraft parameterizations in GCMs. These statistics differ from those presented in Figs. 4.2-4.7, as these statistics are not conditioned on convection type and sample precipitating and non-precipitating points within the timeseries analyzed. All data available at the surface meteorological station during the GOAmazon campaign from 10 Jan 2014 – 20 Oct 2015 are included in these statistics.
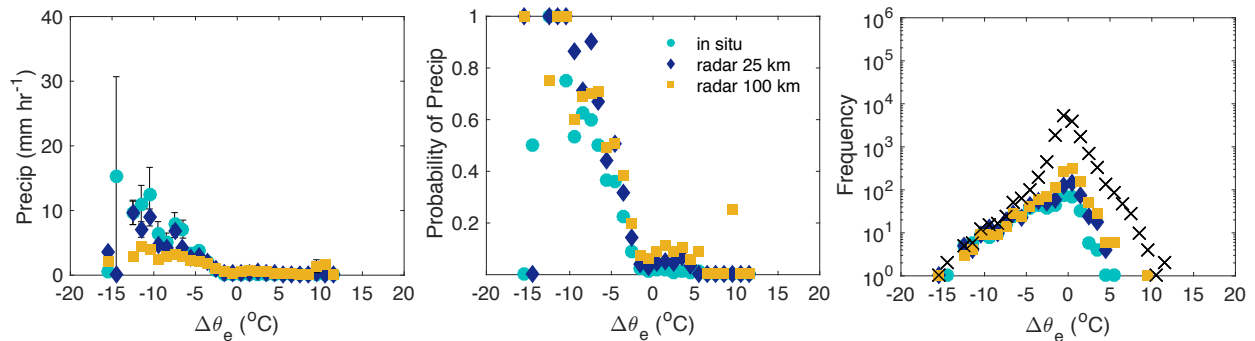
Figure 4.8: (left) Precipitation (30-min averages) conditionally averaged by coincident changes in equivalent potential temperature ($\Delta\theta_e$) at the GOAmazon site. Precipitation values corresponds to the θ_e values at the end of each differencing interval. Bins are a width of 1°. (middle) The probability of precipitation (precip > 1 mm hr^{-1}) occurring for a given $\Delta\theta_e$. (right) The frequency of occurrence of $\Delta\theta_e$ (x's) and precipitation for a given $\Delta\theta_e$ (blue dots; precip > 1 mm hr^{-1}). Precipitation derived from S-Band radar reflectivity at spatial averages over 25 km (yellow squares) and 100 km (navy diamonds) grid boxes surrounding the GOAmazon site are included for comparison to the in situ precipitation (aqua circles).

The first of these statistics conditionally averages precipitation rate by $\Delta\theta_e$ (Fig. 4.8), variants of which have been discussed in previous studies (Barnes and Garstang 1982; Wang et al. 2016). Our statistics mimic those shown in previous work relating column-integrated moisture to deep convection over tropical land (Schiro et al. 2016) and ocean (Neelin et al. 2009, Holloway and Neelin 2009). The direction of causality in the CWV-precipitation statistics, however, is the

opposite of what is presented here. CWV is thought to primarily be the cause of intense precipitation and deep convection, while here the $\Delta\theta_e$ observed is a direct result of the precipitation processes and associated downdraft. Nevertheless, examining the distribution of $\Delta\theta_e$ observed at the surface and magnitudes of the rain rates associated with the highest drops in $\Delta\theta_e$ across different regions in the tropics can place bounds on downdraft behavior. We will also conditionally average $\Delta\theta_e$ by precipitation rate, a more physically consistent direction of causality.

Fig. 4.8 shows precipitation rate binned by $\Delta\theta_e$ for in-situ precipitation and radar precipitation. Bins are 1°C in width and precipitating events are defined as having rain rates greater than 1 mm hr^{-1}. These statistics mainly suggest that any substantial decrease in θ_e at the surface occurs coincidently with heavy precipitation, which is particularly evident in the sharp increase in probability of precipitation (middle panel). The width of the distribution precipitating points is of greatest interest here. The distribution of precipitating points peaks just shy of a $\Delta\theta_e$ of 0°C, indicating that most precipitation events have low rain rates and do not occur coincidently with an appreciable drop in $\Delta\theta_e$. The frequency of precipitation drops off roughly exponentially towards lower $\Delta\theta_e$. An interesting feature is the lower bound observed in the $\Delta\theta_e$ near -15°C. Examining mean profiles in Fig. 4.5 show that, on average, this value of -15°C would be consistent with air originating from the level of minimum θ_e and descending undiluted to the surface. The frequency of observing these values suggests that air very rarely reaches the surface from these altitudes undiluted.

S-Band radar data are averaged in 25 km and 100 km grid boxes surrounding the GOAmazon site to examine the precipitation-$\Delta\theta_e$ relation with model diagnostics in mind (Fig. 4.8). Out to 25 km, the statistics are very similar to those observed using in situ precipitation. Theoretical (Romps and Jevanjee, 2015), modeling (Tompkins, 2001; Feng et al. 2015), and

observational studies (Feng et al. 2015) have all examined typical sizes of cold pools, which are on the order of 25 km in diameter for any one cell. Cold pools can combine, however, to form a larger, coherent mesoscale-sized cold pool (radius of 50 km or greater), as is commonly associated with mesoscale convective systems (Fujita 1959; Johnson and Hamilton 1988). Therefore, it is likely that our use of the in situ $\Delta\theta_e$, assuming cold pool properties are somewhat homogeneous in space, is appropriate for scales up to 25 km. Beyond this scale, it is likely that the $\Delta\theta_e$ would be smoothed by averaging, particularly for the smaller isolated cells, as would precipitation. For 100 km, the precipitation is smoothed by averaging, which would likely degrade further if information of 100 km mean surface thermodynamics were available. This suggests that comparing these statistics to those produced with model output for diagnostic purposes would yield a narrower range of $\Delta\theta_e$ and lower conditionally averaged rain rates.
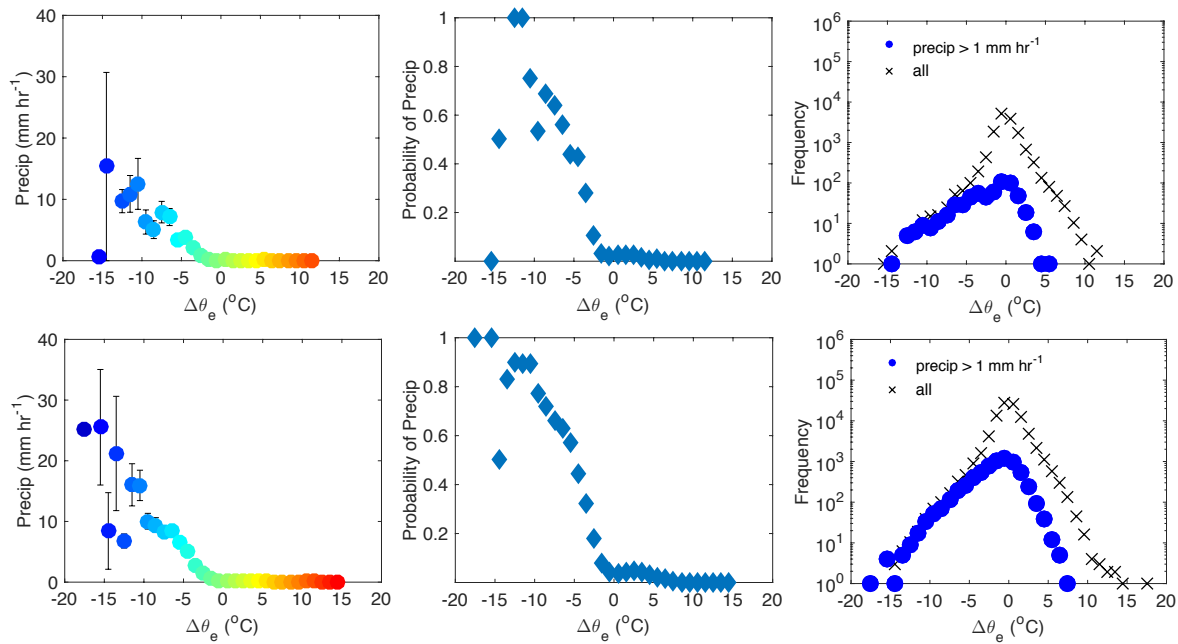
Figure 4.9: (left) Precipitation (30-min averages) conditionally averaged by coincident changes in equivalent potential temperature ($\Delta\theta_e$) at the GOAmazon site (top) and Manus Island (bottom). Precipitation values corresponds to the θ_e values at the end of each differencing interval. Bins are a width of 1°. (middle) The probability of precipitation occurring for a given $\Delta\theta_e$. (right) The frequency of occurrence of $\Delta\theta_e$ (x's) and precipitation for a given $\Delta\theta_e$ (blue dots).

Fig. 4.9 shows remarkable similarity in these statistics when comparing across regions to a DOE ARM site at Manus Island in the tropical western Pacific. As $\Delta\theta_e$ decreases, in situ precipitation rates sharply increase. The distributions, as well as the steepness and locations of the pickups, are remarkably consistent. Again, the sharpness of these curves is a result of the strongest precipitation events coinciding with the strongest decreases in θ_e, shown in the middle panels in Fig. 4.9, where the probability of observing precipitation is greatest at lower $\Delta\theta_e$.
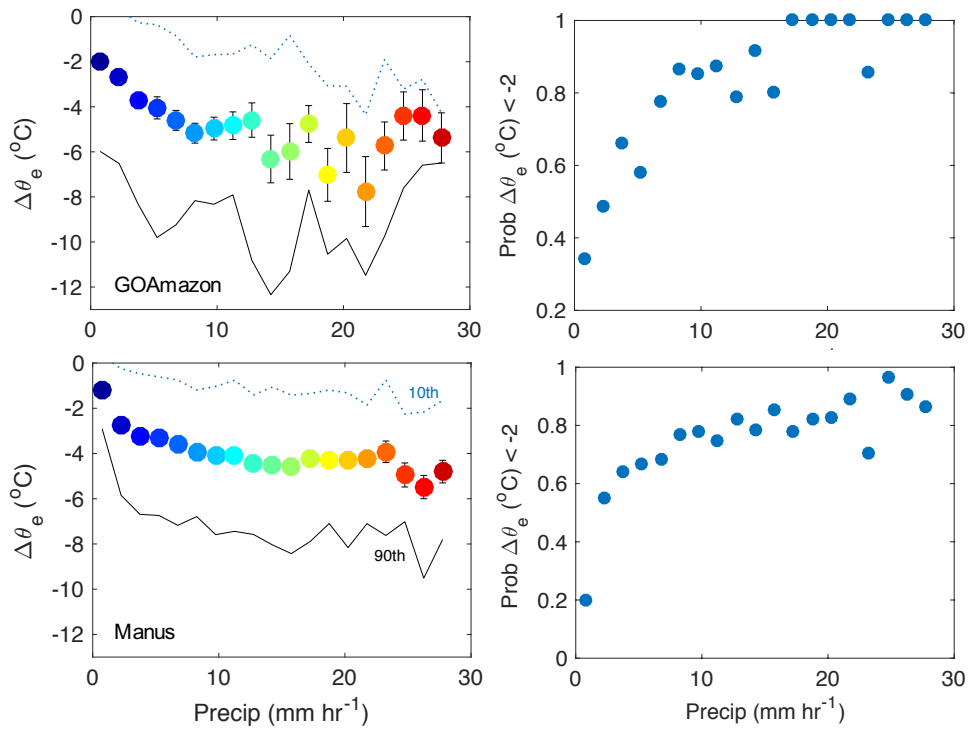
Figure 4.10: $\Delta\theta_e$ conditionally averaged by coincident precipitation (1-hr averages) at the GOAmazon site (top) and at Manus Island (bottom). Precipitation values corresponds to the θ_e values at the end of each differencing interval. Bins are a width of 1°. Error bars represent standard error. The 10th and 90th percentile values for each bin are drawn for reference.

It is then of interest to see if for a given precipitation rate we can expect a particular $\Delta\theta_e$, as this is the proper direction of causality. Fig. 4.10 conditionally averages $\Delta\theta_e$ by precipitation rate (1-hr averages). The maximum $\Delta\theta_e$ within a 3-hr window of a given precipitation rate is averaged to minimize the effects of local precipitation maxima occurring slightly before or after

the minimum in $\Delta\theta_e$. Comparing Figs. 4.9 and 4.10 shows that there can be strong precipitation events without large, corresponding decreases in surface θ_e, but that large decreases in surface θ_e are almost always associated with heavy precipitation.

Beyond about 10 mm hr^{-1} there is high probability of observing large, negative $\Delta\theta_e$ and an apparent limit in mean θ_e decreases with rain rate. This makes physical sense, as discussed above (and in Barnes and Garstang 1982), since cooling is limited by the maximum difference between the surface θ_e and the θ_e minimum aloft. The average $\Delta\theta_e$ for rain rates exceeding 10 mm hr^{-1} is about -5°C for the Amazon and -4°C for Manus Island. This statistic could be of use in constraining downdraft parameters to be consistent with surface cooling and drying observed in nature. There are still, however, open questions about scale dependence and how much cooling or drying should be observed for varying space and time scales. This result is likely applicable to GCM grid scales of 0.25° or less, as is suggested from the results in Fig. 4.9, but would be of lesser magnitude at scales more comparable to typical GCM grids (100 km or greater). Overall, if convective precipitation is present in a GCM grid, a corresponding $\Delta\theta_e$ should result within a range consistent to those observed here, subject to scale dependence.

4.7. Conclusions

Convective events sampled during the GOAmazon campaign compare downdraft characteristics between MCSs and isolated cells and examine their respective effects on surface thermodynamics. All events sampled passed directly over the GOAmazon site with minimum precipitation rates of 10 mm hr^{-1} and $\Delta\theta_e$ less than or equal to -5°C. Isolated events occurred in the afternoon hours and were characterized by average decreases of 1.1 g kg^{-1} in specific humidity, 3.9°C in temperature, and 8.0 K in θ_e, with an increase of 5.5 m s^{-1} in wind speed at the surface. More than half of the deficit in θ_e observed with the passage of the cells recovers within 2 hours,

on average, with the moisture recovering faster than temperature and a larger fraction of the total θ_e recovered. MCSs show similar decreases in temperature (3.7°C) but larger decreases in moisture (1.5 g kg^{-1}) and thus θ_e (9.1 K) at the surface. The θ_e recovers much more slowly for MCSs due to the mesoscale downdrafts and associated precipitation in their trailing stratiform regions.

Vertical velocity profiles from a radar wind profiler show that the probability of observing downdraft air during the 30 minutes of observed minimum $\Delta\theta_e$ increases with decreasing height in the lowest 4 km for both isolated cells and MCSs. This vertical structure of the downdraft probability is consistent with negative vertical velocities originating at various levels within this layer and continuing to the surface. Considering complementary thermodynamic arguments, without mixing, profiles of θ_e suggest that origin levels at average altitudes of 1.3 and 2 km for isolated cells and MCSs, respectively, would be consistent with average surface θ_e for these cases. A minimum in θ_e is observed between 3 and 7 km, on average, so for air to originate above 3 km, simple plume calculations suggest that downdrafts in MCSs would have to be mixing with environmental air at an approximate rate of 0.0025 hPa^{-1} along descent and at a rate roughly 2.5 times greater (0.006 hPa^{-1}) for isolated cells. This would imply mass entering the downdraft throughout the lowest few kilometers. Overall the vertical velocity and thermodynamic constraints are consistent in suggesting a spectrum of downdraft mass origin levels throughout the lowest few kilometers.

Robust statistical relationships between $\Delta\theta_e$ and precipitation are examined from nearly two years of data at the GOAmazon site and 15 years of data at the DOE ARM site at Manus Island in the tropical western Pacific. Conditionally averaging precipitation by $\Delta\theta_e$ is examined, similar to the statistics of precipitation conditioned on a thermodynamic quantity we consider for convective onset statistics. Here, however, the most likely direction of causality differs in that the

θ_e drop is caused by the downdraft that delivers the precipitation (as opposed to the thermodynamic profile providing convective available potential energy for an updraft). For in situ precipitation, the conditional average precipitation exhibits a sharp increase with decreasing $\Delta\theta_e$, which is similar in magnitude over land and ocean, reaching roughly 10 mm/hour at a $\Delta\theta_e$ of -10°C. For area averaged precipitation on scales typical of GCM grids, precipitation magnitude is lower for strong, negative $\Delta\theta_e$, consistent with the points with large $\Delta\theta_e$ occurring at localized downdraft locations within a larger system with smaller average precipitation. The probability distributions of $\Delta\theta_e$ (for precipitating and non-precipitating points) over land and ocean are also remarkably similar. Distributions show exponentially decreasing probability with decreasing $\Delta\theta_e$, providing additional evidence that downdraft plumes originating in the lowest levels are orders of magnitude more likely than plumes descending with little mixing from the height of minimum θ_e. Conditionally averaging $\Delta\theta_e$ by precipitation (the most likely direction of causality) suggests an average limit in $\Delta\theta_e$ of -4 to -5°C given high precipitation typical of downdraft conditions. The corresponding 90th percentile yields $\Delta\theta_e$ of roughly -10°C, consistent with results obtained from composting strong downdrafts. The robustness of these statistics over land and ocean, and to averaging in space at scales appropriate to a typical GCM resolution, suggests possible use of these statistics as model diagnostic tools and observational constraints for downdraft parameterizations.

4.S Supplemental Material

In Figs. 2 and 3 of the main text, composites were based on deep convective events meeting stringent criteria (minimum precipitation rates of 10 mm hr^{-1} and coincident with $\Delta\theta_e$ of -5°C or less, as well as complete data coverage from the radar wind profiler in the hour surrounding the precipitation maximum). Additionally, the data were averaged by convection type (isolated cell or

MCS). Here, we composite without requiring both criteria or complete data coverage from the radar wind profiler. All events with a minimum $\Delta\theta_e$ less than or equal to -5°C within a 12-hr

MCSs			Isolated Cells	
Date	Time (UTC)		Date	Time (UTC)
03/27/2014	13:30		03/11/2014	15:30
03/31/2014	07:00		03/17/2014	18:30
04/01/2014	16:00		05/20/2014	17:00
05/16/2014	18:00		07/17/2014	21:30
06/19/2014	16:00		08/15/2014	19:30
06/21/2014	02:30		09/09/2014	19:30
07/03/2014	10:30		09/13/2014	17:30
07/22/2014	20:00		09/22/2014	15:30
08/16/2014	15:00		10/06/2014	16:30
10/04/2014	15:00		01/04/2015	16:30
10/12/2014	05:00		02/03/2015	21:30
10/18/2014	15:00		03/02/2015	21:00
01/10/2015	14:00			
01/14/2015	18:00			
01/19/2015	20:00			
03/29/2015	16:30			
04/25/2015	16:00			
07/22/2015	14:00			

Table 4.S1: Dates and times (UTC) of MCS (left) and isolated cell (right) passage. Data is obtained from the timeseries of $\Delta\theta_e$ (30-min averages) and signifies the timestep before the drop in equivalent potential temperature observed at the surface.

window are averaged and shown in Fig. 4.S1 (183 events), and events with precipitation rates greater than or equal to 10 mm hr^{-1} within a 12-hr window are averaged and shown in Fig. 4.S2 (166 events). Error bars are +/- 1 standard deviation with respect to time 0. A total of 65 events meet both criteria coincidentally, and from this sample of 65, 28 are used in the main body of the text (11 isolated cases, 17 MCSs). The cases composited in Figs. 4.2 and 4.3 are listed in Table 4.S1.

The composites based on $\Delta\theta_e$ (Fig. 4.S1) show marginal differences in the thermodynamic variables compared to the composite based on precipitation (Fig. 4.S2): lower relative humidity, higher temperature, and higher CWV. It is likely that this results from a daytime bias for the composites in Fig. 4.S1. They do, however, differ in their respective mean rain rates and $\Delta\theta_e$ at time 0, confirming that not all precipitation produces $\Delta\theta_e$ of -5°C or greater and vice versa.
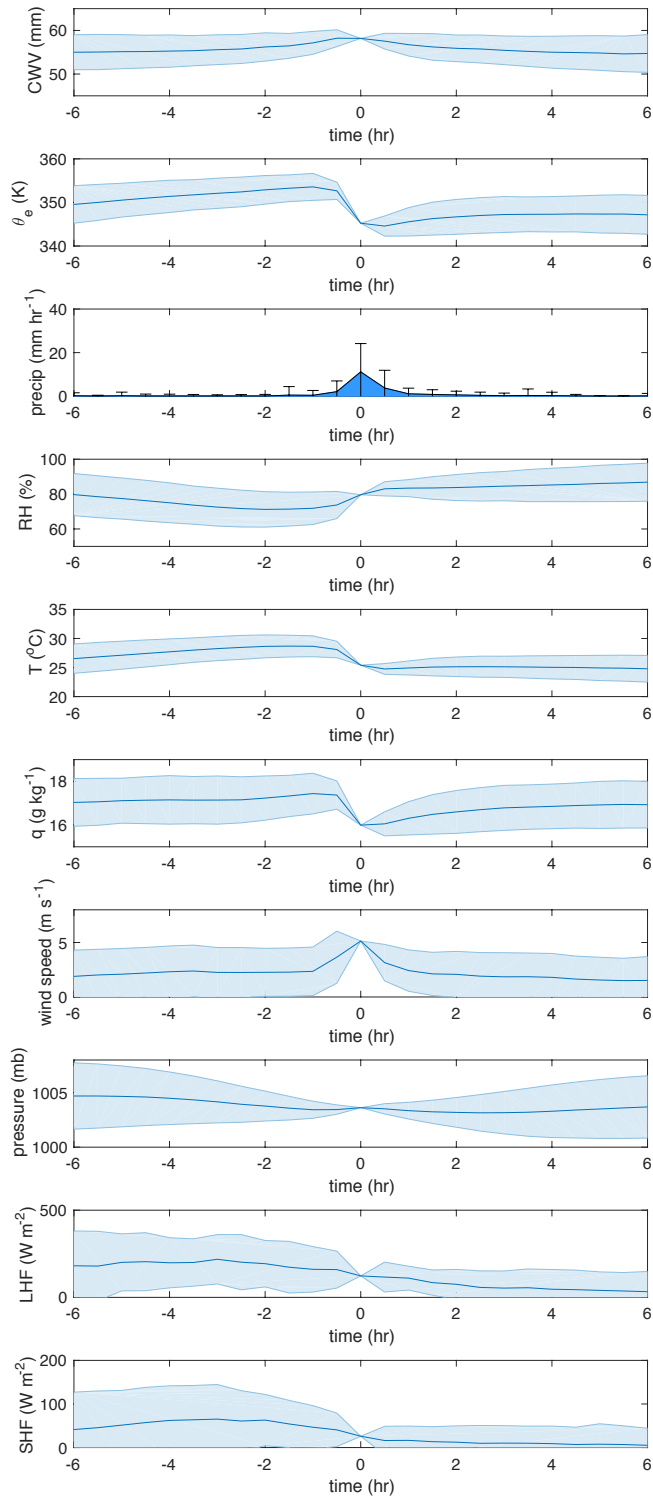
Figure 4.S1: Composites of meteorological variables from the AOSMET station at site T3 (GOAmazon) 6 hours leading and 6 hours lagging drops in equivalent potential temperature less than or equal to -5 K. 183 events total are sampled from 10 Jan 2014 – 20 Oct 2015 contribute to the composite. Error bars are +/- 1 standard deviation with respect to time 0.
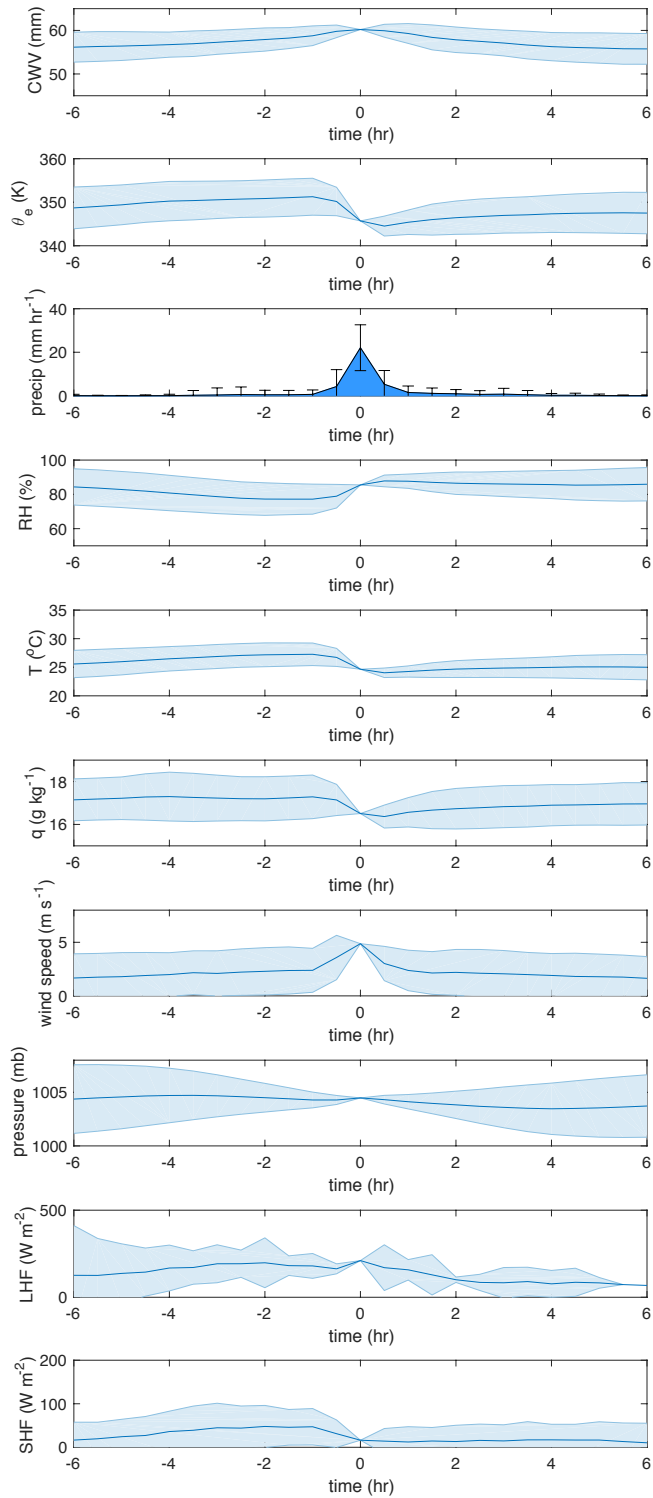
Figure 4.S2: Same as Fig. 4.S1, except compositing based on precipitation rates greater than 10 mm hr^{-1} instead of $\Delta\theta_e$. 166 events are averaged, 65 of which are coincident with drops in $\Delta\theta_e$ less than or equal to -5 K and thus included in the composites in Fig. 4.S1.
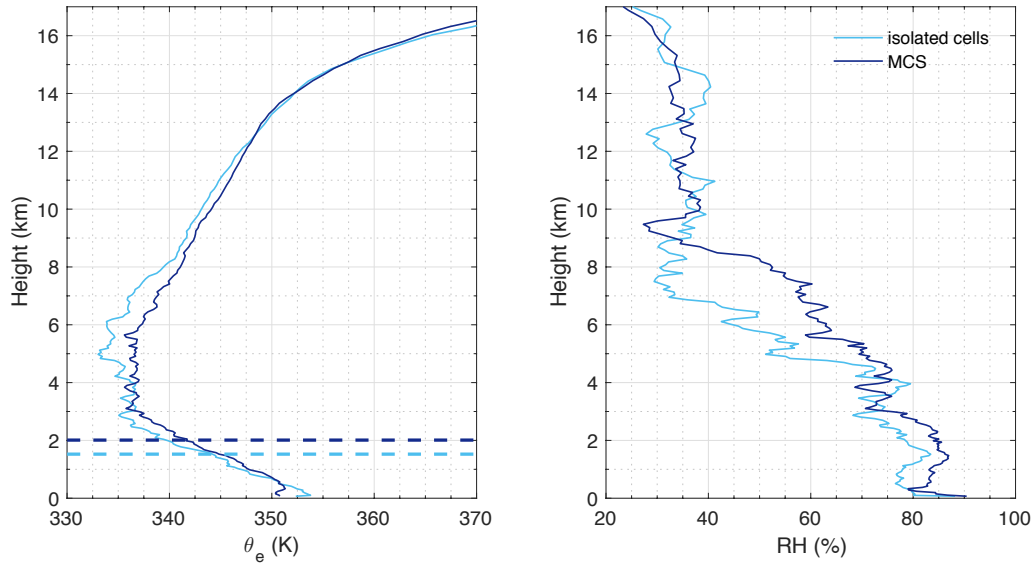
Figure 4.S3: Mean thermodynamic profiles (equivalent potential temperature, left; relative humidity, right) within 6 hours leading the passage of a deep convective event. Dashed lines at 1.3 km and 2.0 km (with an average pressure of 860 mb and 800 mb, respectively) indicate the first altitude at which the minimum surface θ_e matches the θ_e in the vertical profile for isolated cells (blue) and MCS's (navy), respectively.

Lastly, mean profiles of θ_e and relative humidity are shown in Fig. 4.S3 for the isolated and MCS cases leading the passage of the convective systems by up to 6 hours. The MCS cases have higher RH and θ_e throughout the column than the isolated cases, except for in the boundary layer, consistent with the higher CWV observed in the composites of Fig. 4.3 compared to Fig. 4.2.

BIBLIOGRAPHY

Adams, D. K., R. M. S. Fernandes, and J. M. F. Maia, 2011: GNSS precipitable water vapor from an Amazonian rain forest flux tower. *Journal of Atmospheric and Oceanic Technol*ogy, **28,** 1192–1198.

Adams, D. K., S. I. Gutman, K. L. Holub, and D. S. Pereira, 2013: GNSS observations of deep convective time scales in the Amazon. *Geophysical Research Letters*, **40**, 2818-2823.

Adams, D. K., R. M. S. Fernandes, K. L. Holub, S. I. Gutman, H. M. J. Barbosa, L. A.T. Machado, A. J. P. Calheiros, R. A. Bennett, E. R. Kursinski, L. F. Sapucci, C. DeMets, G. F. B. Chagas, A. Arellano, N. Filizola, A. A. Amorim Rocha, R. Araújo Silva, L. M. F. Assunção, G. G. Cirino, T. Pauliquevis, Bruno T. T. Portela, A. Sá, J. M. de Sousa, and L. M. S. Tanaka, 2015: The Amazon Dense GNSS Meteorological Network: A New Approach for Examining Water Vapor and Deep Convection Interactions in the Tropics. *Bulletin of the American Meteorological Society,* **96**, 2151–2165.

Ahmed, F., and C. Schumacher, 2015: Convective and stratiform components of the precipitation-moisture relationship. *Geophysical Research Letters*, **10**, 453-462.

Ahmed, F., and C. Schumacher, 2017: Geographical differences in the tropical precipitation-moisture relationship and rain intensity onset. *Geophysical Research Letters*, **44**, 1114-1122.

Andreae, M. O., D. Rosenfeld, P. Artaxo, A. A., Costa, G. P., Frank, K. M. Longo, and M. A. F. Silva-Dias, 2004: Smoking rain clouds over the Amazon. *Science,* **303**, 1337–1342.

Austin, J. M., 1948: A note on cumulus growth in a nonsaturated environment. *Journal of Meteorology*, **5**, 103–107.

Bacmeister, J. T., and G. L. Stephens, 2011: Spatial statistics of likely convective clouds in CloudSat data. *Journal of Geophysical Research: Atmospheres*, **116**, D04104 1-21.

Barnes, G. M. and M. Garstang, 1982: Subcloud Layer Energetics of Precipitating Convection. *Monthly Weather Review*, **110**, 102-117.

Bechtold, P., J. Chaboureau, A. Beljaars, A. K. Betts, M. Kohler, M. J. Miller, & J. Redelsperger, 2004: The simulation of the diurnal cycle of convective precipitation over land in a global model. *Quarterly Journal of the Royal Meteorological Society*, **130**, 3119–3137.

Bechtold, P., M. Kohler, T. Jung, F. Doblas-Reyes, M. Leutbecher, M. J. Rodwell, F. Vitart and G. Balsamo, 2008: Advances in simulating atmospheric variability with the ECMWF model: From synoptic to decadal time-scales. *Quarterly Journal of the Royal Meteorological Society*, **134**, 1337–1351.

Bechtold, P., N. Semane, P. Lopez, J. Chaboureau, A. Beljaars, and N. Bormann, 2014: Representing equilibrium and nonequilibrium convection in large-scale models. *Journal of the Atmospheric Sciences,* **71**, 734-753.

Bergemann, M., and C. Jakob, 2016: How important is tropospheric humidity for coastal rainfall in the tropics? *Geophysical Research Letters,* **43***,* 5860-5868.

Bernstein, D. N., and J. D. Neelin, 2016: Identifying sensitive ranges in global warming precipitation change dependence on convective parameters. *Geophysical Research Letters*, **43**, 5841-5850.

Benedict, J. J., and D. A. Randall, 2007: Observed characteristics of the MJO relative to maximum rainfall. *Journal of the Atmospheric Sciences,* **64**, 2332–2354.

Betts, A., 1973: Non-precipitating cumulus convection and its parameterization. *Quarterly Journal of the Royal Meteorological Society*, **99**, 178-196.

Betts, A. K., 1976: The thermodynamic transformation of the tropical subcloud layer by precipitation and downdrafts. *Journal of the Atmospheric Sciences*, **33**, 1008-1020.

Betts, A. K., and M. F. Silva Dias, 1979: Unsaturated downdraft thermodynamics in cumulonimbus. *Journal of the Atmospheric Sciences*, **36**(6), 1061-1071.

Betts, A. K., L. V. Gatti, A. M. Cordova, M. A. Silva Dias, and J. D Fuentes, 2002: Transport of ozone to the surface by convective downdrafts at night. *Journal of Geophysical Research: Atmospheres*, **107**(D20).

Betts, A. K., and C. Jakob, 2002: Study of diurnal cycle of convective precipitation over Amazonia using a single column model, *Journal of Geophysical Research.,* **107**, 4732.

Bevis, M., S. Businger, T. A. Herring, C. Rocken, R. A. Anthes, and R. H. Ware, 1992: GPS meteorology: Remote sensing of atmospheric water vapor using the Global Positioning System. *Journal of Geophysical Research: Atmospheres,* **97**, 15787-15801.

Biasutti, M., A. H. Sobel, and Y. Kushnir, 2006: GCM precipitation biases in the Tropical Atlantic. *Journal of Climate*, **19**, 935–958.

Biggerstaff, M. I., and R. A. Houze Jr, 1991: Kinematic and precipitation structure of the 10–11 June 1985 squall line. *Monthly Weather Review*, **119**, 3034-3065.

Boing, S. J., H J. J. Jonker, A. P. Siebesma, and W. W. Grabowski, 2012: Influence of the Subcloud Layer on the Development of a Deep Convective Ensemble. *Journal of the Atmospheric Sciences,* **69**, 2682-2698.

Bolton, D., 1980: The computation of equivalent potential temperature. *Monthly Weather Review*, **108**, 1046-1053.

Bretherton, C. S., M. E. Peters, and L. E. Back, 2004: Relationships between water vapor path and precipitation over the tropical oceans. *Journal of Climate*, **17**, 1517–1528.

Brown, R. G., and C. Zhang, 1997: Variability of midtropospheric moisture and its effect on cloud-top height distribution during TOGA COARE. *Journal of the Atmospheric Sciences,* **54**, 2760–2774.

Byers, H. R. and R. R. Braham, 1949: The thunderstorm: report of the Thunderstorm Project. *US Government Printing Office.*

Chaboureau, J. P., F. Guichard, J. L. Redelsperger, and J. P. Lafore, 2004: The role of stability and moisture in the diurnal cycle of convection over land. *Quarterly Journal of the Royal Meteorological Society*, **130**, 3105–3117.

Cifelli, R., and S. A. Rutledge, 1994: Vertical motion structure in maritime continent mesoscale convective systems: Results from a 50-MHz profiler. *Journal of the Atmospheric Sciences*, **51**, 2631-2652.

Collins, M., R. Knutti, J. Arblaster, J.-L. Dufresne, T. Fichefet, P. Friedlingstein, X. Gao, W.J. Gutowski, T. Johns, G. Krinner, M. Shongwe, C. Tebaldi, A.J. Weaver and M. Wehner, 2013: Long-term Climate Change: Projections, Commitments and Irreversibility. In: Climate Change 2013: The Physical Science Basis. Contribution of Working Group I to the Fifth Assessment Report of the Intergovernmental Panel on Climate Change [Stocker, T.F., D. Qin, G.-K. Plattner, M. Tignor, S.K. Allen, J. Boschung, A. Nauels, Y. Xia, V. Bex and P.M. Midgley (eds.)]. Cambridge University Press, Cambridge, United Kingdom and New York, NY, USA, pp. 1029–1136.

Collow, A.B., M.A. Miller, and L. Trabachino, 2016: Cloudiness over the Amazon Rainforest: Meteorology and thermodynamics. *Journal of Geophysical Research: Atmospheres,* **121**, 7990-8005.

Dai, A., and K. E. Trenberth, 2004: The Diurnal Cycle and Its Depiction in the Community Climate System Model. *Journal of Climate,* **17**, 930–951.

Dai, A., 2006: Precipitation characteristics in eighteen coupled climate models. *Journal of Climate*, **19**, 4605–4630.

de Rooy W. C., P. Bechtold, K. Frohlich, C. Hohenegger, H. Jonker, D. Mironov, A. P. Siebesma, J. Teixeira, and J.-I. Yano, 2013: Entrainment and detrainment in cumulus convection: an overview. *Quarterly Journal of the Royal Meteorological Society*, **139**, 1-19.

Del Genio, A.D., and J. Wu, 2010: The Role of Entrainment in the Diurnal Cycle of Continental Convection. *Journal of Climate*, **23**, 2722–2738.

Del Genio A.D., Y. Chen, D. Kim, and M.-S. Yao, 2011: The MJO transition from shallow to deep convection in CloudSat/CALIPSO data and GISS GCM simulations. *Journal of Climate*, **25**, 3755-3770.

Derbyshire, S. H., I. Beau, P. Bechtold, J.-Y. Gandpeix, J.-M. Piriou, J.-L. Redelsperger, and P. Soares (2004), Sensitivity of moist convection to environmental humidity. *Quarterly Journal of the Royal Meteorological Society,* **130**, 3055 – 3079.

Douville, H., D. Salas-Melia, and S. Tyteca, 2006: On the tropical origin of uncertainties in the global land precipitation response to global warming. *Climate Dynamics,* **26**, 367-385.

Emanuel, K. A., 1994: Atmospheric Convection. 1st ed. Oxford University Press, 580 pp.

Engerer, N. A., D. J. Stensrud, and M. C. Coniglio, 2008: Surface characteristics of observed cold pools. *Monthly Weather Review*, **136**, 4839-4849.

Feng, Z., S. Hagos, A. K. Rowe, C. D. Burleyson, M. N. Martini, and S. P. Szoeke, 2015: Mechanisms of convective cloud organization by cold pools over tropical warm ocean

during the AMIE/DYNAMO field campaign. *Journal of Advances in Modeling Earth Systems*, **7**, 357-381.

Fovell, R. G. and Ogura, Y., 1988: Numerical simulation of a midlatitude squall line in two dimensions. *Journal of the Atmospheric Sciences*, **45**, 3846-3879.

Fovell, R., D. Durran, and J. R. Holton, 1992: Numerical simulations of convectively generated stratospheric gravity waves. *Journal of the Atmospheric Sciences*, **49**, 1427-1442.

Fovell, R. G. and P. H. Tan, 1998: The temporal behavior of numerically simulated multicell-type storms. Part II: The convective cell life cycle and cell regeneration. *Monthly Weather Review*, **126**, 551-577.

Fujita, T., 1959: Precipitation and cold air production in mesoscale thunderstorm systems. *Journal of Meteorology*, **16**, 454-466.

Fujita, T., 1963: Analytical mesometeorology: A review. In *Severe local storms* (pp. 77-128). American Meteorological Society.

Gerken, T., D. Wei, R. J. Chase, J. D. Fuentes, C. Schumacher, L. Machado, R. V. Andreoli et al., 2016: Downward transport of ozone rich air and implications for atmospheric chemistry in the Amazon rainforest. *Atmospheric Environment,* **124**, 64-76.

Giangrande, S. E., T. Toto, M. P. Jensen, M. J. Bartholomew, Z. Feng, A. Protat, C. R. Williams, C. Schumacher, and L. Machado, 2016: Convective cloud vertical velocity and mass-flux characteristics from radar wind profiler observations during GoAmazon2014/5. *Journal of Geophysical Research: Atmospheres*, **121**(21).

Goff, R., 1976: Vertical structure of thunderstorm outflows. *Monthly Weather Review*, **104**, 1429-1440.

Grabowski, W. W., 2003: MJO-like coherent structures: Sensitivity simulations using the cloud-resolving convection parameterization (CRCP). *Journal of the Atmospheric Sciences,* **60**, 847–864.

Grabowski, W. W. and M. W. Moncrieff, 2004: Moisture–convection feedback in the tropics. *Quarterly Journal of the Royal Meteorological Society,* **130**, 3081–3104.

Grabowski, W. W., 2006: Impact of explicit atmosphere–ocean coupling on MJO-like coherent structures in idealized aquaplanet simulations. *Journal of the Atmospheric Sciences,* **63**, 2289–2306.

Grabowski, W. W., and H. Morrison, 2016: Untangling microphysical impacts on deep convection applying a novel modeling methodology. Part 2: Double-moment microphysics. *Journal of the Atmospheric Sciences,* **72**, 2446-2464.

Guichard, F., J. C. Petch, J.-L. Redelsperger P. Bechtold, J.-P. Chaboureau, S. Cheinet, W. Grabowski, H. Grenier, C. G. Jones, M. Köhler, et al., 2004: Modelling the diurnal cycle of deep precipitating convection over land with cloud-resolving models and single column models, *Quarterly Journal of the Royal Meteorological Society, 130*, 3139 – 3172.

Hagos, S., Z. Feng, K. Landu, C. N. Long, 2014: Advection, moistening, and shallow-to-deep convection transitions during the initiation and propagation of Madden-Julian Oscillation. *Journal of Advances in Modeling Earth Systems*, **6**, 938-949.

Hannah, W. M. and E. D. Maloney, 2011: The Role of Moisture–Convection Feedbacks in Simulating the Madden–Julian Oscillation. *Journal of Climate,* **24**, 2754–2770.

Hirota, N., and Y. N. Takayabu, 2013: Reproducibility of precipitation distribution over the tropical oceans in CMIP5 multi-climate models compared to CMIP3. *Climate Dynamics,* **41**, 2909–2920.

Hirota, H., Y. N. Takayabu, M. Watanabe, M. Kimoto, and M. Chikira, 2014: Role of Convective Entrainment in Spatial Distributions of and Temporal Variations in Precipitation over Tropical Oceans. *Journal of Climate,* **27**, 8707–8723.

Hohenegger, C. and C. S. Bretherton, 2011: Simulating deep convection with a shallow convection scheme. *Atmospheric Chemistry and Physics*, **11**(20), 10389-10406.

Hohenegger, C., and B. Stevens, 2013: Preconditioning Deep Convection with Cumulus Congestus. *Journal of the Atmospheric Sciences,* **70**, 448–464.

Holloway, C. E., and J. D. Neelin, 2009: Moisture Vertical Structure, Column Water Vapor, and Tropical Deep Convection. *Journal of the Atmospheric Sciences,* **66**, 1665–1683.

Holloway, C. E., and J. D. Neelin, 2010: Temporal Relations of Column Water Vapor and Tropical Precipitation. *Journal of the Atmospheric Sciences,* **67**, 1091–1105.

Holloway, C. E., S. J. Woolnough, and G. M. S. Lister, 2013: The Effects of Explicit versus Parameterized Convection on the MJO in a Large-Domain High-Resolution Tropical Case Study. Part I: Characterization of Large-Scale Organization and Propagation. *Journal of the Atmospheric Sciences,* **70**, 1342–1369.

Houze, R. A., B. F. Smull, and P. Dodge, 1990: Mesoscale organization of springtime rainstorms in Oklahoma. *Monthly Weather Review*, **118**, 613-654.

Houze, R.A., 1993: *Cloud Dynamics*, 573 pp., Academic, San Diego, Calif.

Houze, R. A., 2004: Mesoscale convective systems. *Reviews of Geophysics*, **42**(4).

Huffman, G.J., R. F. Adler, D. T. Bolvin, G. Gu, E. J. Nelkin, K. P. Bowman, Y. Hong, E. F. Stocker, and D. B. Wolff, 2007: The TRMM Multisatellite Precipitation Analysis (TMPA): Quasi-Global, Multiyear, Combined-Sensor Precipitation Estimates at Fine Scales. *Journal of Hydrometeorology*, **8**, 38-55.

Jensen, M. P., and A. D. Del Genio, 2006: Factors Limiting Convective Cloud-Top Height at the ARM Nauru Island Climate Research Facility. *Journal of Climate,* **19**, 2105-2117.

Jiang, X., D. E. Waliser, W. S. Olson, W. K. Tao, T. S. L'Ecuyer, , K. F. Li, Y. L. Yung, S. Shige, S. Lang, and Y. N. Takayabu, 2011: Vertical diabatic heating structure of the MJO: Intercomparison between recent reanalyses and TRMM estimates. *Monthly Weather Review*, **139**, 3208-3223.

Johnson, R. H., and P. J. Hamilton, 1988: The relationship of surface pressure features to the precipitation and airflow structure of an intense midlatitude squall line. *Monthly Weather Review*, **116**, 1444-1473.

Johnson, R. H., T. M. Rickenbach, S. A. Rutledge, P. E. Ciesielski, and W. H. Schubert, 1999: Trimodal characteristics of tropical convection. *Journal of Climate,* **12**, 2397–2418.

Jorgensen, D. P. and M. A. LeMone, 1989: Vertical velocity characteristics of oceanic convection. *Journal of the Atmospheric Sciences*, **46**, 621-640.

Kain, J. S., and J. M. Fritsch, 1990: A one-dimensional entraining/detraining plume model and its application in convective parameterization. *Journal of the Atmospheric Sciences*, **47**, 2784-2802.

Kamburova, P. L. and F. H. Ludlam, 1966: Rainfall evaporation in thunderstorm downdraughts. *Quarterly Journal of the Royal Meteorological Society*, **92**, 510-518.

Kemball-Cook, S. R., and B. C. Weare, 2001: The onset of convection in the Madden-Julian oscillation. *Journal of Climate,* **14**, 780–793.

Khain, A., D. Rosenfeld, and A. Pokrovsky, 2005: Aerosol impact on the dynamics and microphysics of deep convective clouds. *Quarterly Journal of the Royal Meteorological Society*, **131**, 2639–2663.

Khain, A. P., K. D. Beheng, A. Heymsfield, A. Korolev, S. O. Krichak, Z. Levin, M. Pinsky, V. Phillips, T. Prabhakaran, A. Teller, S. C. van den Heever, and J.-I. Yano, 2015: Representation of microphysical processes in cloud-resolving models: Spectral (bin) microphysics versus bulk parameterization. *Rev. Geophys.,* **53**, 247–322.

Khairoutdinov, M., and D. Randall, 2006: High-resolution simulation of shallow-to-deep convection transition over land, *Journal of the Atmospheric Sciences,* **63**, 3421 – 3436.

Khairoutdinov, M. F., S. K. Krueger, C. H. Moeng, P. A. Bogenschutz and D. A. Randall, 2009: Large-eddy simulation of maritime deep tropical convection. *Journal of Advances in Modeling Earth Systems*, **1**(4).

Kim, D., A. H. Sobel, A. D. Del Genio, Y. Chen, S. J. Camargo, M.-S. Yao, M. Kelley, and L. Nazarenko, 2012: The Tropical Subseasonal Variability Simulated in the NASA GISS General Circulation Model. *Journal of Climate*, **25**, 4641–4659.

Kim, D., P. Xavier, E. Maloney, M. Wheeler, D. Waliser, K. Sperber, H. Hendon, C. Zhang, R. Neale, Y.-T. Hwang, H. Liu, 2014: Process-Oriented MJO Simulation Diagnostic: Moisture Sensitivity of Simulated Convection. *Journal of Climate,* **27**, 5379-5395.

Klocke, D., R. Pincus, and J. Quaas, 2011: On constraining estimates of climate sensitivity with present-day observations through model weighting. *Journal of Climate*, **24**, 6092-6099.

Knievel, J. C., D. A. Ahijevych, and K. W. Manning, 2004: Using temporal modes of rainfall to evaluate the performance of a numerical weather prediction model. *Monthly Weather Review*, **132**, 2995-3009.

Knight, C. G., and Coauthors, 2007: Association of parameter, software, and hardware variation with large-scale behavior across 57,000 climate models. *Proceedings of the National Academy of Sciences USA*, **104**, 12 259–12 264,

Knupp, K. R. and W. R. Cotton, 1985: Convective cloud downdraft structure: An interpretive survey. *Reviews of Geophysics*, **23**, 183-215.

Kuang, Z., and C. S. Bretherton 2006: A mass-flux scheme view of a high-resolution simulation of a transition from shallow to deep convection, *Journal of the Atmospheric Sciences*, **63**, 1895 – 1909.

Kumar, V. V., C. Jakob, A. Protat, P. T. May, and L. Davies, 2013: The four cumulus cloud modes and their progression during rainfall events: AC-band polarimetric radar perspective. *Journal of Geophysical Research: Atmospheres,* **118**, 8375–8389.

Kumar, V. V., C. Jakob, A. Protat, C. R. Williams, and P. T. May, 2015: Mass-flux characteristics of tropical cumulus clouds from wind profiler observations at Darwin, Australia. *Journal of the Atmospheric Sciences*, **72**, 1837–1855.

Kuo, Y. H., J. D. Neelin, and C. R. Mechoso, 2017: Tropical Convective Transition Statistics and Causality in the Water Vapor–Precipitation Relation. *Journal of the Atmospheric Sciences*, **74**, 915-931.

Kummerow, C., Y. Hong, W. S. Olson, S. Yang, R. F. Adler, J. McCollum, R. Ferraro, G. Petty, Dong-Bin Shin, and T. T. Wilheit, 2001: The evolution of the Goddard Profiling Algorithm (GPROF) for rainfall estimation from passive microwave sensors. *Journal of Applied Meteorology,* **40**, 1801-1820.

Lee, M. I., S. D. Schubert, M. J. Suarez, I. M. Held, A. Kumar, T. L. Bell et al. 2007: Sensitivity to horizontal resolution in the AGCM simulations of warm season diurnal cycle of precipitation over the United States and northern Mexico. *Journal of Climate*, **20**, 1862-1881.

LeMone, M. A., and E. J. Zipser (1980), Cumulonimbus vertical velocity events in GATE. Part I: Diameter, intensity and mass flux. *Journal of the Atmospheric Sciences,* **37**, 2444–2457.

LeMone, M. A., E. J. Zipser, and S. B. Trier, 1998: The Role of Environmental Shear and Thermodynamic Conditions in Determining the Structure and Evolution of Mesoscale Convective Systems during TOGA COARE. *Journal of the Atmospheric Sciences,* **55**, 3493–3518.

Li, Y., E. J. Zipser, S. K. Krueger, and M. A. Zulauf, 2008: Cloud-resolving modeling of deep convection during KWAJEX. Part I: Comparison to TRMM satellite and ground-based radar observations. *Monthly Weather Review*, **136**, 2699–2712.

Li, Z., P. Zuidema, and P. Zhu, 2014: Simulated convective invigoration processes at trade wind cumulus cold pool boundaries. *Journal of the Atmospheric Sciences*, **71**, 2823-2841.

Lin, J. L., K. M. Weickman, G. N. Kiladis, B. E. Mapes, S. D. Schubert, M. J. Suarez, and coauthors, 2008: Subseasonal variability associated with Asian summer monsoon simulated by 14 IPCC AR4 coupled GCMs. *Journal of Climate*, **21**, 4541-4567.

Liljegren, JC, 1999: Automatic self-calibration of ARM microwave radiometers. *Microwave Radiometry and Remote Sensing of the Earth's Surface and Atmosphere*. Ed. P. Pampaloni and S. Paloscia, pp. 433-443.

Lima, M. A., and J. W. Wilson, 2008: Convective storm initiation in a moist tropical environment. *Monthly Weather Review*, **136**, 1847-1864.

Lintner, B. R., and J. D. Neelin, 2007: A prototype for convective margin shifts. *Geophysical Research Letters,* **34**, L05812.

Lintner, B. R., and J. D. Neelin, 2008: Eastern margin variability of the South Pacific convergence zone. *Geophysical Research Letters,* **35**, L16701.

Lintner, B.R., and J.D. Neelin, 2009: Soil moisture impacts on convective margins. *Journal of Hydrometeorology*, **10**, 1026—1039.

Lintner, B.R., and J. D. Neelin, 2010: Tropical South America–Atlantic Sector Convective Margins and Their Relationship to Low-Level Inflow. *Journal of Climate,* **23**, 10, 2671-2685.

Lintner, B. R., C. E. Holloway, and J. D. Neelin, 2011: Column Water Vapor Statistics and Their Relationship to Deep Convection, Vertical and Horizontal Circulation, and Moisture Structure at Nauru. *Journal of Climate*, **24**, 5454-5466.

Luo, Z. J., G. Y. Liu, and G. L. Stephens, 2010: Use of A-train data to estimate convective buoyancy and entrainment. *Geophysical Research Letters,* **37**, L09804.

Ma, H-Y., X. Ji, J. D. Neelin, and C. R. Mechoso, 2011: Mechanisms for Precipitation Variability of the Eastern Brazil/SACZ Convective Margin, *Journal of Climate*, **24**, 13, 3445-3456.

Malkus, J. S., 1954: Some results of a trade-cumulus cloud investigation. *Journal of Meteorology*, **11**, 220–237.

Maloney, E. D. and D. L. Hartmann, 2001: The sensitivity of intraseasonal variability in the NCAR CCM3 to changes in convective parameterization. *Journal of Climate*, **14**, 2015-2034.

Mapes, B., S. Tulich, J. Lin, and P. Zuidema, 2006: The mesoscale convection life cycle: Building block or prototype for largescale tropical waves? *Dynamics of Atmospheres and Oceans,* **42**, 3–29.

Mapes, B., and R. Neale, 2011: Parameterizing convective organization to escape the entrainment dilemma. *Journal of Advances in Modeling Earth Systems*, **3**.

Martin, S. T., P. Artaxo, L. A. T. Machado, A. O. Manzi, R. A. F. Souza, C. Schumacher, J. Wang, M. O. Andreae, H. M. J. Barbosa, J. Fan, G. Fisch, A. H. Goldstein, A. Guenther, J. L.

Jimenez, U. Pöschl, M. A. Silva Dias, J. N. Smith, and M. Wendisch, 2016: Introduction: Observations and Modeling of the Green Ocean Amazon (GoAmazon2014/5). *Atmospheric Chemistry and Physics,* **16**, 4785-4797.

Masunaga, H., 2013: A satellite study of tropical moist convection and environmental variability: A moisture and thermal budget analysis. *Journal of the Atmospheric Sciences,* **70**, 2443–2466.

May, P. T. and D. K. Rajopadhyaya, 1998: Vertical Velocity Characteristics of Deep Convection over Darwin, Australia. *Monthly Weather Review*, **127**, 1056-1071.

Moncrieff, M. W. and M. J. Miller, 1976: The dynamics and simulation of tropical cumulonimbus and squall lines. *Quarterly Journal of the Royal Meteorological Society*, **102**, 373-394.

Morris, V.R., 2006: Microwave radiometer (MWR) handbook. *ARM-TR016.*

Murphy, J. M., D. M. H. Sexton, D. N. Barnett, G. S. Jones, M. J. Webb, M. Collins, and D. A.Stainforth, 2004: Quantification of modelling uncertainties in a large ensemble of climate change simulations. *Nature*, **430**, 768–772.

Neale, R. B., J. H. Richter, and M. Jochum, 2008: The impact of convection on ENSO: From a delayed oscillator to a series of events. *Journal of Climate*, **21**, 5904-5924.

Neelin, J. D., and I. M. Held, 1987: Modeling tropical convergence based on the moist static energy budget. *Monthly Weather Review,* **115**, 3-12.

Neelin, J.D., O. Peters, and K. Hales, 2009: The Transition to Strong Convection. *Journal of the Atmospheric Sciences,* **66**, 2367–2384.

Neelin, J.D., B.R. Lintner, B. Tian, Q.B. Li, L. Zhang, P.K. Patra, M.T. Chahine, and S.N. Stechmann, 2010: Long tails in deep columns of natural and anthropogenic tracers. *Geophysical Research Letters,* **37**, L05804.

Nesbitt, S. W., and E. J. Zipser, 2003: The diurnal cycle of rainfall and convective intensity according to three years of TRMM measurements. *Journal of Climate*, **16**, 1456–1475.

Oueslati, B., and G. Bellon, 2013: Convective Entrainment and Large-Scale Organization of Tropical Precipitation: Sensitivity of the CNRM-CM5 Hierarchy of Models. *Journal of Climate,* **26**, 2931–2946.

Parsons, D. B., K. Yoneyama, and J.-L. Redelsperger, 2000: The evolution of the tropical western Pacific atmosphere–ocean system following the arrival of a dry intrusion. *Quarterly Journal of the Royal Meteorological Society,* **126**, 517–548.

Peters, O., and J. D. Neelin, 2006: Critical phenomena in atmospheric precipitation. *Nature Phys.,* **2**, 393–396.

Pritchard, M. S., M. W. Moncrieff, and R. C. Somerville, 2011: Orogenic propagating precipitation systems over the United States in a global climate model with embedded explicit convection. *Journal of the Atmospheric Sciences*, **68**, 1821-1840.

Purdom, J. F., 1976: Some uses of high-resolution GOES imagery in the mesoscale forecasting of convection and its behavior. *Monthly Weather Review*, **104**, 1474-1483.

Randall, D. A., Harshvardhan, and D. A. Dazlich, 1991: Diurnal variability of the hydrologic cycle in a general circulation model. *Journal of the Atmospheric Sciences,* **48**, 40–62.

Raymond, D. J. and A. M. Blyth, 1986: A stochastic mixing model for nonprecipitating cumulus clouds. *Journal of the Atmospheric Sciences,* **43**, 2708-2718.

Raymond, D. J. and D. J. Torres, 1998: Fundamental moist modes of the equatorial troposphere. *Journal of the Atmospheric Sciences,* **55**, 1771-1790.

Raymond, D. J., 2000: Thermodynamic control of tropical rainfall. *Quarterly Journal of the Royal Meteorological Society,* **126**, 889–898.

Raymond, D. J. and X. Zeng, 2000: Instability and large-scale circulations in a two-column model of the tropical troposphere. *Quarterly Journal of the Royal Meteorological Society,* **126**, 3117-3135.

Raymond, D. J., S. L. Sessions, A. H. Sobel, and Z. Fuchs, 2009: The Mechanics of Gross Moist Stability. *Journal of Advances in Modeling Earth Systems,* **1**(3).

Raymond, D. J., Z. Fuchs, S. Gjorgjievska, and S. Sessions, 2015: Balanced dynamics and convection in the tropical troposphere. *Journal of Advances in Modeling Earth Systems*, **7**, 1093-1116.

Redelsperger, J. L., D. B. Parsons, and F. Guichard, 2002: Recovery processes and factors limiting cloud-top height following the arrival of a dry intrusion observed during TOGA–COARE. *Journal of the Atmospheric Sciences,* **59**, 2438–2457.

Ridout, J., 2002: Sensitivity of Tropical Pacific Convection to Dry Layers at Mid- to Upper Levels: Simulation and Parameterization Tests. *Journal of the Atmospheric Sciences,* **59**, 3362-3381.

Rio, C., F. Hourdin, J. Y. Grandpeix, and J. P. Lafore, 2009: Shifting the diurnal cycle of parameterized deep convection over land. *Geophysical Research Letters*, **36**.

Romps, D. M., and Z. Kuang, 2010: Do Undiluted Convective Plumes Exist in the Upper Tropical Troposphere? *Journal of the Atmospheric Sciences,* **67**, 468-484.

Romps, D. M., and N. Jeevanjee, 2016: On the sizes and lifetimes of cold pools. *Quarterly Journal of the Royal Meteorological Society*, **142**, 1517-1527.

Rosenfeld, D. and I. M. Lensky, 1998: Satellite-based insights into precipitation formation processes in continental and maritime convective clouds. *Bulletin of the American Meteorological Society*, **80**, 2457-2477.

Rosenfeld, D., U. Lohmann, G. B. Raga, C. D. O'Dowd, M. Kulmala, S. Fuzzi, A. Reissell, and M. Andreae, 2008: Flood or Drought: How Do Aerosols Affect Precipitation? *Science*, **321**, 1309-1313.

Rotunno, R., J. B. Klemp, and M. L. Weisman, 1988: A Theory for Strong, Long-Lived Squall Lines. *Journal of the Atmospheric Sciences,* **45**, 463–485.

Rowe, A. K., and R. A. Houze, Jr., 2015: Cloud organization and growth during the transition from suppressed to active MJO conditions. *Journal of Geophysical Research: Atmospheres.*, **120**, 10324–10350.

Sahany, S. and R. S. Nanjundiah, 2008: Impact of convective downdrafts on model simulations: results from aqua-planet integrations. In *Annales geophysicae: atmospheres, hydrospheres and space sciences* (Vol. 26, No. 7, p. 1877).

Sahany, S., J. D. Neelin, K. Hales, and R. B. Neale, 2012: Temperature-moisture dependence of the deep convective transition as a constraint on entrainment in climate models. *Journal of the Atmospheric Sciences,* **69**, 1340–1358.

Sahany, S., J. D. Neelin, K. Hales and R. B. Neale, 2014: Deep Convective Transition Characteristics in the NCAR CCSM and Changes Under Global Warming. *Journal of Climate*, **27**, 9214-9232.

Sanderson, B. M., R. Knutti, T. Aina, C. Christensen, N. Faull, D. J. Frame, W. J. Ingram, C. Piani, D. A. Stainforth, D. A. Stone, and M. R. Allen, 2008: Constraints on Model Response to Greenhouse Gas Forcing and the Role of Subgrid-Scale Processes. *Journal of the Atmospheric Sciences,* **21**, 2384-2400.

Schiro, K. A., J. D. Neelin, D. K. Adams, and B. R. Lintner, 2016: Deep Convection and Column Water Vapor over Tropical Land versus Tropical Ocean: A Comparison between the

Amazon and the Tropical Western Pacific. *Journal of the Atmospheric Sciences*, **73**, 4043-4063.

Schlemmer, L., and C. Hohenegger, 2014: The Formation of Wider and Deeper Clouds as a Result of Cold-Pool Dynamics. *Journal of the Atmospheric Sciences,* **71**, 2842–2858.

Sherwood, S. C., and R. Wahrlich, 1999: Observed evolution of tropical deep convective events and their environment. *Monthly Weather Review,* **127**, 1777–1795.

Sherwood, S. C., P. Minnis, and M. McGill, 2004: Deep convective cloud-top heights and their thermodynamic control during CRYSTAL–FACE. *Journal of Geophysical Research*, **109**, D20119.

Siebesma, A. P., P. M. M. Soares, and J. Teixeira, 2007: A combined eddy-diffusivity mass-flux approach for the convective boundary layer. *Journal of the Atmospheric Sciences,* **64**, 1230–1248.

Simpson, J., 1971: On cumulus entrainment and one-dimensional models. *Journal of the Atmospheric Sciences,* **28**, 449-455.

Sobel, A. H., S. E. Yuter, C. S. Bretherton, and G. N. Kiladis, 2004: Large-Scale Meteorology and Deep Convection during TRMM KWAJEX. *Monthly Weather Review*, **132**, 422-444.

Srivastava, R. C., 1987: A model of intense downdrafts driven by the melting and evaporation of precipitation. *Journal of the Atmospheric Sciences*, **44**, 1752-1774.

Stechmann, S. N., and J. D. Neelin, 2011: A stochastic model for the transition to strong convection. *Journal of the Atmospheric Sciences*, **68**, 2955–2970.

Stechmann, S. N., and J. D. Neelin, 2014: First-Passage-Time prototypes for precipitation statistics. *Journal of the Atmospheric Sciences,* **71**, 3269-3291.

Stirling, A. J., and R. A. Stratton, 2012: Entrainment processes in the diurnal cycle of deep convection over land. *Quarterly Journal of the Royal Meteorological Society,* **138**, 1135 – 1149.

Suhas, E., and G. J. Zhang, 2014: Evaluation of trigger functions for convective parameterization schemes using observations. *Journal of Climate*, **27**, 7647-7666.

Sun, J., S. Braun, M. I. Biggerstaff, R. G. Fovell, and R. A. Houze Jr, 1993: Warm upper-level downdrafts associated with a squall line. *Monthly Weather Review*, **121**(10), 2919-2927.

Terai, C. R. and R. Wood, 2013: Aircraft observations of cold pools under marine stratocumulus. *Atmospheric Chemistry and Physics*, **13**(19), 9899-9914.

Tian, B., D. Waliser, E. J. Fetzer, B. H. Lambrigtsen, Y. L. Yung, and B. Wang, 2006: Vertical most thermodynamic structure and spatial-temporal evolution of the MJO in AIRS observations. *Journal of the Atmospheric Sciences,* **63**, 2462-2485.

Tiedtke, M., 1989: A comprehensive mass flux scheme for cumulus parameterization in large-scale models. *Monthly Weather Review*, **117**(8), 1779-1800.

Tompkins, A. M., 2001a: Organization of tropical convection in low vertical wind shears: The role of water vapor. *Journal of the Atmospheric Sciences,* **58**, 529–545.

Tompkins, A. M., 2001b: Organization of tropical convection in low vertical wind shears: The role of cold pools. *Journal of the Atmospheric Sciences,* **58**, 1650–1672

Torri, G. and Z. Kuang, 2016: A Lagrangian study of precipitation-driven downdrafts. *Journal of the Atmospheric Sciences*, **73**(2), 839-854.

Turner, D. D., S. A. Clough, J. C. Liljegren, E. E. Clothiaux, K. E. Cady-Pereira, and K. L. Gaustad, 2007: Retrieving Liquid Water Path and Precipitable Water Vapor From the

Atmospheric Radiation Measurement (ARM) Microwave Radiometers. *IEEE Transactions on Geoscience and Remote Sensing*, **45**(11), 3680-3690.

Waite, M. L., and B. Khouider, 2010: The deepening of tropical convection by congestus preconditioning. *Journal of the Atmospheric Sciences,* **67**, 2601–2615.

Wakimoto, R. M., 1982: The life cycle of thunderstorm gust fronts as viewed with Doppler radar and rawinsonde data. *Monthly Weather Review*, **110**(8), 1060-1082.

Wang, W. and M. E. Schlesinger, 1999: The dependence on convection parameterization of the tropical intraseasonal oscillation simulated by the UIUC 11-layer atmospheric GCM. *Journal of Climate*, **12**, 1423-1457.

Wang, H. and G. Feingold, 2009: Modeling mesoscale cellular structures and drizzle in marine stratocumulus. Part I: Impact of drizzle on the formation and evolution of open cells. *Journal of the Atmospheric Sciences*, **66**, 3237-3256.

Wang, J., R. Krejci, S. Giangrande, C. Kuang, H.M. Barbosa, J. Brito, S. Carbone, X. Chi, J. Comstock, F. Ditas, and J. Lavric, 2016: Amazon boundary layer aerosol concentration sustained by vertical transport during rainfall. *Nature,* **539**, 416-419.

Wei, D., A. M. Blyth, and D. J. Raymond, 1998: Buoyancy of convective clouds in TOGA COARE. *Journal of the Atmospheric Sciences,* **55**, 3381–3391.

Weisman, M. L., and J. B. Klemp, 1986: Characteristics of isolated convective storms. In *Mesoscale Meteorology and Forecasting* (pp. 331-358). American Meteorological Society.

Wilson, J. W., and W. E. Schreiber, 1986: Initiation of convective storms at radar-observed boundary-layer convergence lines. *Monthly Weather Review*, **114**(12), 2516-2536.

Wu, C.-M., B. Stevens, and A. Arakawa, 2009: What controls the transition from shallow to deep convection? *Journal of the Atmospheric Sciences*, **66**, 1793-1806.

Xie, S., M. Zhang, J. S. Boyle, R. T Cederwall, G. L. Potter, and W. Lin, 2004: Impact of a revised convective triggering mechanism on Community Atmosphere Model, version 2, simulations: Results from short-range weather forecasts. *Journal of Geophysical Research: Atmospheres*, **109**.

Xu, W. and E. J. Zipser, 2012: Properties of deep convection in tropical continental, monsoon, and oceanic rainfall regimes. *Geophysical Research Letters*, **39**, L07802.

Yang, G. Y., and J. M. Slingo, 2001: The diurnal cycle in the tropics, *Monthly Weather Review,* **129**, 784 – 801.

Yoneyama, K. and T. Fujitani, 1995: The behavior of dry westerly air associated with convection observed during the TOGA-COARE R/V Natsushima cruise. *Journal-Meteorological Society of Japan*, **73**, 291-304.

Zhang, G. J., and M. Mu, 2005: Simulation of the Madden–Julian oscillation in the NCAR CCM3 using a revised Zhang–McFarlane convection parameterization scheme. *Journal of Climate*, **18**, 4046-4064.

Zhang Y., and Klein S. A., 2010: Mechanisms affecting the transition from shallow to deep convection over land: Inferences from observations of the diurnal cycle collected at the ARM Southern Great Plains Site. *Journal of the Atmospheric Sciences,* **67**, 2943–2959.

Zhang, G. J., and X. Song, 2016: Parameterization of Microphysical Processes in Convective Clouds in Global Climate Models. *Meteorological Monographs*, **56**, Ch. 12.

Zhao, M., I. M. Held, S.-J. Lin, And G. A. Vecchi, 2009: Simulations of Global Hurricane Climatology, Interannual Variability, and Response to Global Warming Using a 50-km Resolution GCM. *Journal of Climate*, **22**, 6653-6678.

Zipser, E. J., 1969: The role of organized unsaturated convective downdrafts in the structure and rapid decay of an equatorial disturbance. *Journal of Applied Meteorology*, **8**, 799-814.

Zipser, E. J., 1977: Mesoscale and convective–scale downdrafts as distinct components of squall-line structure. *Monthly Weather Review*, **105**, 1568-1589.

Zipser, E. J., and M. A. LeMone (1980), Cumulonimbus vertical velocity events in GATE. Part II: Synthesis and model core structure. *Journal of the Atmospheric Sciences,* **37**, 2458–2469.

Zhang, G. J. and N. A. McFarlane, 1995: Sensitivity of climate simulations to the parameterization of cumulus convection in the Canadian climate centre general circulation model. *Atmosphere-Ocean*, **33**, 407-446.

Zuidema, P., Z. Li, R. J. Hill, L. Bariteau, B. Rilling, C. Fairall, W. A. Brewer, B. Albrecht, and J. Hare, 2012: On trade wind cumulus cold pools. *Journal of the Atmospheric Sciences*, **69**, 258-280.